The Atlantic Multidecadal Oscillation in models and observations

Leela Frankcombe

ISBN 978-90-393-5365-3

COVER: An artist's impression of figure 6.7(b), by Phillip Frankcombe. Oil and acrylic on canvas board, 2010.

The Atlantic Multidecadal Oscillation in models and observations

De Atlantische Multidecadale Oscillatie in modellen en observaties

(met een samenvatting in het Nederlands)

PROEFSCHRIFT

ter verkrijging van de graad van doctor aan de Universiteit Utrecht
op gezag van de rector magnificus, prof. dr. J. C. Stoof,
ingevolge het besluit van het college voor promoties
in het openbaar te verdedigen op

maandag 5 juli 2010 des middags te 4:15 uur

door

Leela Mary Frankcombe

geboren op 13 januari 1984 te Melbourne, Australië

PROMOTOR: **Prof. dr. ir. H. A. Dijkstra**
CO-PROMOTOR: **Dr. A. S. von der Heydt**
Institute for Marine and Atmospheric research Utrecht (IMAU),
Faculty of Physics and Astronomy, University of Utrecht

Dit proefschrift werd mogelijk gemaakt door financiële steun van de Nederlandse organisatie voor Wetenschappelijk Onderzoek (NWO), sectie Aard- en Levenswetenschappen (ALW) onder contract nr. 854.00.037.

‘The universe is full of magical things,
patiently waiting for our wits to grow sharper.’

Eden Phillpotts
(1862 - 1960)

CONTENTS

SUMMARY

Climate variability is a phenomenon of which we are all aware. Variability on the time scale of days or months, what we call 'weather', may be the most immediate example of climate variability but it is only a small part of the spectrum. The climate also varies on longer time scales and it is this low frequency variability which is the subject of this thesis. In particular we focus on inter- to multidecadal variability of the climate of the North Atlantic.

Low frequency variability has been observed in sea surface temperatures in the North Atlantic. This variability has a time scale in the range of 30 – 70 years and a particular spatial pattern and has been named the 'Atlantic Multidecadal Oscillation' or AMO. Due to this variability the North Atlantic was unusually warm in the 1940s and 50s as well as after the mid 1990s, and anomalously cool around 1920 and during the 1970s. The influence of the AMO extends beyond the ocean alone, affecting the climate of the surrounding land. The positive phase of the AMO (warmer than normal temperatures in the North Atlantic) has been linked to warmer temperatures in Europe, less rainfall over the central United States, more rainfall in Florida and the Sahel, a stronger Indian monsoon as well as stronger and more frequent hurricanes in the North Atlantic. Greater understanding of the AMO would thus be very useful for weather and climate prediction. The AMO also plays a role in the variability of the global mean temperature. Apart from the increase associated with anthropogenic forcings, the global mean temperature shows variability on multidecadal time scales which may be at least partially explained by the AMO.

There are two different approaches to modelling and understanding the physics of the AMO. In one method we can use Coupled General Circulation Models (CGCMs) to simulate the entire climate and then try to understand the processes which cause variability. This method has lead to the idea that the AMO is linked to variations in the strength of the overturning circulation of the ocean, although the time scale seems to be dependent on the model used. The drawback of this approach is that in these complex models there are always many different fields varying at the same time which makes it difficult to separate cause from effect. This has lead to numerous different descriptions of the physics of the AMO.

The other approach to studying the AMO uses a so-called 'minimal model', the simplest possible model which can still simulate the fundamental physics of the system.

Additional processes may later be included in the model to make it more realistic and to allow comparisons with more complex models as well as with observations, but these additions do not change the underlying physical processes. We know, from studies using such a minimal model, that an AMO-like oscillation appears in simple ocean models as a so-called Hopf bifurcation, where the stable equilibrium state changes from steady flow to a periodic oscillation. The precise physical mechanisms of the variability have also been described using the minimal model - the oscillation is caused by an out of phase response of zonal and meridional overturning anomalies which results in westward propagating temperature anomalies. The time scale of the variability is then due to the time it takes for the anomalies to travel across the ocean basin. The mechanism of the AMO from the minimal model is described in chapter 2, where it is also shown that the pattern of temperature anomalies from the minimal model resembles those from observations.

An element that has been missing from the minimal model theory, as developed so far, is the effect of the atmosphere. Some GCM studies have shown that if high frequency variability in the atmosphere is removed then the low frequency variability from the ocean also disappears, which indicates that the oceanic variability is being excited by the atmospheric noise. This idea is explored in chapter 3. Since the minimal model is an ocean-only model, the effect of the atmosphere is modelled through a boundary condition at the surface of the ocean. Atmospheric variability is mimicked by adding noise to this boundary condition and we find that the AMO-like oscillation is indeed excited by this noise. While purely white noise does excite the variability, higher amplitude oscillations appear when the atmospheric noise has a coherent spatial and temporal pattern. From this we conclude that atmospheric variability such as the North Atlantic Oscillation (NAO; a pattern of atmospheric variability in the atmosphere over the North Atlantic) could excite the AMO.

With the inclusion of the effect of the atmosphere in the minimal model the most relevant additions to the minimal model have been made. To validate the model we need to compare its results to observations, which is done in chapter 4. One of the most distinctive features of the minimal model mechanism is the westward propagation of temperature anomalies at the surface of the ocean. In observations of sea surface temperature this is difficult to see, both because of the disrupting effect of atmospheric noise, as well as because of the strong eastwards propagating signal of the Gulf Stream. Observations of temperature in the few hundred metres below the surface of the ocean do, however, show evidence of westward propagation in agreement with the minimal model mechanism. Since the time series of observed sub-surface temperatures is too short to be convincing evidence, chapter 5 continues the comparison with observations from tide gauges which measure sea level around the North Atlantic, and for which longer time series are available. The link between sea level and the AMO comes about because temperature anomalies are associated with sea surface height anomalies, so the propagation of temperature anomalies across the North Atlantic is visible in the phase difference between sea level anomalies measured at the coast along each side of the ocean basin. The variability in sea level is found in a GCM (the GFDL CM2.1 model) as well as in observations and both agree with the idea of westward propagating anomalies from the minimal model.

The next question, discussed in chapter 6, is one of time scale. Early observations of

the AMO put its period at 50-70 years while the subsurface temperature record discussed in chapter 4 and the tide gauge measurements of chapter 5 indicate a period closer to 20-30 years. Many GCMs show variability in the North Atlantic on both these time scales. In addition, low frequency variability in the Arctic is also found in both observations and GCMs. Variability originating in the North Atlantic may propagate into the Arctic and vice versa. It is difficult to tell, from the limited observations that are available, which basin the variability on different time scales comes from. In 6 we show that in the GFDL CM2.1 GCM there is variability on long time scales in salinity in the Arctic ocean. The hypothesis is that the 20-30 year variability is due to the AMO mechanism from the minimal model while the 50-70 year variability may originate in the Arctic.

This Arctic salinity variability is further investigated in chapter 7. An idealised model is used to study the different kinds of variability that are present in the Arctic basin and we find that a multidecadal oscillation in salinity does indeed appear in the model. There are promising signs that, once the oscillation has been deformed by the intricate topography of the Arctic basin, its spatial pattern will resemble the variability found in the Arctic in the GFDL CM2.1 GCM, supporting the hypothesis that some of the low-frequency variability observed in the North Atlantic may be due to internal variability in the Arctic. Further research on this Arctic variability is needed.

SAMENVATTING

Variabiliteit in het klimaat is een verschijnsel waarvan iedereen zich bewust is. De variaties op tijdschalen van dagen of maanden, oftwel het 'weer', zijn wellicht het meest in het oog springende voorbeeld van deze variabiliteit, maar beslaan slechts een klein deel van het spectrum. Het klimaat varieert ook op langere tijdschalen en deze laagfrequente variabiliteit is het onderwerp van dit proefschrift. In het bijzonder richten we ons op inter- en multidecadale variabiliteit van het klimaat van de Noord-Atlantische Oceaan.

De oppervlaktetemperatuur van de Noord-Atlantische Oceaan vertoont laagfrequente variabiliteit. Deze variabiliteit heeft een tijdschaal van tussen de 30 en 70 jaar en een specifiek ruimtelijk patroon en wordt de 'Atlantische Multidecadale Oscillatie' of AMO genoemd. Door deze variabiliteit was de Noord-Atlantische Oceaan relatief warm in de jaren '40 en '50, en ook na de midden jaren '90, en relatief koel rond 1920 en in de jaren '70. De reikwijdte van de AMO is groter dan alleen de oceaan; ook het omringende land wordt beïnvloed. De positieve fase van de AMO (hogere temperaturen dan normaal in de Noord-Atlantische Oceaan) is in verband te brengen met hogere temperaturen in Europa, minder regen in de Centraal-Verenigde Staten, meer regen in Florida en de Sahel, een krachtigere moesson in India en zowel meer als sterkere orkanen boven de Noord-Atlantische Oceaan. Een beter begrip van de AMO is dus heel bruikbaar voor weers- en klimaatvoorspellingen. De AMO speelt ook een rol in de variabiliteit van de wereldgemiddelde temperatuur. Naast de opwarming die geassocieerd wordt met menselijke invloeden, vertoont deze temperatuur ook variabiliteit op multidecadale tijdschalen die tenminste voor een deel door de AMO verklaard kan worden.

Er zijn twee verschillende manieren om het modelleren en begrijpen van de fysica achter de AMO te benaderen. De ene methode maakt gebruik van gekoppelde algemene circulatiemodellen ('Coupled General Circulation Models', CGCMs) om het gehele klimaat te simuleren en dan de processen die de variabiliteit veroorzaken te begrijpen. Deze methode heeft ertoe geleid dat de AMO wordt gerelateerd aan variaties in de sterkte van de meridionale omwentelingscirculatie (of de 'lopende band' circulatie) in de oceaan, al is de tijdschaal erg afhankelijk van welk model er wordt gebruikt. Het nadeel van deze methode is dat het moeilijk is om oorzaak en gevolg te scheiden. Hierdoor is er een aantal verschillende beschrijvingen van de fysica achter de AMO.

De andere benadering om de AMO te bestuderen maakt gebruik van een zogenoemd 'minimaal model': het simpelst mogelijke model dat nog steeds de fundamentele fysica

van het systeem kan simuleren. Aanvullende processen kunnen later nog aan het model worden toegevoegd om het realistischer te maken en om vergelijking met complexere modellen en waarnemingen mogelijk te maken, maar deze aanvullingen veranderen de onderliggende fysica niet. Uit eerdere studies met zo'n minimaal model weten we dat een AMO-achtige oscillatie zich in simpele oceaanmodellen openbaart als een zogenaamde Hopf bifurcatie, waar de stabiele evenwichtscirculatie van een stationaire stroming in een periodieke oscillatie overgaat. Het precieze mechanisme van de variabiliteit is ook beschreven met behulp van het minimale model - de oscillatie wordt veroorzaakt door een reactie in de zonale en meridionale stromingen van de omwentelingscirculatie die uit fase is, wat resulteert in westwaarts bewegende temperatuuranomalieën. De tijdschaal wordt dan bepaald door de tijd die de anomalie nodig heeft om het bekken over te steken. Het mechanisme van de AMO uit het minimale model is beschreven in hoofdstuk 2, waar ook is aangetoond dat het patroon van de temperatuuranomalieën uit het minimale model lijkt op het patroon uit observaties.

Een element dat nog miste in de minimale modeltheorie is het effect van de atmosfeer. Verschillende CGCM studies laten zien dat met het wegnemen van de hoogfrequente variabiliteit in de atmosfeer ook de laagfrequente variabiliteit uit de oceanen verdwijnt, wat een indicatie is voor het idee dat de oceaanvariabiliteit wordt opgewekt door ruis in de atmosfeer. Dit concept wordt verkend in hoofdstuk 3. Omdat het minimale model alleen de oceaan beslaat, wordt het effect van de atmosfeer gemodelleerd door een randvoorwaarde op het oceaanoppervlak. Atmosferische variabiliteit wordt nagebootst door ruis op te tellen bij deze randvoorwaarde en dan vinden we een AMO-achtige oscillatie die inderdaad wordt aangewakkerd door deze ruis. Pure witte ruis slaat de oscillatie al aan, maar we krijgen een grotere uitwijking in de oscillatie als de atmosfeerruis een coherent ruimtelijk en tijdspatroon heeft. Hieruit concluderen we dat de amosfeervariabiliteit zoals de Noord-Atlantische Oscillatie (NAO; een specifiek patroon van variabiliteit in de atmosfeer boven de Noord-Atlantische Oceaan) de AMO kan activeren.

Met de uitbreiding van het minimale model met het effect van de atmosfeer zijn de meest relevante aanvullingen gemaakt. Om het model te valideren moeten we de resultaten met observaties vergelijken, wat is gedaan in hoofdstuk 4. Een van de opvallendste eigenschappen van het mechanisme uit het minimale model is de westwaartse voortplanting van de temperatuuranomalieën op het oceaanoppervlak. Dit is moeilijk te zien in waarnemingen van de oppervlaktetemperatuur, enerzijds door het verstorende effect van de atmosferische ruis, anderzijds door een sterk, zich oostwaarts voortplantend signaal van de Warme Golfstroom. Temperatuurobservaties in de paar honderd meter onder het oppervlak getuigen wel van westwaartse voortplanting, overeenkomend met het mechanisme uit het minimale model. Maar omdat de tijdreeks van onderzeese temperaturen te kort is om overtuigend bewijs te leveren, gaat hoofdstuk 5 door met het vergelijken van data uit peilschalen (getijdemeters) die het zeeniveau rond de Noord-Atlantische Oceaan meten en waarvoor veel langere tijdreeksen beschikbaar zijn. De koppeling tussen de AMO en de waterstand komt uit het feit dat de temperatuuranomalieën gerelateerd zijn met zeeniveau-anomalieën. Hierdoor zien we de voortplanting van de temperatuuranomalie over de Noord-Atlantische Oceaan in het faseverschil tussen zeeniveau-anomalieën die gemeten worden langs beide kusten van het oceaanbekken. Behalve in de waarnemingen is de variabiliteit in zeeniveau ook gevonden in een GCM

(het GFDL CM2.1 model), en beide bevestigen het idee van de westwaartse voortplanting van de temperatuuranomalieën uit het minimale model.

De volgende vraag, die wordt behandeld in hoofdstuk 6, gaat over de tijdschaal. De eerste waarnemingen van de AMO laten een periode zien van 50 tot 70 jaar, terwijl de onderzeese temperatuurmetingen die besproken worden in hoofdstuk 4 en de observaties uit de peilschalen in hoofdstuk 5 meer op een periode van 20 tot 30 jaar wijzen. Veel GCM's laten variabiliteit zien op beide tijdschalen in de Noord-Atlantische Oceaan. Daarbij is er ook laagfrequente variabiliteit in de Noordelijke IJszee zichtbaar in zowel de observaties als in GCM's. Variabiliteit die ontstaat in de Noord-Atlantische Oceaan kan propageren naar de Noordelijke IJszee en andersom. Het is moeilijk te onderscheiden, door het beperkte aantal beschikbare waarnemingen, uit welk bekken de variabiliteit komt. In hoofdstuk 6 laten we zien dat het zoutgehalte in de Noordelijke IJszee in het GFDL CM2.1 model variabiliteit met een lange tijdschaal vertoont. De hypothese is dat de 20-30 jarige variabiliteit door het minimale modelmechanisme komt, terwijl de 50-70 jarige variabiliteit in de Noordelijke IJszee ontstaat.

Deze Arctische zoutvariabiliteit wordt verder onderzocht in hoofdstuk 7. Een geïdialiseerd model wordt gebruikt om de verschillende soorten variabiliteit in de Noordelijke IJszee te bestuderen en we vinden inderdaad een multidecadale oscillatie in zoutgehalte. Er zijn veelbelovende aanwijzingen dat als deze oscillatie vervormd wordt door de complexe topografie van het Arctisch Bekken, dat dan het ruimtelijke patroon overeen komt met de Arctische variabiliteit in het GFDL CM2.1 model. Dit onderschrijft de hypothese dat een deel van de Noord Atlantische variabiliteit voortkomt uit interne variabiliteit in de Noordelijke IJszee. Er is vervolgonderzoek nodig over deze Arctische variabiliteit.

(Vertaald door Selma Huisman)

1 INTRODUCTION

The temperature of the Earth is maintained by the balance between incoming and outgoing solar radiation. Short wave radiation from the sun warms the Earth, long wave radiation from the Earth returns to space. The amount of incoming solar radiation depends strongly on latitude, low latitudes receive much more incoming radiation than high latitudes. This is reflected in the higher temperatures near the equator compared to the poles. However, if temperature at the Earth's surface depended solely on the amount of incoming radiation then the temperature differential would be much larger. The balance is maintained by the transport of large amounts of heat from the equator towards the poles. This heat transport is carried out by both the atmosphere and the ocean.

1.1 THE CIRCULATION OF THE OCEAN

Water at the surface of the ocean at low latitudes absorbs heat. This heat is then transported with the water due to the circulation of the ocean. Heat can only be exchanged between the atmosphere and the ocean at the ocean's surface and, since water has a large heat capacity, the deep ocean acts as an enormous reservoir for heat storage. In fact, the upper 2.5m of the ocean can store as much heat as the entire atmosphere.

The circulation of the ocean can be broadly divided into two parts: the wind-driven circulation and the density-driven circulation. The wind-driven part of the circulation is caused by the flux of momentum from the wind to the surface of the ocean and is largely responsible for the pattern of currents at the surface of the ocean (Peizoto and Oort, 1984). The density-driven part of the circulation is due to the fluxes of heat and freshwater between the ocean and the atmosphere and is thus called the thermohaline circulation (THC; Broecker, 1991). These fluxes change the density of the surface waters, which impacts the stability of the water column. These changes are propagated both along the surface and to the deeper ocean by advection and mixing. While the wind-driven part of the circulation is restricted to the upper part of the ocean, the thermohaline circulation involves the whole depth.

It is the thermohaline circulation which is responsible for many of the features of our current climate. Figure 1.1 shows a broad outline of the present THC. This is not an exact picture, rather it is an impression of the circulation that is found when averaged

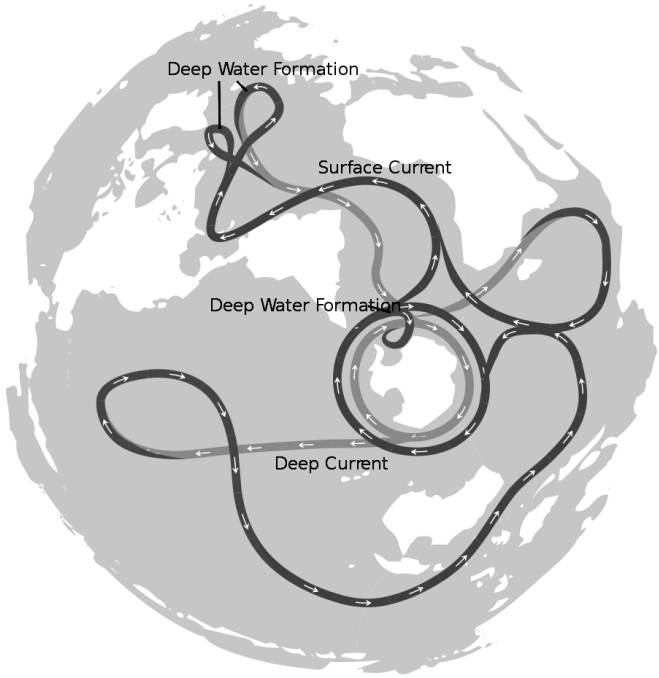

FIGURE 1.1: *Conceptual view of the thermohaline circulation. Surface waters are shown in darker shades, deep waters are lighter. Original version by Alexandre Van de Sande, from Wikimedia Commons under a Creative Commons Attribution-Share Alike license.*

over the entire ocean for a long period of time. Surface waters flow northwards in the Atlantic, carrying with them vast amounts of heat which is then released to the atmosphere in the northern North Atlantic (Ganachaud and Wunsch, 2000). This is the reason for the mild climate of Europe in comparison to other land areas at the same latitudes. The surface waters, now cooler and denser, sink and return southwards at depth. Water masses between all the oceans are transported in the Southern Ocean, in the eastward flowing Antarctic Circumpolar Current (ACC). This spreads the deep water from the North Atlantic to the Indian and Pacific oceans, where it gradually returns to the surface. The loop is completed by the return of surface waters from the Pacific and Indian oceans to the Atlantic. This occurs along the ACC from the Pacific directly into the southern Atlantic through Drake Passage and also, to a lesser extent, through the Indonesian throughflow and around the southern tip of Africa as part of the Agulhas current.

While, when averaging over large areas and long periods of time, we may consider the ocean circulation as a smooth, unbroken loop, in reality it is made up of various currents, each of which varies in time. This variability can cause large variations in the way heat is transported, thus affecting the climate.

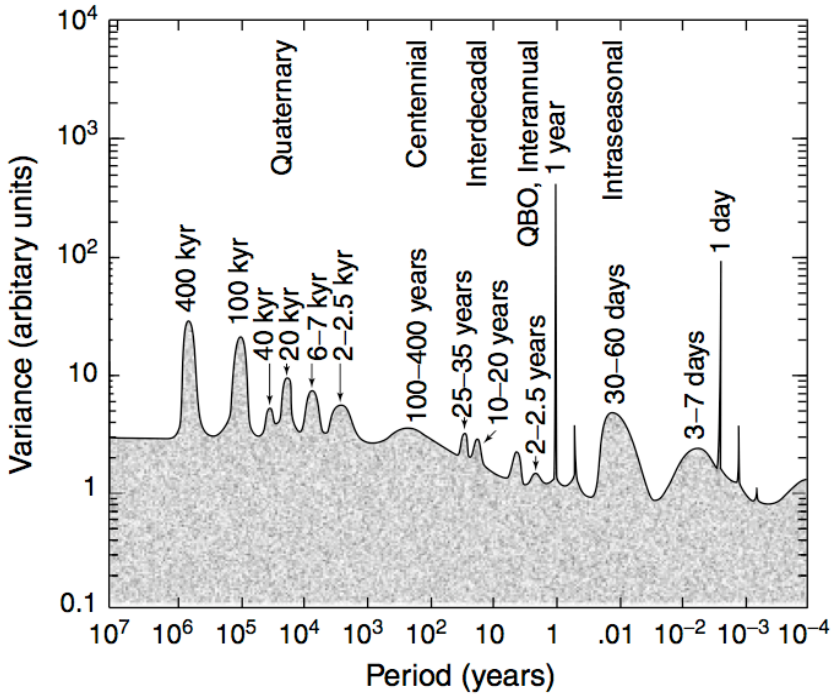

FIGURE 1.2: *Composite spectrum of climate variability over the last* 10^7 *years. Taken from Ghil (2002).*

1.2 VARIABILITY OF THE CLIMATE

We are all familiar with climate variability. One day is warmer or cooler than another, one month rainier or drier. We have all experienced particularly warm summers and wet autumns; but variability on the time scale of days or months, what we think of as 'weather', is only a small part of the spectrum. The climate also varies on much longer time scales. Figure 1.2 shows an artist's impression of the variability over the last 10 million years (Ghil, 2002).

The spectrum may be divided into three parts: sharp peaks (at one day and one year, for example) corresponding to periodically forced variations, broader peaks due to internal modes of variability in the climate system, and the continuous background portion of the spectrum which arises from stochastically forced variations.

Starting from the high frequency (short period) end of the spectrum, the first large peak is at a period of one day. This is, of course, the diurnal cycle, the cycle of day and night caused by the rotation of the Earth on its axis. The second, much broader peak, has a period of three to seven days, and is associated with the mid-latitude weather systems which we are all familiar with from weather maps. These are formed due to the baroclinic instability of the large scale atmospheric flow. Intraseasonal variability, on time scales of 30-60 days, is due to low frequency atmospheric variability such as the Madden-Julian oscillation in the tropics and the zonal/blocked flow in mid-latitudes.

The second sharp peak has a period of one year and represents the seasonal cycle, caused by the revolution of the Earth around the sun and the tilt of the Earth's axis.

We then come to variability on time scales longer than one year. The quasi-biennial oscillation (QBO) is an oscillation of the zonal wind in the tropical stratosphere that has a period of 2-2.5 years. The next peak, with a period of 3-7 years, belongs to the El Niño-Southern Oscillation (ENSO), a mode of coupled ocean-atmosphere variability in the tropical Pacific and probably the most well known form of long time scale internal climate variability.

Continuing to the longest time scales depicted in this spectrum, we reach variability beyond the scope of the instrumental record. These oscillations are known through the study of paleo records such as ice cores. At 2-2.5 thousand years is a peak representing Dansgaard-Oescheger cycles. These rapid events occurred during the last glacial period and are thought to be related to fluctuations in the strength of the overturning circulation, which causes variations in the amount of heat transported into the Northern Hemisphere. Heinrich events, with a period of 6-7 thousand years, also occurred during the last ice age and are associated with the release of large amounts of ice from the northern ice sheets. The peaks at 20, 40, 100 and 400 thousand years are due to orbital variations such as precession (the change in the orientation of the Earth's axis relative to the sun), obliquity (the angle between the Earth's axis and the ecliptic) and eccentricity (the shape of the Earth's orbit).

The spectrum in figure 1.2 also shows peaks at inter- to multidecadal time scales, in particular there are peaks at 10-20 and 25-35 years. These peaks are attributed to the Atlantic Multidecadal Oscillation (AMO) and Pacific Decadal Oscillation (PDO) in the ocean and the North Atlantic Oscillation (NAO) and Arctic Oscillation (AO) in the atmosphere. These time scales are problematic to research since they require longer records with high temporal and spatial resolution, falling between the instrumental record, which has the resolution but not the record length, and proxy records which have the length but not the resolution.

Forecasting the climate on multidecadal time scales also falls between the two different approaches to climate prediction (Cane, 2010). On short time scales, climate prediction relies on accurate knowledge of the current state of the climate system. The state of the atmosphere is particularly important, since it is atmospheric variability which dominates on the time scales of weather prediction. Errors in the initial condition supplied to forecast models grow as the forecast time gets longer, after a certain point the predictions are no longer valid. This is something we are all aware of, perhaps without even noticing - we may trust the weather forecast for tomorrow but put little faith in predictions for the week after next. On long time scales, climate prediction requires knowledge of how the external forcings on the climate system will change, such as solar forcing strength, greenhouse gas concentrations, volcanic activity, etc. In order to separate forced climate changes from natural variability, results from ensembles of climate models are averaged to remove the effect of the initial conditions. Long term climate prediction can thus tell us the general trend that the climate may follow for the next centuries, the validity of the predictions depends on the accuracy of the forecasting of the external forcing parameters. Medium term climate forecasting requires that we take into account initial conditions as well as changing external forcings. In particular, an accurate knowledge of the current state of the ocean becomes vital, since on decadal to

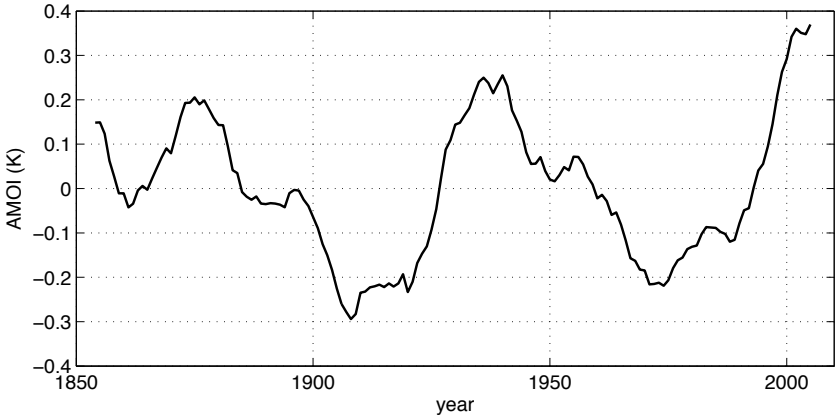

FIGURE 1.3: *AMO index: the ten-year running mean of detrended Atlantic SSTA north of the equator (using data from the HadSST2 dataset).*

multidecadal time scales the natural variability of the climate system is driven largely by the ocean.

The extent to which climate is predictable on the medium to long term can be investigated using climate models. An ensemble is initiated with each member having slightly different initial conditions and the time after which the ensemble members diverge gives an estimate of the predictability of various aspects of the system (see, for example Pohlmann et al., 2004; Keenlyside et al., 2008). Predictability is found to be greatest in the North Atlantic region and it is thought that the increased skill of the predictions may be due to low frequency natural variability in this region. It is this oceanic variability which is the subject of this thesis.

1.3 THE ATLANTIC MULTIDECADAL OSCILLATION

Low frequency variability in sea surface temperatures in the North Atlantic has been found in proxy data stretching back at least 300 years (Delworth and Mann, 2000) and within this data it has a statistically significant peak above a red-noise background. The variability was named the Atlantic Multidecadal Oscillation (AMO) by Kerr (2000). The AMO seems to have a definite time scale range (30 – 70 years) and a particular spatial pattern. An AMO index, defined by Enfield et al. (2001) as the ten-year running mean of detrended Atlantic SST anomalies north of the equator, is plotted in figure 1.3. Warm periods were in the 1940s and from 1995 up to the present, whereas during the 1970s the North Atlantic was relatively cold. A first impression of the pattern was obtained from an analysis of SSTs in the North Atlantic over the last 150 years (Kushnir, 1994). Figure 1.4 shows the difference in SST between the relatively warm years (1950 to 1964) and the relatively cool years (1970 to 1984). There is a negative SST anomaly near the coast of Newfoundland and a positive SST anomaly over the rest of the North Atlantic basin.

A persistent, large scale temperature anomaly over an ocean basin the size of the North Atlantic represents a significant amount of heat. It comes as no surprise, therefore,

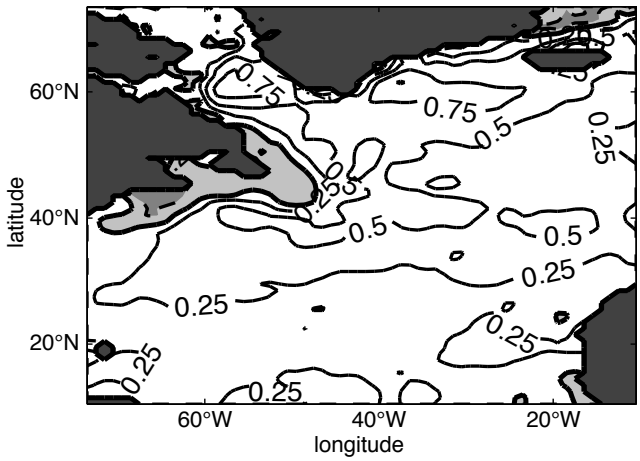

FIGURE 1.4: *AMO pattern: Differences in observed SST between the periods 1950-1964 (warm period) and 1970-1984 (cold period). Units are in °C, negative values are shaded.*

that the AMO has an effect on the climate of the surrounding land masses. Sutton and Hodson (2005) found that sea level pressure, precipitation and temperature over Europe and North America, particularly in summer, are partially driven by the AMO. Figure 1.5 shows the correlation between the AMO index and surface temperatures over the entire globe.

In particular, the AMO has been linked to rainfall and thence to river flows in the US (Enfield et al., 2001). There is a negative correlation between the AMO index and rainfall over the Mississippi basin in the US and a positive correlation between the AMO index and rainfall in Florida. This means that there is on average less rain over Mississippi catchment area and more rain over Florida when the AMO index is high, and more rain over the Mississippi basin and less rain over Florida when the AMO index is low. Figure 1.6 shows the AMO index as well as rainfall in Florida and inflow to Lake Okeechobee, the headwaters of the Everglades. Positive correlations have also been found between the AMO index and rainfall in the Sahel and between the AMO index and the strength of the Indian summer monsoon (Zhang and Delworth, 2006; Knight et al., 2006; Feng and Hu, 2008). Ability to predict the AMO is thus useful for water management and drought prediction.

The strength and frequency of hurricanes has also been positively correlated to the AMO. This is not only due to the temperature of the sea surface but also to changes in vertical shear in the troposphere in the main hurricane development region (Goldenberg et al., 2001; Knight et al., 2006).

Greater understanding of the AMO would thus be very useful for both weather and climate prediction. One further point is the role of the AMO in the variability of the global mean temperature. Apart from the increase associated with anthropogenic forcings, the global mean temperature also shows variability on a range of time scales, including the multidecadal time scale. Zhang et al. (2007) suggest that the AMO can explain at least a portion of the multidecadal variability in global mean temperatures.

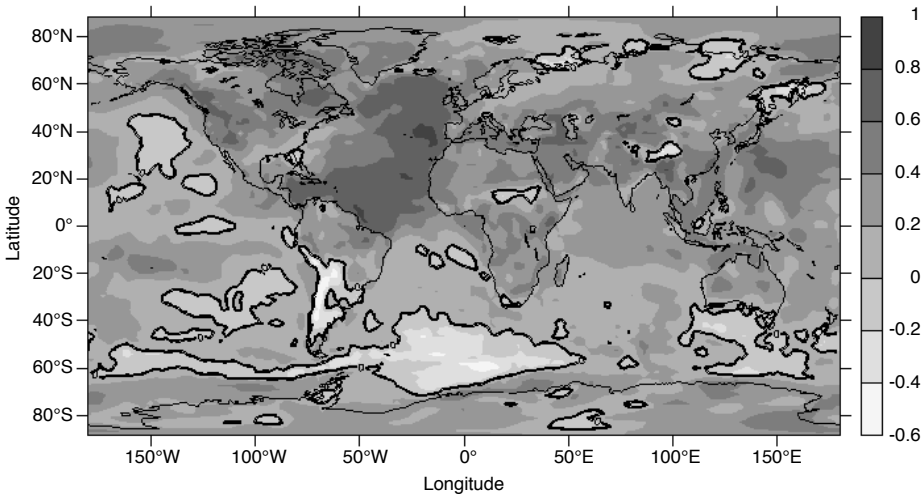

FIGURE 1.5: *Correlation between the AMO index and surface temperature from the NCEP/NCAR reanalysis. The zero contour is bold. Image from NOAA/ESRL Physical Sciences Division, Boulder Colorado (http://www.esrl.noaa.gov/psd/).*

1.4 THIS THESIS

In modelling and understanding the physics of the AMO there appear to be two different, and so far quite disjointed, approaches. In the top down approach, Coupled General Circulation Models (CGCMs) are used to simulate the variability and then deduce the processes from (a mainly statistical) analysis of the different fields. Using the relatively coarse resolution GFDL R15 model, Delworth et al. (1993) were able to simulate the pattern and time scale of the variability. Using regression analysis on the different fields they concluded that the AMO is associated with variations in the Atlantic Meridional Overturning Circulation (AMOC). After a careful sensitivity analysis with the GFDL R15 model, Delworth and Greatbatch (2000) proposed that multidecadal variability is due to an internal ocean mode which is forced by low-frequency variability of the atmosphere. Numerous more recent analyses have come up with similar conclusions, although time scales in models can differ substantially and statistical relations between different fields have lead to different descriptions of the physics of the variability (Eden and Jung, 2001; Cheng et al., 2004; Dong and Sutton, 2005; Jungclaus et al., 2005; Zhu and Jungclaus, 2008). The problem with this type of analysis is that statistically many fields are varying in concert but the chain of processes causing the multidecadal behavior, in particular the pattern and time scale of the variability, can be difficult to extract.

The other approach to studying the AMO is from the bottom up and recognises that there must be a so called ‘minimal model’ which captures the heart of the physics of the AMO. In this context the term ‘minimal model’ refers to the simplest possible model in which AMO-like variability can be simulated. Additional physics included in models extending such a minimal model then only quantitatively affects patterns and time scale, without changing the underlying mechanism of variability. Such a minimal model of the AMO was formulated by Greatbatch and Zhang (1995) and Chen and

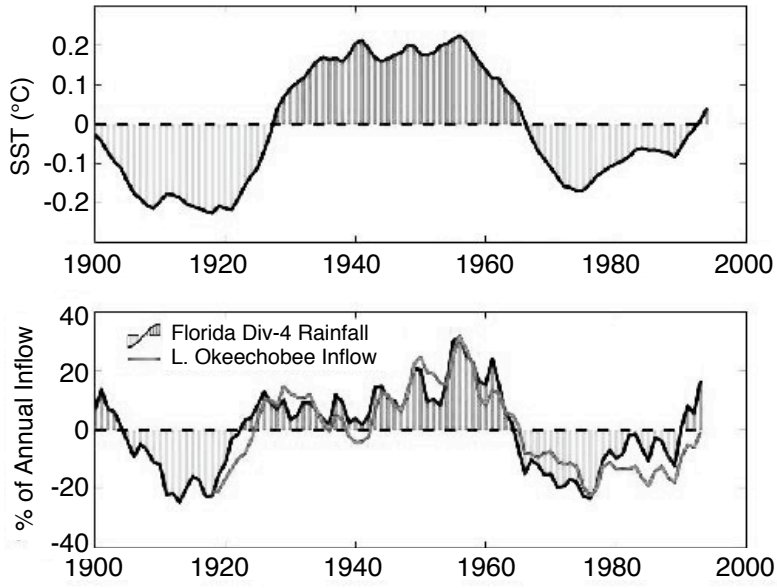

FIGURE 1.6: *Ten-year running means of (upper) the AMO index and (lower) Lake Okeechobee inflow (solid grey curve, expressed as a percentage of the long term annual mean) and the area-weighted Florida division 4 rainfall (shaded departures). Taken from Enfield et al. (2001).*

Ghil (1996) and consists of flow in an idealised three-dimensional northern hemispheric sector model forced only by a prescribed heat flux. It was suggested by Chen and Ghil (1996) that the oscillatory behavior arises from a Hopf bifurcation (an instability of the background steady flow to time-periodic disturbances), but it was not until the work of Huck and Vallis (2001) and te Raa and Dijkstra (2002) that the existence of this Hopf bifurcation was demonstrated. Analysis near the Hopf bifurcation revealed the precise physical mechanisms of variability as an out of phase response of zonal and meridional overturning anomalies to westward propagating temperature (or more generally, density) anomalies (te Raa and Dijkstra, 2002).

According to this mechanism, the multidecadal time scale of the variability arises from the east-west basin propagation time of the density anomalies. The pattern most favorable to amplification is the one where flow anomalies caused by density anomalies lead to density anomalies similar to the original ones. In that sense the mechanism is a generalised baroclinic instability (te Raa and Dijkstra, 2002). This description is supported by many model results in the same minimal model and slight extensions of it (Huck et al., 1999). Furthermore, the spectral origin of the multidecadal (normal) mode that eventually obtains a positive growth factor is fully understood by considering the small thermal forcing limit. The mode arises through mergers of stationary modes, called SST modes in Dijkstra (2006). The result of the merging is an oscillatory mode

which has a multidecadal time scale under realistic forcing conditions. This mode, and the mechanism by which it propagates, are discussed in chapter 2.

One of the missing elements in the minimal model theory, as developed so far, is the effect of atmospheric damping combined with atmospheric noise. There are important results from the top down approach using CGCMs which show that if noise is absent, there is no multidecadal variability (Delworth and Greatbatch, 2000), which, in the theory from the minimal model is interpreted as the multidecadal mode being damped. In chapter 3 the excitation of the AMO mode by noise is described. Spatial patterns and temporal coherence in the noise are tested for their effectiveness at exciting the mode.

The thesis then turns to observations of the AMO. While the characteristics of the AMO in terms of SST variability are more or less well established, basin wide variability in sub-surface layers has not been investigated due to the scarcity of data and the short length of the available time series compared to the estimated period of the variability. Motivated by the view of the AMO obtained from the model hierarchy, chapter 4 investigates westward propagation and lateral temperature differences in the sub-surface North Atlantic using XBT data.

The AMO is best characterised in terms of temperature anomalies, however studies of the AMO in observations are severely limited by the short length of the temperature record. Some of the longest time series available for the North Atlantic ocean are tide gauge measurements, which are examined in chapter 5. In addition this chapter compares the observed variability with sea surface height variability in a coupled climate model, which can be linked to the AMO.

Observations of multidecadal variability are not limited to the North Atlantic. The Arctic also shows variability on the time scales of interest. Chapter 6 examines the observational record of the North Atlantic and Arctic to determine the dominant time scales of variability. The links between variability in the two basins are also investigated in a coupled climate model. Chapter 7 then uses a different approach to studying Arctic variability, using an implicit model to find modes of variability in an idealised Arctic basin. Multidecadal modes are present in this simplified model Arctic, and their time scales and spatial patterns may be compared to variability found in a coupled climate model.

The central issues of this thesis may be summarised as follows:

- Excitation of the AMO (chapter 3)
- Characteristics of the AMO in observations and GCMs (chapters 4 and 5)
- Time scale of the variability in the North Atlantic and Arctic in observations and GCMs (chapter 6)
- Internal variability in the Arctic (chapter 7)

The thesis is concluded with a brief summary of the main results.

2

A STOCHASTIC DYNAMICAL SYSTEMS VIEW OF THE ATLANTIC MULTIDECADAL OSCILLATION

We provide a dynamical systems framework to understand the Atlantic Multidecadal Oscillation (AMO) and show that this framework is in many ways similar to that of the El Niño/Southern Oscillation. A so-called minimal primitive equation model is used to represent the Atlantic ocean circulation. Within this minimal model, we identify a normal mode of multidecadal variability that can destabilise the background climate state through a Hopf bifurcation. Next, we argue that noise is setting the amplitude of the sea surface temperature variability associated with this normal mode. The results provide support that a stochastic Hopf bifurcation is involved in the multidecadal variability as observed in the North Atlantic.

This chapter is based on:
A stochastic dynamical systems view of the Atlantic Multidecadal Oscillation, by H. A. Dijkstra, L. M. Frankcombe and A. S. von der Heydt, *Philosophical Transactions of the Royal Society A*, **366**, 2545-2560, 2008.
The Atlantic Multidecadal Oscillation: a stochastic dynamical systems view, by L. M. Frankcombe, H. A. Dijkstra and A. S. von der Heydt, in *Stochastic Physics and Climate Modelling* (ed. T. Palmer and P. Williams), pp. 287-306, Cambridge University Press, 2010.

2.1 A SIMPLE HOPF BIFURCATION

As mentioned in chapter 1, several pronounced large-scale patterns of variability on various time scales are known in the present climate system. On the interannual time scale, the El Niño/Southern Oscillation (ENSO) phenomenon provides a dominant pattern in sea surface temperature (SST) variability, which is localised in the equatorial Pacific (Philander, 1990). The Atlantic Multidecadal Oscillation (AMO), which is associated with a basin wide temperature anomaly in the North Atlantic, is the clearest phenomenon on the multidecadal time scale (Enfield et al., 2001). Of course, many ENSO cycles have been measured over the past decades, while the AMO is recorded over one cycle at most. A basic theory of both ENSO and the AMO should explain (i) the physics of the SST pattern and its propagation (if any), (ii) the physics of the dominant time scale of variability and (iii) the processes controlling the amplitude of the SST pattern.

For ENSO such a basic theory exists (Neelin et al., 1998). An important aspect in the development of the theory was the availability of a so-called minimal model of the coupled equatorial ocean-atmosphere system, the Zebiak-Cane (ZC) model (Zebiak and Cane, 1987). The solutions of the ZC model have been extensively analysed with the ocean-atmosphere coupling strength μ (the amount of wind stress per SST anomaly) as an important control parameter (Neelin et al., 1998). In the ZC model, the Tropical Pacific annual mean climate state can become unstable when μ crosses a critical value μ_c. When $\mu > \mu_c$, specific time-dependent perturbations grow in time leading to oscillatory behavior on an interannual time scale.

In terms of dynamical systems theory (Dijkstra, 2005), a Hopf bifurcation occurs at $\mu = \mu_c$ in the ZC model. The simplest dynamical system (Guckenheimer and Holmes, 1990) exhibiting such a bifurcation is the system

$$\frac{dx}{dt} = (\mu - \mu_c)x - \omega y - x(x^2 + y^2), \tag{2.1a}$$

$$\frac{dy}{dt} = (\mu - \mu_c)y + \omega x - y(x^2 + y^2), \tag{2.1b}$$

having two degrees of freedom (x, y). In polar coordinates (r, θ) with $x = r\cos\theta$ and $y = r\sin\theta$, the equations 2.1 can be written as

$$\frac{dr}{dt} = (\mu - \mu_c)r - r^3, \tag{2.2a}$$

$$\frac{d\theta}{dt} = \omega, \tag{2.2b}$$

For $\mu < \mu_c$, there is only one steady state $r = 0$ (or $x = y = 0$). For $\mu > \mu_c$, however, there are two solutions of the steady equation 2.2a, i.e., $r = 0$ and $r = \sqrt{\mu - \mu_c}$. The latter corresponds through equation 2.2b with a periodic orbit with an angular frequency ω and period $2\pi/\omega$. Hence at the Hopf bifurcation ($\mu = \mu_c$) periodic behavior with a frequency ω is spontaneously generated through an instability of the trivial solution $x = y = 0$.

In ENSO theory, when the ZC model is discretised under annual mean forcing, a large-dimensional dynamical system of the form

$$\frac{d\mathbf{X}}{dt} = \mathbf{f}(\mathbf{X}, \mu) \tag{2.3}$$

appears, where the state vector $\mathbf{X}$ consists of the dependent quantities in the model (for example, sea surface temperature, oceanic and atmospheric velocities) at each grid point and $\mathbf{f}$ contains the tendencies of all these state variables. In the same way as for the simple system (2.1), Hopf bifurcations are found by considering the stability of the annual mean Pacific climate state $\bar{\mathbf{X}}$ in the ZC model. Putting $\mathbf{X} = \bar{\mathbf{X}} + \tilde{\mathbf{X}}$ and $\tilde{\mathbf{X}} = e^{\sigma t}\hat{\mathbf{X}}$, we find by linearisation around $\bar{\mathbf{X}}$ that $\hat{\mathbf{X}}$ (the spatial pattern of the eigenmode) is determined by

$$\sigma\hat{\mathbf{X}} = \mathcal{J}(\bar{\mathbf{X}})\hat{\mathbf{X}}, \tag{2.4}$$

where $\mathcal{J}(\bar{\mathbf{X}})$ is the Jacobian matrix of $\mathbf{f}$ at $\bar{\mathbf{X}}$. In this case, a Hopf bifurcation occurs when a complex conjugate pair of eigenvalues $\sigma = \sigma_r + i\sigma_i$ crosses the imaginary axis as μ crosses μ_c. If the associated eigenvector is indicated by $\hat{\mathbf{X}} = \hat{\mathbf{X}}_r + i\hat{\mathbf{X}}_i$, then the periodic orbit at the Hopf bifurcation has the form

$$\mathbf{\Phi}(t) = \cos(\sigma_i t)\hat{\mathbf{X}}_r - \sin(\sigma_i t)\hat{\mathbf{X}}_i, \tag{2.5}$$

and $\mathbf{\Phi}(t)$ defines a propagating pattern with a period $2\pi/\sigma_i$. Note that the period is internally determined by processes in the system and not externally imposed.

As $\hat{\mathbf{X}}$ is a solution to equation 2.4 it is called a normal mode and in the case of the discretised ZC model it is usually referred to as the ENSO mode. By following this mode to smaller values of μ it is found (Jin and Neelin, 1993) that it splits up into two modes (in a so-called mode merger or mode splitter). One of these modes (an SST mode) is related to tendencies in the SST equation in the ZC model and the other mode (an equatorial ocean basin mode) is related to equatorial wave dynamics. The pattern of SST in the ENSO mode at μ_c is inherited from the SST mode while the interannual time scale is inherited from the equatorial basin mode (Jin and Neelin, 1993).

While in the ZC model, sustained ENSO type oscillations are found when $\mu > \mu_c$, there is no interannual time scale oscillatory behavior when $\mu < \mu_c$ as the annual mean Pacific climate state is stable. However, when noise (e.g., representing atmospheric weather) is applied in the ZC model, interannual oscillations are found for $\mu < \mu_c$. The simplest system exhibiting qualitatively the same behavior is the stochastic Itô extension of the simple system (equation 2.1), i.e., the dynamical system

$$dX_t = ((\mu - \mu_c)X_t - \omega Y_t - X_t(X_t^2 + Y_t^2))dt + \lambda\, dW_t, \tag{2.6a}$$

$$dY_t = ((\mu - \mu_c)Y_t + \omega X_t - Y_t(X_t^2 + Y_t^2))dt + \lambda\, dW_t, \tag{2.6b}$$

where λ is the amplitude of the additive noise and W_t is a Wiener process with increment dW_t. The expectation value $E[R_t]$, where $R_t^2 = X_t^2 + Y_t^2$, resulting from the stochastic integration of the system given by equations 2.6 is shown in figure 2.1 for several values of λ; the deterministic case is shown for $\lambda = 0$. Clearly, there is a response for values $\mu < \mu_c$ which increases with increasing noise level λ.

The effect of noise on the variability in the ZC model has been systematically studied by Roulston and Neelin (2000) and the results are qualitatively similar to those in figure 2.1. For values $\mu < \mu_c$, white noise in the wind stress over the equatorial Pacific is able to excite the ENSO mode to substantial amplitude while for values $\mu > \mu_c$ there are sustained oscillations which are not much affected by the noise. In both cases, the spatial pattern and the time scale of propagation associated with the interannual variability do

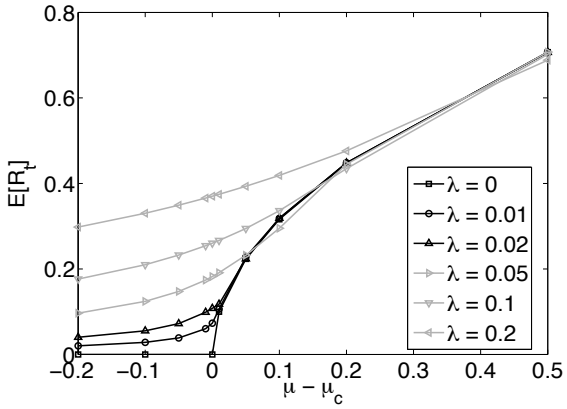

FIGURE 2.1: *Response near a stochastic Hopf bifurcation at $\mu = \mu_c$ monitored through solutions of (2.6). In the deterministic case ($\lambda = 0$), $r = 0$ for $\mu < \mu_c$. When noise is included, the expectation value $E[R_t]$, where $R_t^2 = X_t^2 + Y_t^2$, increases with increasing λ for any value of $\mu - \mu_c$. In the cases with stochastic forcing $E[R_t]$ is determined over a long time interval integration.*

not depend on the precise noise characteristics as both are coupled to the ENSO mode. Stochastic noise in the wind stress mainly affects the amplitude of the pattern (Roulston and Neelin, 2000).

Having introduced this stochastic dynamical systems view of ENSO, a similar framework can be applied to the AMO. The minimal model of the AMO is described in section 2.2. It is show in section 2.3 that a Hopf bifurcation occurs in this model, leading to multidecadal periodic oscillations. The origin of the AMO mode giving rise to this variability and the physics of the time scale and pattern are provided in section 2.3.1. The effect of including continental geometry in the model is shown in section 2.3.2 and a summary and discussion of the dynamical systems framework of the AMO follows in section 2.4.

2.2 THE MINIMAL PRIMITIVE EQUATION MODEL

A minimal model of the AMO was formulated by Greatbatch and Zhang (1995) and Chen and Ghil (1996) and consists of flow in an idealised three-dimensional northern hemispheric sector model forced only by a prescribed heat flux. We therefore consider ocean flows in a model domain on the sphere bounded by the longitudes $\phi_w = 286^\circ$ (74°W) and $\phi_e = 350^\circ$ (10°W) and by the latitudes $\theta_s = 10^\circ$N and $\theta_n = 74^\circ$N; the ocean basin has a constant depth H. The flows in this domain are forced by a restoring heat flux Q_{rest} (in Wm^{-2}) given by

$$Q_{rest} = -\lambda_T (T^* - T_S) \tag{2.7}$$

where λ_T (in Wm^{-2}K^{-1}) is a constant surface heat exchange coefficient. The heat flux Q_{rest} is proportional to the temperature difference between the ocean temperature T^*

taken at the surface and a prescribed atmospheric temperature T_S, chosen as

$$T_S(\phi,\theta) = T_0 + \frac{\Delta T}{2}\cos\left(\pi\frac{\theta-\theta_s}{\theta_n-\theta_s}\right)$$

where $T_0 = 15°\text{C}$ is a reference temperature and ΔT is the temperature difference between the southern and northern latitude of the domain. The forcing is distributed as a body forcing over the first (upper) layer of the ocean having a depth H_m.

Temperature differences in the ocean cause density differences according to

$$\rho = \rho_0(1-\alpha_T(T^*-T_0))$$

where α_T is the volumetric expansion coefficient and ρ_0 is a reference density. Inertia is neglected in the momentum equations because of the small Rossby number, we use the Boussinesq and hydrostatic approximations and represent horizontal and vertical mixing of momentum and heat by constant eddy coefficients. With r_0 and Ω being the radius and angular velocity of the Earth, the governing equations for the zonal, meridional and vertical velocity u, v and w, the dynamic pressure p (the hydrostatic part has been subtracted) and the temperature $T = T^* - T_0$ become

$$-2\Omega\, v\sin\theta + \frac{1}{\rho_0 r_0\cos\theta}\frac{\partial p}{\partial\phi} = A_V\frac{\partial^2 u}{\partial z^2} + A_H L_u(u,v) \tag{2.8a}$$

$$2\Omega\, u\sin\theta + \frac{1}{\rho_0\, r_0}\frac{\partial p}{\partial\theta} = A_V\frac{\partial^2 v}{\partial z^2} + A_H\, L_v(u,v) \tag{2.8b}$$

$$\frac{\partial p}{\partial z} = \rho_0\, g\, \alpha_T\, T \tag{2.8c}$$

$$\frac{1}{r_0\cos\theta}\left(\frac{\partial u}{\partial\phi} + \frac{\partial(v\cos\theta)}{\partial\theta}\right) + \frac{\partial w}{\partial z} = 0 \tag{2.8d}$$

$$\frac{DT}{dt} - \nabla_H\cdot(K_H\nabla_H T) - \frac{\partial}{\partial z}\left(K_V\frac{\partial T}{\partial z}\right) = \frac{(T_S-T^*)}{\tau_T}\mathcal{H}(\frac{z}{H_m}+1) \tag{2.8e}$$

where $\mathcal{H}$ is a continuous approximation of the Heaviside function, C_p the constant heat capacity, g is the gravitational acceleration and $\tau_T = \rho_0 C_p H_m/\lambda_T$ is the surface adjustment time scale of heat. In these equations, A_H and A_V are the horizontal and vertical momentum (eddy) viscosity and K_H and K_V the horizontal and vertical (eddy) diffusivity of heat, respectively. In addition, the operators in the equations above are defined as

$$\frac{D}{dt} = \frac{\partial}{\partial t} + \frac{u}{r_0\cos\theta}\frac{\partial}{\partial\phi} + \frac{v}{r_0}\frac{\partial}{\partial\theta} + w\frac{\partial}{\partial z} \tag{2.9a}$$

$$\nabla_H\cdot(K_H\nabla_H) = \frac{1}{r_0^2\cos\theta}\left[\frac{\partial}{\partial\phi}\left(\frac{K_H}{\cos\theta}\frac{\partial}{\partial\phi}\right) + \frac{\partial}{\partial\theta}\left(K_H\cos\theta\frac{\partial}{\partial\theta}\right)\right] \tag{2.9b}$$

$$L_u(u,v) = \nabla_H^2 u + \frac{\cos 2\theta}{r_0^2\cos^2\theta}u - \frac{2\sin\theta}{r_0^2\cos^2\theta}\frac{\partial v}{\partial\phi} \tag{2.9c}$$

$$L_v(u,v) = \nabla_H^2 v + \frac{\cos 2\theta}{r_0^2\cos^2\theta}v + \frac{2\sin\theta}{r_0^2\cos^2\theta}\frac{\partial u}{\partial\phi} \tag{2.9d}$$

2Ω	=	$1.4 \cdot 10^{-4}$	$[s^{-1}]$	r_0	=	$6.4 \cdot 10^{6}$	$[m]$
H	=	$4.0 \cdot 10^{3}$	$[m]$	τ_T	=	$3.0 \cdot 10^{1}$	$[days]$
α_T	=	$1.0 \cdot 10^{-4}$	$[K^{-1}]$	g	=	9.8	$[ms^{-2}]$
A_H	=	$1.6 \cdot 10^{5}$	$[m^2 s^{-1}]$	T_0	=	15.0	$[^\circ C]$
ρ_0	=	$1.0 \cdot 10^{3}$	$[kgm^{-3}]$	A_V	=	$1.0 \cdot 10^{-3}$	$[m^2 s^{-1}]$
K_H	=	$1.0 \cdot 10^{3}$	$[m^2 s^{-1}]$	K_V	=	$1.0 \cdot 10^{-4}$	$[m^2 s^{-1}]$
C_p	=	$4.2 \cdot 10^{3}$	$[J(kgK)^{-1}]$	ΔT	=	20.0	$[K]$

TABLE 2.1: *Standard values of parameters used in the minimal primitive equation model.*

Slip conditions and zero heat flux are assumed at the bottom boundary, while at all lateral boundaries no-slip and zero heat flux conditions are applied. As the forcing is represented as a body force over the first layer, slip and zero heat flux conditions apply at the ocean surface. Hence, the boundary conditions are

$$z = -D, 0 \quad : \qquad \frac{\partial u}{\partial z} = \frac{\partial v}{\partial z} = w = \frac{\partial T}{\partial z} = 0 \tag{2.10a}$$

$$\phi = \phi_w, \phi_e \quad : \qquad u = v = w = \frac{\partial T}{\partial \phi} = 0 \tag{2.10b}$$

$$\theta = \theta_s, \theta_n \quad : \qquad u = v = w = \frac{\partial T}{\partial \theta} = 0 \tag{2.10c}$$

The parameters for the standard case are the same as in typical large-scale low-resolution ocean general circulation models and their values are listed in table 2.1.

2.3 THE AMO MODE

To determine whether Hopf bifurcations occur within the minimal primitive equation model of the previous section, methods from numerical bifurcation theory are used (Dijkstra, 2005). First, the governing equations (equations 2.8) and boundary conditions (equations 2.10) are discretised on an Arakawa B-grid using central spatial differences. In the results in this section, we use a horizontal resolution of 4°. An equidistant grid with 16 levels is used in the vertical so that the first layer thickness $H_m = 250$ m. The discretised system of equations can be written in the form of 2.3 and a $16 \times 16 \times 16$ grid with 5 unknowns per point (u, v, w, p and T) leads to a dynamical system of dimension (the number of degrees of freedom) 20,480.

The steady equations of the form of equation 2.3 are solved using a pseudo-arclength continuation method (Keller, 1977). As primary control parameter μ, we choose the equator-to-pole temperature difference ΔT. For every value of ΔT we calculate a steady solution of the minimal model under the restoring flux Q_{rest} in equation 2.7. For each steady flow pattern, the maximum of the meridional overturning streamfunction (ψ_M) is calculated and it is plotted versus ΔT in figure 2.2(a). The meridional overturning streamfunction for $\Delta T = 20$ K is plotted in figure 2.2(b). The maximum of ψ occurs at about 55°N and the amplitude is about 16 Sv.

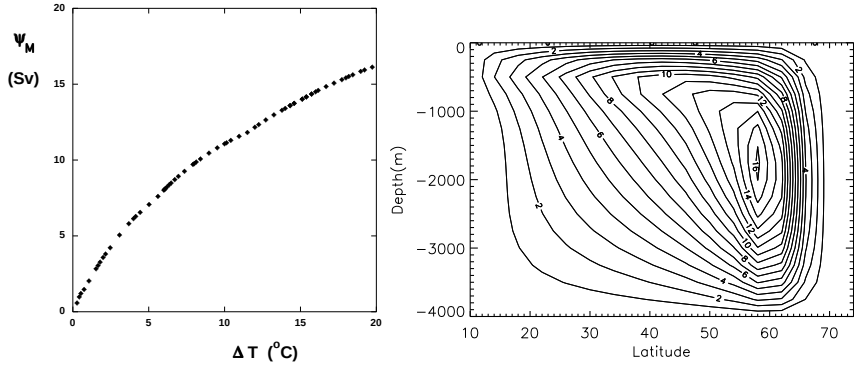

FIGURE 2.2: *Plot of the maximum meridional overturning (ψ_M) of the steady solution (in Sv) versus the equator-to-pole temperature difference ΔT ($^\circ C$) under restoring conditions (left) and plot of the meridional overturning streamfunction (contour values in Sv) for $\Delta T = 20$ ($^\circ C$; right).*

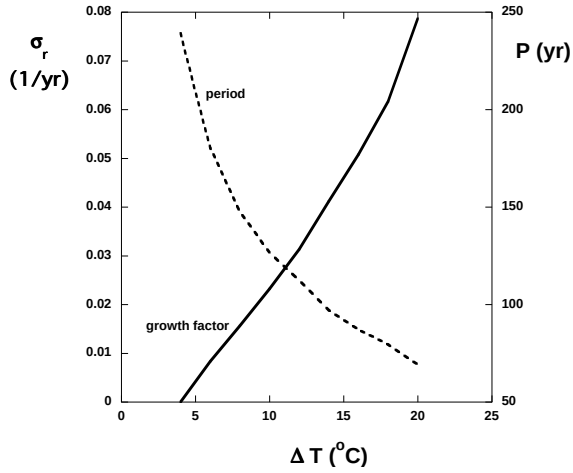

FIGURE 2.3: *Growth factor σ_r (in yr^{-1}, drawn) and period $P = 2\pi/\sigma_i$ (in yr, dashed) versus ΔT (in $^\circ C$) of the AMO mode in the minimal primitive equation model under prescribed flux conditions.*

Next, we diagnose the ocean-atmosphere heat flux Q_{pres} of each of the steady solutions and compute the linear stability of the steady solution under the heat flux Q_{pres} (where the subscript refers to 'prescribed'). To determine the linear stability we solve for the 'most dangerous' modes of the problem (equation 2.4), i.e., those with real part closest to the imaginary axis and order the eigenvalues $\sigma = \sigma_r + i\sigma_i$ according to the magnitude of their real part σ_r (the growth factor). The growth rate and period of the mode with the largest growth factor are plotted versus ΔT in figure 2.3.

For $\Delta T = 20^\circ$C, the AMO mode has a positive growth factor and hence the background state, of which the meridional overturning streamfunction was shown in figure 2.2(b), is unstable to the AMO mode. The period of the AMO mode is about 67 years at

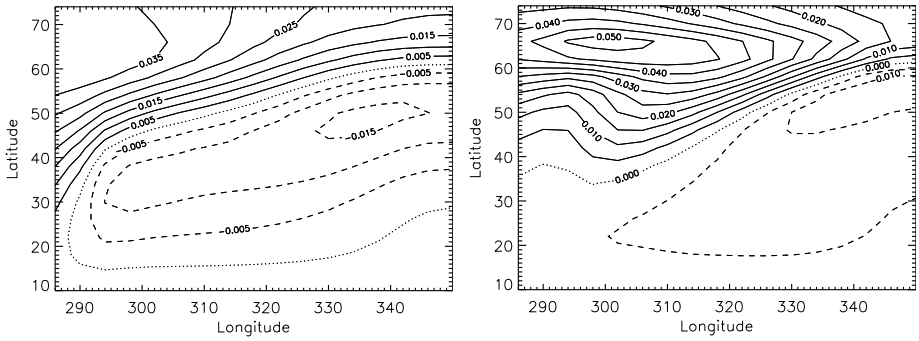

FIGURE 2.4: *SST pattern of the real part the AMO mode for $\Delta T = 4^\circ C$ (near Hopf bifurcation; left) and $\Delta T = 20^\circ C$ (right). Negative contours are dashed, the zero contour is dotted. Note that amplitudes are arbitrary.*

$\Delta T = 20^\circ$C, and it decreases with increasing ΔT (figure 2.3). From figure 2.3, we see also that the growth factor of the AMO mode decreases strongly with decreasing ΔT and becomes negative near $\Delta T_c \approx 4^\circ$C, where the Hopf bifurcation occurs. For $\Delta T < \Delta T_c$, the steady states are therefore linearly stable under the prescribed flux Q_{pres}.

It was shown in Dijkstra (2006) that for small ΔT, the angular frequency of the AMO mode becomes zero and the complex conjugate pair of eigenvalues splits up into two real eigenvalues. The paths of the two different modes can be followed to the $\Delta T = 0$ limit, where the eigensolutions connect to those of the diffusion operator of the temperature equation, called SST modes in Dijkstra (2006). These SST modes can be ordered according to their zonal, meridional and vertical wavenumber and it was found that the AMO mode connects to the $(0, 0, 1)$ SST mode and the $(1, 0, 0)$ SST mode at $\Delta T = 0$.

For each eigenvalue σ associated with the AMO mode, there is a corresponding eigenvector $\mathbf{X} = \mathbf{X}_r + i\mathbf{X}_i$ according to equation 2.4. In figure 2.4, the sea surface temperature field of the real part of the eigenvector ($\mathbf{X}_r$) of the AMO mode is plotted for $\Delta T = 4^\circ$C (near Hopf bifurcation) and for $\Delta T = 20^\circ$C. A comparison of the pattern in figure 2.4(b) and the one in figure 4d in te Raa and Dijkstra (2002) demonstrates that the AMO mode here is the multidecadal mode as described in detail in te Raa and Dijkstra (2002). With increasing ΔT, the pattern becomes more localised in the northwestern part of the basin.

2.3.1 PROPAGATION OF THE MODE

The physical mechanism of propagation of the AMO mode was presented in te Raa and Dijkstra (2002). This mechanism holds for every ΔT for which an oscillatory AMO mode is present (cf. figure 2.4). A slight generalisation (compared to that in te Raa and Dijkstra (2002)) of this mechanism is provided with help of figure 2.5. A warm anomaly in the north-central part of the basin causes a positive meridional perturbation temperature gradient, which induces – via the thermal wind balance – a negative zonal surface flow (figure 2.5(a)). The anomalous anticyclonic circulation around the warm anomaly causes southward (northward) advection of cold (warm) water to the east (west) of the anomaly, resulting in westward phase propagation of the warm anomaly.

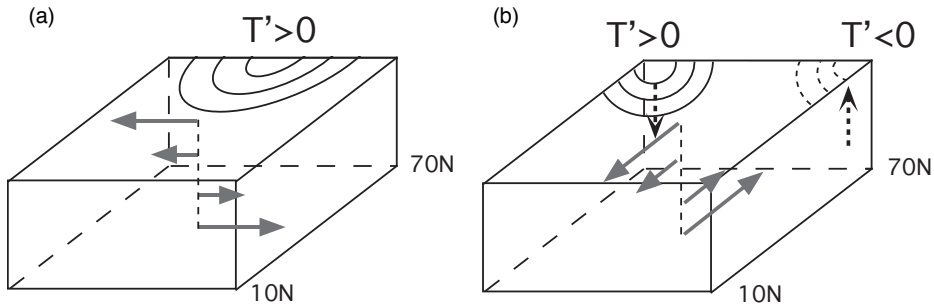

FIGURE 2.5: *Schematic diagram of the oscillation mechanism associated with the multidecadal mode caused by the westward propagation of the temperature anomalies T'. The phase difference between (a) and (b) is about a quarter period. See text and te Raa and Dijkstra (2002) for a further explanation.*

Due to this westward propagation, the zonal perturbation temperature gradient becomes negative, inducing a negative surface meridional flow (figure f:mech(b)). The resulting upwelling (downwelling) perturbations along the northern (southern) boundary cause a negative meridional perturbation temperature gradient, inducing a positive zonal surface flow, and the second half of the oscillation starts. The crucial elements in this oscillation mechanism are the phase difference between the zonal and meridional surface flow perturbations, and the westward propagation of the temperature anomalies (te Raa and Dijkstra, 2002). The presence of salinity does not essentially change this mechanism; density anomalies will take over the role of temperature anomalies in the description above.

The westward propagation of subsurface anomalies is characteristic of the variations. This westward propagation is associated with Rossby type dynamics but the background potential vorticity gradient is set by the background temperature gradient. In idealised (three-dimensional primitive equation) ocean models the background meridional overturning circulation can become unstable due to growth of such a propagating and oscillatory perturbation (te Raa and Dijkstra, 2002; Sévellec et al., 2009).

2.3.2 DEFORMATION OF THE SPATIAL PATTERN BY CONTINENTS

In order to compare the AMO mode of variability in the simple model to multidecadal variability found in GCMs as well at that observed in the real ocean we need to know how the spatial pattern of the AMO mode is modified by the presence of continents. For this we use the same model setup as in section 2.3 with the resolution increased to $2^\circ \times 2^\circ$ and with 24 levels in the vertical. The model still has a uniform depth of 4000m but continental boundaries are now included. Under prescribed flux boundary conditions the oscillatory mode has a period of about 42 years and a spatial pattern which is shown in the first two EOFs of SST in figure 2.6. The variability is still concentrated in the northwestern part of the basin but the pattern has been deformed by the continents.

Following Kushnir (1994) we take the difference in sea surface temperatures between the warm and cool phases of the AMO in both the model and observations. In the model

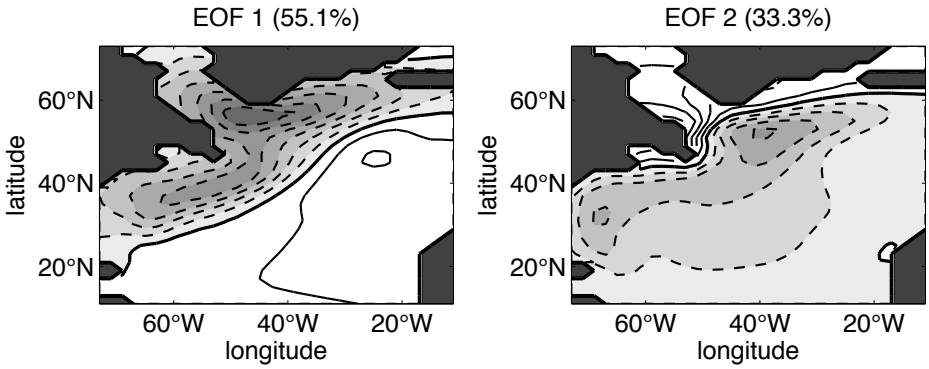

FIGURE 2.6: *First two EOFs of sea surface temperature for the model configuration with continents, which together explain almost 90% of the variance. Contour interval is* $0.5^\circ C$*, negative values are shaded.*

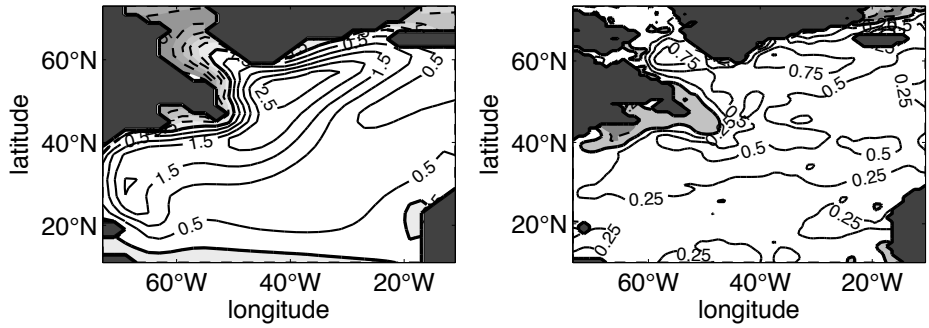

FIGURE 2.7: *The pattern of the AMO in SST, with negative SSTs shaded. (a) Difference between the pattern of SST from years with maximum and minimum AMO indices in the model, contour interval* $0.5^\circ C$*. (b) SST averaged over the years 1970 – 1984 (negative AMO index) subtracted from the years 1950 – 1964 (positive AMO index), contour interval* $0.25^\circ C$*.*

the SSTs from the year with the lowest AMO index were subtracted from those from the year with the highest AMO index (where the AMO index is the average SST over the North Atlantic, as defined by Enfield et al. (2001)). The resulting pattern is shown in figure 2.7(a). Observed SSTs were taken from the HadISST dataset (Rayner et al., 2003) and averaged over 1950 – 1964 for the warm period and 1970 – 1984 for the cool period. The pattern that results when subtracting the cool from the warm period is shown in figure 2.7(b). There are notable similarities between the two patterns, with negative anomalies around Newfoundland and north of Iceland and the largest positive anomalies just south of Greenland. Several differences can also be observed. Firstly the pattern is not as coherent in observations as in the model. However, this is only to be expected since the mode in the real ocean is thought to be damped and therefore its spatial pattern, amplitude and period will not be as defined as in the model, which is in the supercritical regime for this mode.The effect of atmospheric noise also contributes to the observed

pattern, whereas it is not included in this simple model.

Secondly, there are small differences in the shape of the pattern, for example in observations the cold anomaly is centered much more around Nova Scotia and Newfoundland than in the model, where it is more intense further north in the Labrador Sea. This is also not unexpected since the model and observed climatologies are not identical. In particular the Gulf Stream separation point in such a coarse resolution model is too far to the north compared to observations. This difference in mean states leads to differences in the spatial patterns of variability as well.

Therefore, despite some differences, the overall effect of including continents in the simple model is to deform the spatial pattern of the AMO mode into a form that resembles observations, giving us confidence that the multidecadal mode in the simple model is indeed the same phenomenon which gives rise to multidecadal variability in the real ocean.

2.4 SUMMARY AND DISCUSSION

In this chapter is has been shown that a similar dynamical systems framework can be formulated for the Atlantic Multidecadal Oscillation (AMO) as for ENSO. The minimal primitive equation model as presented in section 2.2 takes the same role in the AMO theory as the Zebiak-Cane model in ENSO theory. In the ZC model, the ocean-atmosphere coupling strength μ serves as the main control parameter, while in the AMO theory the atmospheric damping time scale of SST anomalies, here mimicked by the parameter γ, has that role.

In both minimal models of ENSO and the AMO there is a normal mode, the 'most dangerous' mode (having the largest growth factor) which is able to destabilise the background state. Interestingly, both ENSO and AMO variability arise through normal rather than non-normal modes (Zanna and Tziperman, 2008; Sévellec et al., 2009). We do not consider non-normal modes of the system since we wish to study sustained oscillations rather than the exponentially decaying variability found when non-normal modes are excited. Secondly, the types of non-normal modes that are found depend on the norm that is chosen, this is not the case for the normal modes.

The nature of the ENSO mode which destabilises the Pacific mean state at sufficiently large coupling strength is a merger between an ocean basin mode and a stationary SST mode. The mechanism of the ENSO mode propagation and time scale is known to be related to the dominant feedback mechanism (thermocline, upwelling, zonal advection) and the equatorial wave propagation (Neelin et al., 1998). In the AMO minimal model, the 'most dangerous' normal mode is called the AMO mode and it results from a merger of two SST modes at small ΔT (Dijkstra, 2006). The propagation of the AMO mode is determined by a thermal wind response to a propagating temperature (or density) anomaly and the multidecadal time scale is set by the east-west propagation time of the temperature (or density) anomalies. The oscillation can be characterised by an out of phase response of the meridional and zonal overturning anomalies as shown in figure 2.5.

It is not known whether the Tropical Pacific climate state is near the Hopf bifurcation (Fedorov and Philander, 2000). Because of slow variations of the background state it is possible that one ENSO event could occur in the supercritical regime (with less impact

of noise) and the next in the subcritical regime (with noise controlling its amplitude). Similarly, it is not known whether the atmospheric damping time scale of temperature anomalies in the North Atlantic induces a positive or negative growth factor of the AMO mode.

When additive noise is included, the ENSO mode can be excited below critical conditions (Roulston and Neelin, 2000) and the ENSO variability results from a stochastic Hopf bifurcation as introduced in section 2.1. The results here make a case that a Hopf bifurcation also occurs for the AMO. The inclusion of stochastic noise in the minimal model of the AMO will be discussed in the next chapter.

3

Noise Induced Multidecadal Variability in the North Atlantic: Excitation of Normal Modes

In this paper we propose that the stochastic excitation of a multidecadal internal ocean mode is at the origin of the multidecadal sea surface temperature variability in the North Atlantic. We study the excitation processes of the spatial sea surface temperature pattern associated with this multidecadal mode within an idealised three-dimensional model by adding noise to the surface heat-flux forcing. In the regime where the internal mode is damped, the amplitude of its sea surface temperature pattern depends on the type of noise forcing applied. While the mode is weakly excited by white noise, only the introduction of spatial and temporal coherence in the forcing, in particular those with characteristics of the North Atlantic Oscillation, causes the amplitude of the variability to increase to levels comparable to those observed. Within this idealised model the physical mechanism of the excitation can be determined: the presence of the noise rectifies the background state and consequently changes the growth factor of the internal mode.

This chapter is based on:
Noise-induced multidecadal variability in the North Atlantic: Excitation of normal modes, by L. M. Frankcombe, H. A. Dijkstra and A. S. von der Heydt, *Journal of Physical Oceanography*, **39**, 220-233, 2009.

3.1 INTRODUCTION

As discussed in chapter 1 the Atlantic Multidecadal Oscillation (AMO) is associated with a particular time scale and spatial pattern (Enfield et al., 2001; Kushnir, 1994). Delworth and Greatbatch (2000) found that the AMO in the GFDL R15 coupled model arose due to low-frequency variability in the atmosphere which forced an internal ocean mode. This result has since been found in a range of other models although the AMO time scale differs between models. Different mechanisms have also been reported (Eden and Jung, 2001; Cheng et al., 2004; Dong and Sutton, 2005; Jungclaus et al., 2005). The problem with analysing the AMO in such models is that many fields are varying at the same time, making it difficult to separate cause from effect.

Another approach to studying the AMO uses a 'minimal model', the simplest possible model in which an AMO mode can appear. This minimal model of the AMO was described in the previous chapter. In this minimal model flow is forced only by a prescribed heat flux, and the oscillatory variability arises through a Hopf bifurcation. A similar Hopf bifurcation also appears in the minimal model of ENSO, where additive noise may excite the variability even in the regime where the oscillations are damped. In this chapter the effect of additive noise on the minimal mode of the AMO is studied.

The minimal model of the AMO does not capture the effects of continental geometry, bottom topography, salinity, wind-driven flow or dynamical interaction with the atmosphere. The single-hemispheric geometry is also quite constraining as it cannot capture the cross-equatorial or interbasin exchanges. Furthermore, atmospheric damping in the minimal model is assumed to be negligible. This is far from realistic; a reasonable value of the damping time scale of SST anomalies is about 30 days (Barsugli and Battisti, 1998). The effect of salinity and wind forcing, continental geometry, bottom topography and atmospheric damping were considered in several studies (te Raa and Dijkstra, 2003; te Raa et al., 2004) which showed that the Hopf bifurcation is robust and that the mechanism as described in te Raa and Dijkstra (2002) still underlies the variability in these extended models (Dijkstra et al., 2006). As expected, the presence of bottom topography and/or atmospheric damping decreases the growth factor of the multidecadal mode and hence the Hopf bifurcation is shifted to a parameter regime of higher forcing/lower dissipation. The deformation of the pattern of the multidecadal mode in model situations with realistic continental geometry even tends to look like the pattern as in Kushnir (1994). The effect of cross-equatorial flow and interbasin exchange is to localise the variability in the North Atlantic, as was shown in von der Heydt and Dijkstra (2007). The spectral view of the SST mergers leading to the multidecadal modes in these situations was described in Dijkstra and von der Heydt (2007).

One of the missing elements in the minimal model theory as developed so far is the effect of atmospheric damping combined with atmospheric noise. There are important results from the top down approach using CGCMs which show that if noise is absent, there is no multidecadal variability (Delworth and Greatbatch, 2000), which, in the theory from the minimal model is interpreted as the multidecadal mode being damped. When only high-pass filtered atmospheric forcing is driving the ocean component of the CGCM of Delworth and Greatbatch (2000), the multidecadal variability is much weaker than in the coupled case. Low-frequency variability in the forcing is needed to obtain multidecadal variability in the ocean-only case. This result motivates the study in this paper, where we consider the physics of the excitation processes of the multidecadal

mode in the minimal model for cases where atmospheric damping is strong enough to damp the multidecadal mode. By introducing noise into the surface boundary condition we can systematically investigate the effects of spatial and temporal correlations in the noise on the amplitude of variability excited, while the simplicity of the model and boundary conditions allow us to study the excitation of the mode over a whole range of atmospheric damping strengths.

The effect of noise on idealised ocean models was considered in a more limited context by Griffies and Tziperman (1995) and Saravanan and McWilliams (1997, 1998). Saravanan and McWilliams (1998) studied the effect of noise in combination with passive advection in the ocean. Both Griffies and Tziperman (1995) and Saravanan and McWilliams (1997) studied models, a four-box model and a zonally averaged model respectively, where the multidecadal mode considered here cannot exist. In these models, the only normal modes consist of two-dimensional loop oscillations for which the presence of both temperature and salt is required (Winton and Sarachik, 1993). In more general, three dimensional ocean models these normal modes have a centennial timescale (te Raa and Dijkstra, 2003) and appear alongside the three-dimensional normal mode with a multidecadal timescale that is under investigation in this study. This three dimensional multidecadal mode does not exist in a two dimensional model because the zonal direction is essential for its existence. The three dimensional mode involves westward propagation of temperature anomalies at the surface, while two dimensional loop oscillations occur due to the advection of salinity anomalies by the overturning circulation. These differences in propagation mean that the addition of noise in the surface boundary condition can be expected to have significantly different effects on the two modes.

It will be shown here that colored noise is needed to excite the pattern of the multidecadal mode to sufficient amplitude and that the spatial/temporal statistical properties of the North Atlantic Oscillation can favorably excite the multidecadal mode to the amplitudes observed. This excitation is thought to occur through the modification of the growth factor of the multidecadal mode through rectification of the background state by the noise. In section 3.2 the minimal model set-up is described briefly, with focus on the surface boundary conditions for temperature. In section 3.3 the results are presented for the deterministic (no noise) case and for the variability appearing when noise, either uncorrelated or correlated in space and time, is included in the forcing. In addition, we take a look at how the background state affects the stability of the mode. This is followed by the discussion and conclusions in section 3.4.

3.2 FORMULATION

All the simulations discussed below were carried out using version 3.1 of the GFDL Modular Ocean Model (MOM). An extensive description of the equations, their discretisation and the solution methods in this model is given in Pacanowski and Griffies (2000). The model domain used here consists of a single hemispheric $64^\circ \times 64^\circ$ basin covering the sector from $\theta_s = 10^\circ$N to $\theta_n = 74^\circ$N and $\phi_w = 74^\circ$W to $\phi_e = 10^\circ$W. Bottom topography is not included and the basin is 4000 m deep everywhere. The resolution of the model is 4° in both latitude and longitude. A stretched grid with 16 layers is used in the vertical so that the first four layers have a thickness of 50 m, with the thickness then increasing to 583 m in the lowest level. The rigid lid version of the model is used, so

the vertical velocity vanishes at the ocean surface. Buoyancy fluxes through the bottom and lateral walls are zero. No-slip conditions are imposed at the lateral boundaries and slip conditions are imposed on the bottom boundaries.

Since heat-flux forcing has been found to dominate over the freshwater and momentum flux components in causing the SST variability (Delworth and Greatbatch, 2000; Eden and Jung, 2001), we neglect freshwater and momentum flux forcing in this model. Salinity is set to a uniform value of 35.0 psu and wind-stress forcing has been set to zero in all runs. Horizontal eddy viscosity A_H is set to 1.6×10^5 m^2/s, vertical eddy viscosity A_V is 1.0×10^{-3} m^2/s and horizontal eddy diffusivity K_H is 1.0×10^3 m^2/s, as in Dijkstra (2006). Vertical eddy diffusivity K_V is 1.0×10^{-4} m^2/s. This value of K_V is slightly smaller than that used in Dijkstra (2006) and gives a more realistic MOC strength. An implicit convective adjustment scheme is used in the model, in which vertical eddy diffusivity is increased in areas of unstable stratification.

The model is initially run for 6000 years under restoring conditions for temperature. In these simulations, a restoring heat flux Q_{rest} of the form

$$Q_{rest} = \frac{\lambda_T}{\rho C_p H_m}\big(T_S(\theta) - T\big)$$

is used, where C_p is the specific heat capacity of water at constant pressure, H_m is the depth of the first layer in the model, ρ is the constant Boussinesq density of water used by the ocean model and λ_T is an air-sea exchange coefficient. The restoring timescale for temperature $\tau_T^{rest} = \rho C_p H_m/\lambda_T$ in the model is 30 days. The temperature profile $T_S(\theta)$ is given by

$$T_S(\theta) = 15 + 10\cos\Big(\pi\frac{\theta - \theta_s}{\theta_n - \theta_s}\Big). \tag{3.1}$$

This means that the temperature varies between 25°C at the southern boundary and 5°C at the northern boundary, i.e., the meridional temperature difference is 20°C.

The meridional overturning streamfunction of the equilibrium state has a maximum of about 19.2 Sv and is plotted in figure 3.1(a). The surface heat flux needed to keep the system in equilibrium is then diagnosed. We call this flux Q_{pres} and it is plotted in figure 3.1(b) where a positive value indicates that heat is entering the ocean. Over most of the basin the heat flux into the ocean decreases with increasing latitude. The strongest heat loss from the ocean occurs over the western boundary current.

Prescribing the flux Q_{pres} as a boundary condition is equivalent to increasing the restoring timescale of the surface temperature to infinity (i.e. reducing the damping to zero). We know that under restoring boundary conditions the multidecadal mode is damped, but under prescribed flux boundary conditions it can have a positive growth rate (te Raa and Dijkstra, 2003) so that oscillations spontaneously occur. Restoring and prescribed flux conditions are thus the two limits of damping by the atmosphere of the ocean. To study what happens between these limits a new general boundary condition for surface heat flux is applied:

$$Q = (1-\gamma)Q_{rest} + \gamma Q_{pres}, \tag{3.2}$$

where Q_{rest} and Q_{pres} are the restoring and prescribed heat fluxes, respectively. The relative amounts of these fluxes, and therefore the amount of damping, are changed using the control parameter γ in (3.2).

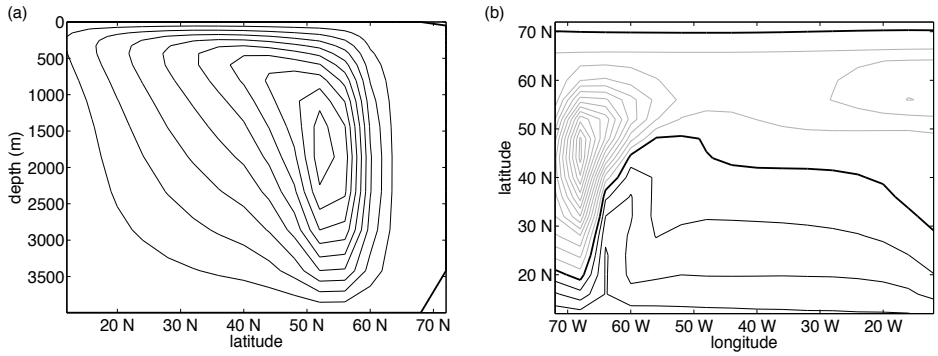

FIGURE 3.1: *(a) Meridional overturning streamfunction (in Sv) of the background state, obtained after spin-up of the model using restoring boundary conditions (contour interval 2 Sv). (b) Surface heat flux (in W/m^2) diagnosed at the end of the spin-up run under restoring conditions and later used as the prescribed heat flux. Black contours indicate positive heat flux (heat flux into the ocean), grey contours indicate negative heat flux, contour interval 10 W/m^2, zero contour is bold.*

A value of γ representative of the real ocean can be estimated by examining the damping timescale of the upper layer of the ocean. The effective damping timescale τ_T is defined as

$$\tau_T = (1-\gamma)\frac{C_p H_m \rho}{\lambda_T}.$$

Using variables from the model ($\rho = 1 \times 10^3$ kg/m^3, $C_p = 3990$ Jkg^{-1}K^{-1}, $H_m = 50$ m, $\tau_T = 30$ days) and $\lambda_T = 20$ Wm^{-2}K^{-1} as a representative midlatitude value (Barsugli and Battisti, 1998) gives a value of $\gamma \approx 0.74$.

3.3 RESULTS

We will first consider the deterministic case (section 3.1) and then consider the effect of only spatial coherence of the noise forcing (section 3.2). In section 3.3, we study the impact of both spatial and temporal coherence in the noise forcing and then in section 3.4 we examine the role of rectification of the background state in the excitation of the multidecadal mode. The various runs carried out are listed in table 3.1 along with their γ values and the temporal and spatial characteristics of the noise included in the heat flux. Variations in SST are analysed in terms of averages over the surface area [$46°$N – $62°$N] $\times$ [$74°$W – $50°$W] in the northwestern part of the basin. The meridional overturning circulation (MOC) strength is measured at the location where the MOC is maximal at the end of the spinup run (figure 3.1(a)). Patterns of variability are analysed using the Multichannel Singular Spectral Analysis (MSSA) toolkit (Ghil et al., 2002b).

Run name	γ value	Type of noise	Spatial pattern of noise
Q_W	0.7 – 1.0	white	none
$Q_{S,W}$	0.7 – 1.0	white	sinusoidal
$Q_{S,NAO}$	0.0 & 0.8	NAO index, 30 day timescale	sinusoidal
$Q_{S,rNAO}$	0.8	reversed NAO index, 30 day timescale	sinusoidal
Q_{S,W_1}	0.8	white, 1 day timescale	sinusoidal
$Q_{S,W_{10}}$	0.8	white, 10 day timescale	sinusoidal
$Q_{S,W_{30}}$	0.8	white, 30 day timescale	sinusoidal
$Q_{S,NAO+}$	0.8	constant NAO+ (no noise)	sinusoidal
$Q_{S,NAO-}$	0.8	constant NAO− (no noise)	sinusoidal
$Q_{S,W,NAO+}$	0.8	NAO+ with added noise	sinusoidal
$Q_{S,W,NAO-}$	0.8	NAO− with added noise	sinusoidal

TABLE 3.1: *Table of runs with noisy forcing*

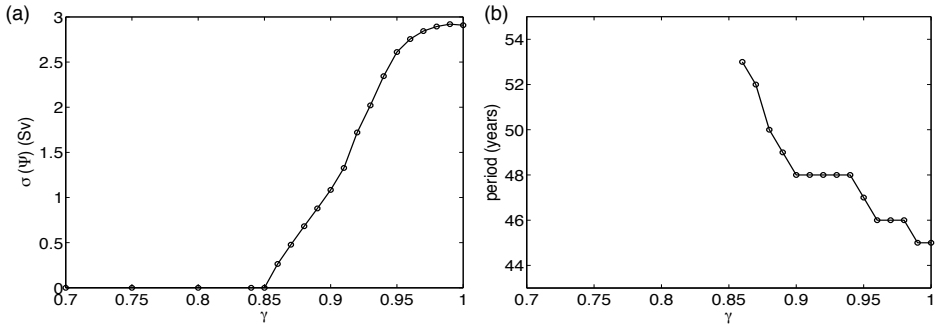

FIGURE 3.2: *(a) Standard deviation (Sv) of the maximum of the meridional overturning streamfunction ($\sigma(\Psi)$) as a function of γ. Below $\gamma = 0.85$ the standard deviation is zero, indicating that there is no oscillatory behavior. (b) Period of oscillation as a function of γ.*

3.3.1 DETERMINISTIC CASE

Under the heat flux (3.2), we compute equilibrium states using time integration starting from the $\gamma = 0$ equilibrium solution (that is, the equilibrium solution under restoring conditions). For each solution obtained, the maximum of the meridional overturning streamfunction is determined and its standard deviation is plotted as a function of γ in figure 3.2(a). For $\gamma \leq 0.85$ there are no oscillations. Near $\gamma = \gamma_c = 0.85$ the system undergoes a Hopf bifurcation and multidecadal oscillations appear. The amplitude of the oscillations is measured by calculating the standard deviation of the meridional overturning rather than the peak to peak amplitude so that comparisons can be made with later simulations where the variability is not regular. The oscillations have periods

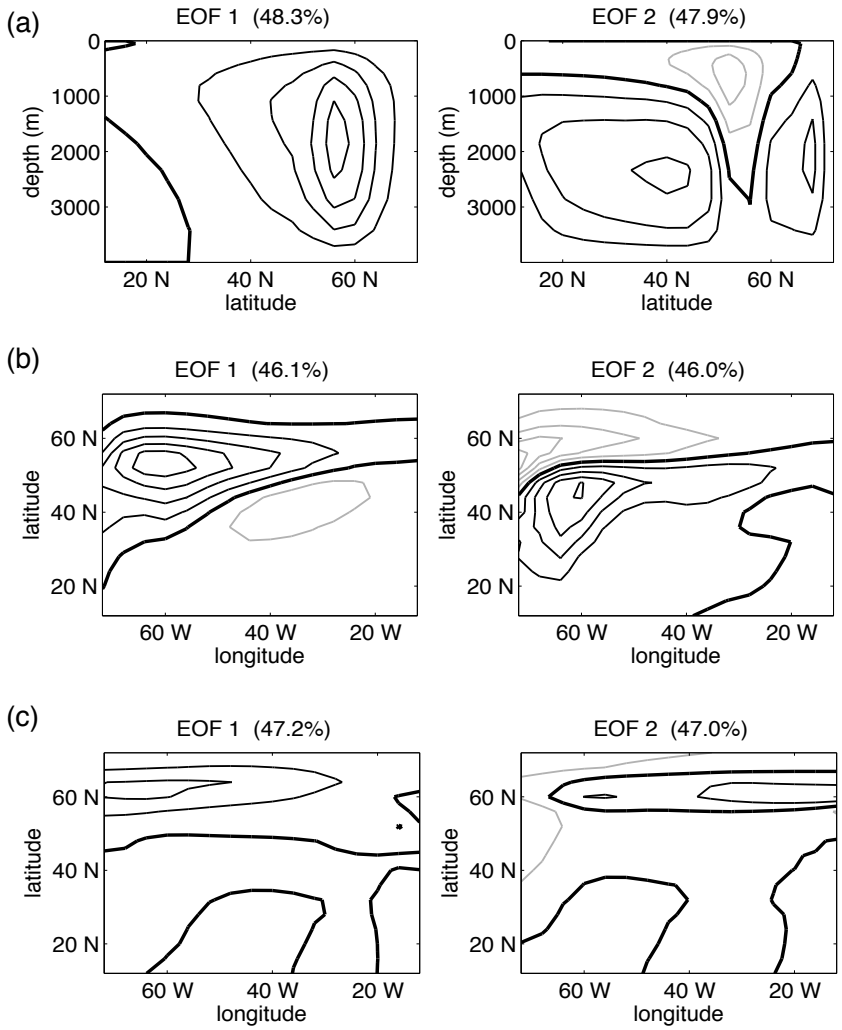

FIGURE 3.3: *First two EOFs of (a) meridional overturning (*96% *of variance, contour interval 0.05 Sv), (b) sea surface temperature (*92% *of variance, contour interval 0.05 K) and (c) temperature in the bottom layer (4000m depth;* 94% *of variance, contour interval 0.1 K) for the deterministic case with* $\gamma = 0.98$*.*

of about 45 to 50 years with the period showing a slight dependence on γ, as seen in figure 3.2(b).

The patterns of the MOC anomalies and the temperature anomalies are very similar to those in te Raa and Dijkstra (2002). For comparison with the noise forcing cases later on, the first two EOFs of each of these fields are shown for $\gamma = 0.98$ in figure 3.3. Figure 3.3(a) shows the first and second EOFs of the MOC. These two EOFs explain 96.2% of the variance, which is concentrated in the northern half of the basin, around the sinking region of the background flow (figure 3.1(a)). These EOFs indicate a strengthening

and weakening of the MOC (EOF 1) as well as a shift in the position of the sinking region (EOF 2) during an oscillation. Also shown are the first and second EOFs of the temperature at the surface (figure 3.3(b)) and in the bottom layer (figure 3.3(c)), which explain 92.1% and 94.1% of the variance, respectively. We can see that the variance in temperature at the sea surface is concentrated in the northwest of the basin, while at depth the temperature mainly varies in a band along the north of the basin. The anomalies at depth move westwards from the eastern boundary and then southwards along the western boundary.

The cycle begins with a positive temperature anomaly in the central western part of the basin. As time progresses the positive anomaly moves northwards and a negative anomaly develops to the south east. The positive anomaly then moves westwards and disappears, while the negative anomaly which has developed to the south intensifies. After half a period of the oscillation, the temperature anomalies have the opposite signs to those seen at the beginning of the cycle. There is a lag of ~ 8 years between the maximum temperature (averaged over the area [46°N – 62°N] $\times$ [74°W – 50°W]) and the MOC, with the MOC leading in agreement with the mechanism described in te Raa and Dijkstra (2002).

3.3.2 WHITE AND SPATIALLY CORRELATED NOISE

We now investigate whether noise forcing from the atmosphere (as represented by noise added to the heat flux) can excite the multidecadal mode in cases when it would normally be damped in the absence of noise, i.e. for $\gamma \leq 0.85$. Several authors have concluded that multidecadal variability in GCMs is forced by atmospheric phenomena (Delworth and Greatbatch, 2000) which involve coherent spatial patterns. The simplicity of the minimal model allows us to systematically explore the effects of spatial and temporal coherence in the noise.

First we consider the effect of spatial coherence in the noise forcing by comparing the responses of the model under the following two heat fluxes:

$$\begin{aligned} Q_W &= (1-\gamma)Q_{rest} + \gamma Q_{pres} + \sigma_n Z_{ij}(t) \\ Q_{S,W} &= (1-\gamma)Q_{rest} + \gamma Q_{pres} \\ &\quad + \sigma_n Z(t) \sin\left(\frac{\pi(i-i_e)}{i_w - i_e}\right) \sin\left(\frac{\pi(j-j_s)}{j_n - j_s}\right) \end{aligned} \tag{3.3}$$

In Q_W, σ_n is the amplitude of the noise and Z_{ij} is a normally distributed random variable which takes on a different value at each grid point (i, j) in space at each timestep t. The noise in Q_W is thus uncorrelated in both space and time. In $Q_{S,W}$, $i_e \leq i \leq i_w$ and $j_s \leq j \leq j_n$ are the grid variables in the x and y directions and $Z(t)$ is a normally distributed random variable. The spatial pattern is chosen as a rough approximation to variations in atmospheric heat fluxes seen over the North Atlantic (Cayan, 1992b,a; Grosfeld et al., 2007). However, the pattern has only spatial correlation and the noise is uncorrelated in time. In both Q_W and $Q_{S,W}$, the amplitude (σ_n) of the noise was taken to be 10% of the difference between the maximum and minimum over the basin of the prescribed heat flux Q_{pres} which results in $\sigma_n \approx 20$ W/m^2. The simulations conducted with different types of noise forcing are listed in table 3.1.

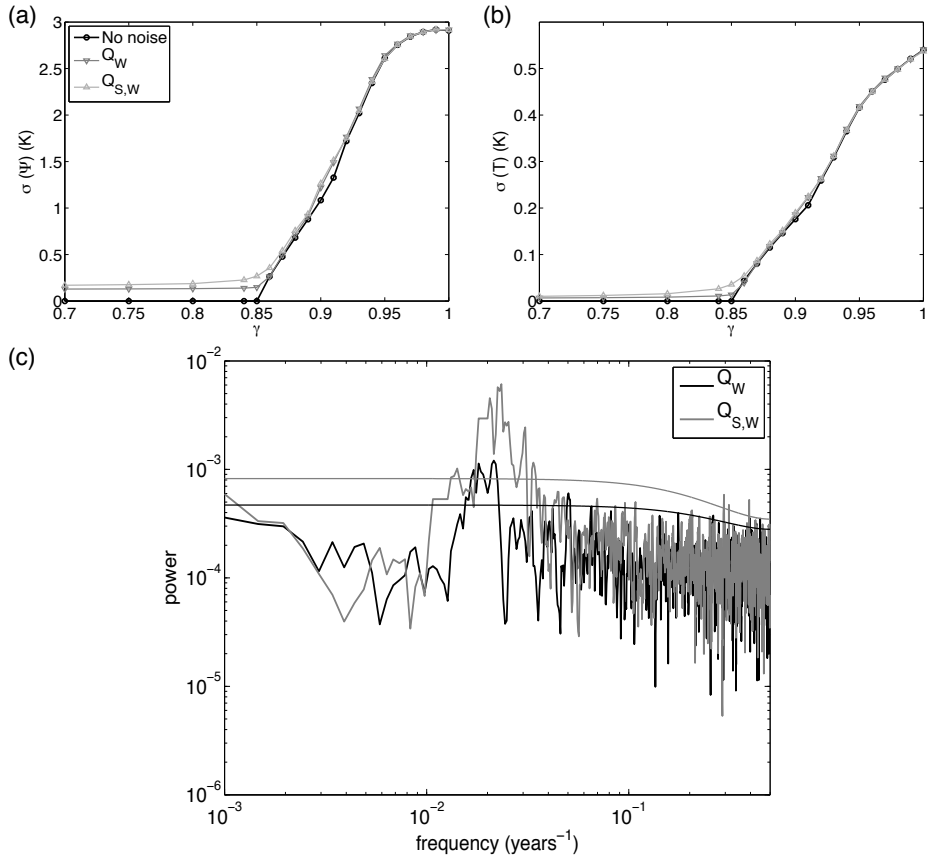

FIGURE 3.4: *Standard deviation of (a) meridional overturning (Ψ, in Sv) and (b) sea surface temperature (in $^\circ$C, averaged over the area [$46^\circ N - 62^\circ N$] $\times$ [$74^\circ W - 50^\circ W$]) as a function of γ, for the no noise, Q_W and $Q_{S,W}$ cases. (c) Spectrum of SST over the area [$46^\circ N - 62^\circ N$] $\times$ [$74^\circ W - 50^\circ W$] for the Q_W (black line) and $Q_{S,W}$ (grey line) cases with $\gamma = 0.8$. The 99% significance levels are also plotted.*

Figures 3.4(a) and 3.4(b) show the effects of noise on the standard deviation of meridional overturning and sea surface temperature. For values of γ greater than the critical value (i.e. past the Hopf bifurcation point) the noise has only a small effect. In contrast, for near and below critical values of γ, the noise causes both the surface temperature and overturning strength to vary, unlike in the deterministic cases. The standard deviation is larger for $Q_{S,W}$ than for Q_W for the same value of γ. This is also seen in figure 3.4(c), which shows the spectra for the case of $\gamma = 0.8$ with the addition of the two different types of noise. Although the noise added to the system has no preferred frequency the spectrum shows a large peak at multidecadal frequencies. This is in contrast to the $\gamma = 0.8$ case in the absence of noise, where neither the temperature or MOC strength vary at all. It can also be clearly seen that spatial correlation of the noise increases the height and breadth of the multidecadal peak.

We find that, in cases with noisy forcing, for values of $\gamma > \gamma_c$, the spatial patterns

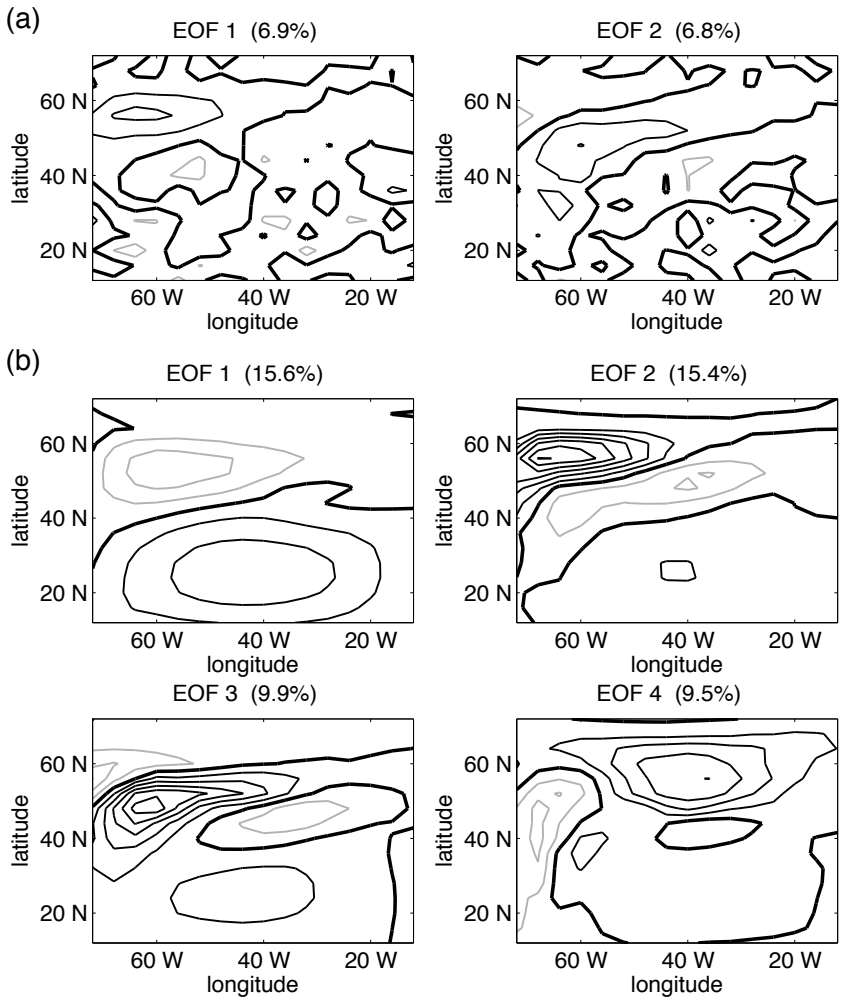

FIGURE 3.5: *(a) First two EOFs of sea surface temperature for the Q_W case, which together explain almost 14% of the variance (contour interval 0.1 K). (b) First four EOFs of sea surface temperature for the $Q_{S,W}$ case, which together explain over 50% of the variance (contour interval 0.05 K). In both cases $\gamma = 0.8$ and the data was low-pass filtered to allow periods of between 30 and 100 years.*

of variability closely resemble those in the no noise case. When γ is decreased below γ_c, noise dominates the patterns seen in the MSSA analysis. However, if the data is low-pass filtered to allow periods from 30 to 100 years then the patterns of multidecadal variability are recovered. Figures 3.5(a) and 3.5(b) show the EOFs for the Q_W and $Q_{S,W}$ cases with $\gamma = 0.8$. In the Q_W case the southern half of the basin is dominated by small-scale variations due to the white noise forcing. In the northern half of the basin there are similar patterns to those seen in the EOFs for the no noise case (figure 3.3(b)). Figure 3.5(b) shows the first four EOFs of SST for the $Q_{S,W}$ case, with the EOFs accounting

for 15.6%, 15.4%, 9.9% and 9.5% of the variance respectively. As in the Q_W case the northern part of the basin is dominated by a pattern similar to that in figure 3.3(b). In the 1st EOF (and to a smaller extent in the 3rd) the southern part of the basin shows a signal from the sinusoidal spatial pattern of the noise forcing. These two cases show that the noise has excited the same multidecadal mode as in the cases with $\gamma > \gamma_c$, a mode which is damped under these boundary conditions in the absence of noise.

In other words, there is a multidecadal mode present in the system with a growth rate that increases with increasing γ. For $\gamma < 0.85$ the growth rate is negative, that is the mode is damped, and the damping of the mode increases as γ decreases. This means that for γ below 0.85 the steady equilibrium state of the system is stable. As we have seen, however, the multidecadal mode can still be excited in the presence of noise. At $\gamma = 0.85$ the growth rate of the multidecadal mode is zero and the system undergoes a Hopf bifurcation. For $\gamma > 0.85$ the growth rate is positive so the steady equilibrium state becomes unstable to the mode and multidecadal oscillations are observed even in the absence of noise.

3.3.3 THE IMPACT OF TEMPORAL COHERENCE IN THE NOISE

While both white noise (Q_W) and noise with spatial coherence ($Q_{S,W}$) have been shown to excite the multidecadal mode for γ less than the critical value, neither can excite it to an amplitude comparable to that seen in observations (c.f. the observed variation in SST of ~ 0.5°C (Delworth et al., 1993) and the values in figure 3.4(b)). Since atmospheric phenomena can persist on timescales much longer than the timestep used in the model we next investigate the effect of temporal coherence in the noise has on the multidecadal variability.

To this end the sinusoidal spatial pattern in (3.3) is multiplied by a monthly white noise index $Z(t)$, so that the noise has a temporal coherence of 30 days; the resulting flux is indicated as $Q_{S,W_{30}}$. This case of noise that has a sinusoidal spatial pattern but is white in time mimics the spatial variations of the NAO but not the temporal variations. Delworth and Greatbatch (2000) found that the low frequency part of the heat flux forcing was most effective at exciting multidecadal variability, so it is interesting to investigate the effect that an NAO with a more realistic temporal signature would have on the model. The monthly NAO index of Luterbacher et al. (2002) is thus also used to force the sinusoidal spatial pattern (with resulting flux $Q_{S,NAO}$). Since the Luterbacher et al. (2002) NAO index has non-zero mean we also force the model using an index of the opposite sign (with resulting flux $Q_{S,rNAO}$). In each case the index is scaled so that it has the same variance as the time series used in the white noise index run.

Figure 3.6(a) compares a timeseries of model SST variability for the $Q_{S,W_{30}}$ case to $Q_{S,NAO}$ and $Q_{S,rNAO}$, which are the two cases involving the NAO index of Luterbacher et al. (2002). The temperatures for the $Q_{S,rNAO}$ case have been reversed so that they can be easily compared to the $Q_{S,NAO}$ case. It is clear from the two NAO index runs that the small offset in the mean of the Luterbacher et al. (2002) NAO index does not greatly effect the resulting temperature variability. The variability in the $Q_{S,W_{30}}$ case has a smaller amplitude than the two NAO index cases which indicates that temporal coherence in the noise is having an effect on the amplitude of the variability.

Next we investigate the effect of the timescale of temporal coherence more systematically. Figure 3.6(b) shows the spectra for cases where white noise with sinusoidal

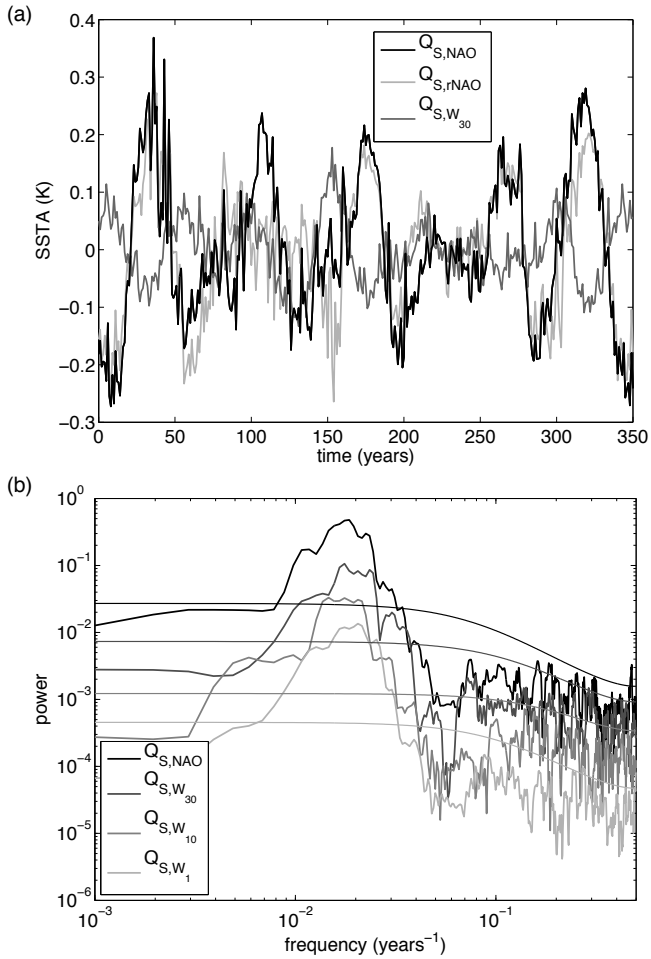

FIGURE 3.6: *(a) Variability in SST for three runs with sinusoidal spatial forcing; $Q_{S,NAO}$ (black line), $Q_{S,rNAO}$ (light grey line) and $Q_{S,W_{30}}$ (dark grey line). The signs of the temperature anomalies in the $Q_{S,rNAO}$ case have been reversed for easier comparison to the $Q_{S,NAO}$ case. (b) Spectra of temperature for four runs with sinusoidal spatial forcing; $Q_{S,NAO}$ (black line) and the other three using white noise with timescales of 1 (Q_{S,W_1}; light line), 10 ($Q_{S,W_{10}}$; medium grey line) and 30 ($Q_{S,W_{30}}$; dark grey line) days. The 99% significance levels for each case are also plotted.*

spatial patterns and timescales of 1, 10 and 30 days (runs Q_{S,W_1}, $Q_{S,W_{10}}$ and $Q_{S,W_{30}}$) is compared to the NAO index case ($Q_{S,NAO}$, which also has a coherence timescale of 30 days). The multidecadal peak increases as the coherence timescale in the noise forcing increases. Forcing using the NAO index also increases the power in the multidecadal peak over that when white noise forcing with the same timescale is used. Since the spectrum of the NAO index shows slightly increased power at low frequencies compared to white noise this result agrees with Delworth and Greatbatch (2000), who found that

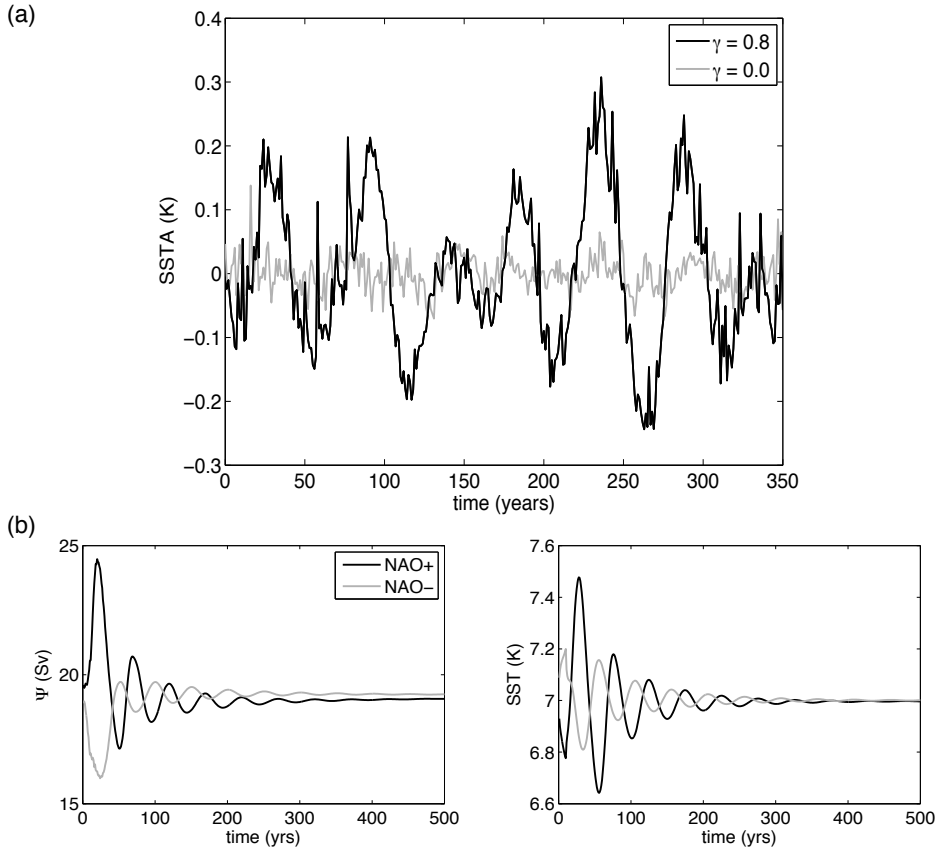

FIGURE 3.7: *(a) The effect of γ on the amplitude of temperature variations. The temperature anomaly for two runs of the $Q_{S,NAO}$ case with values of γ equal to 0.8 (black line) and 0.0 (grey line). (b) Meridional overturning strength (left) and surface temperature (right) for a run where the flux pattern of the NAO+ state ($Q_{S,NAO+}$) was held constant for ten years and then switched off (black lines). Similarly for the NAO− state ($Q_{S,NAO-}$; grey lines).*

multidecadal variability in their coupled climate model was driven by the low-frequency variations in heat flux. Note, however, that the timescale of coherence here is at most 30 days, whereas Delworth and Greatbatch (2000) used a 20 year filter to separate high and low frequency atmospheric forcing. When spatial coherence is removed (so that the noise added to each grid point is independent) the temporal coherence still causes large variations in temperature but the power at multidecadal frequencies is greatly reduced (not shown), which indicates that the spatial coherence is necessary to effectively excite the mode.

To demonstrate that the variability is indeed caused by the excitation of the multidecadal mode and not by direct forcing of the low-frequency component of the NAO index, we compare the cases of NAO index forcing ($Q_{S,NAO}$) for two values of γ. Figure 3.7(a) shows the variations in temperature seen for the cases with $\gamma = 0.8$ and $\gamma = 0.0$

(pure restoring conditions). The spectrum of the $\gamma = 0.0$ case (not shown) does have a small peak at multidecadal frequencies, but it is dwarfed by the variability seen in the higher γ case. This illustrates that the further from the Hopf bifurcation point the system is (in the stable regime), the smaller the variability excited by forcing of a particular strength, i.e. the external forcing is unable to generate multidecadal variability in the presence a strongly damped (or absence of) the multidecadal mode.

Next we perform two additional tests to study the decay of the multidecadal mode through the relaxation of the system back to a steady state after forcing (which excites the multidecadal mode) has been removed. The surface flux pattern associated with the NAO+ state ($Q_{S,NAO+}$; flux positive in the southern half of the basin and negative in the north) was applied to the ocean model in equilibrium (with $\gamma = 0.8$) for a duration of ten years, and then removed so that the model could relax back to equilibrium. A similar test was carried out with the flux pattern of the NAO− state ($Q_{S,NAO-}$; flux negative in the southern half of the basin and positive in the north). The overturning strength and surface temperature are plotted in figure 3.7(b). After the additional forcing is removed the ocean undergoes a series of oscillations with a multidecadal period, with the oscillations decaying as the system relaxes back to its equilibrium state.

3.3.4 MECHANISM OF EXCITATION

The results in the previous sections show that a multidecadal mode which destabilises the background state for values of $\gamma > \gamma_c$ can also be excited under conditions where $\gamma < \gamma_c$ by noisy forcing. To identify the mechanism of this excitation we take a look at background states. Noise can rectify the background state and the background state has an effect on the stability of the multidecadal mode. Thus the effect of the background state on the stability of the multidecadal mode is investigated. Figure 3.8(a) shows the MOC of the background state with steady forcing (i.e. no noise) with $\gamma = 0.8$. In one simulation, the model is then forced with the (steady) surface heat flux pattern associated with a permanent NAO+ state until a steady state is reached. Figure 3.8(b) shows the difference between the MOC of this new time-mean state and the steady state under standard no noise forcing. In another simulation, this is repeated for a steady permanent NAO− forcing and the difference between this time-mean state and the standard no noise case is shown in figure 3.8(c).

The pattern of permanent NAO+ forcing has positive heat flux over the southern half of the basin and negative heat flux over the northern half, and thus acts to increase the north-south surface temperature gradient. This leads to an increase in the MOC as well as a slight northward shift of the sinking region, as seen in figure 3.8(b). The opposite occurs with permanent NAO− forcing, with a decrease in the north-south temperature gradient leading to a decrease in MOC (figure 3.8(c)). According to Dijkstra (2006) the growth rate of the multidecadal mode increases with increasing strength of the MOC, which in turn increases with increasing ΔT, where ΔT is the north-south temperature difference. This means that the permanent NAO+ and NAO− forcing has alternately increased and decreased the growth factor of the multidecadal mode, i.e. under permanent NAO+ forcing the mean meridional overturning circulation is more unstable to the multidecadal mode than the mean meridional overturning circulation under permanent NAO− forcing. This difference in stability of the background states can also be seen in

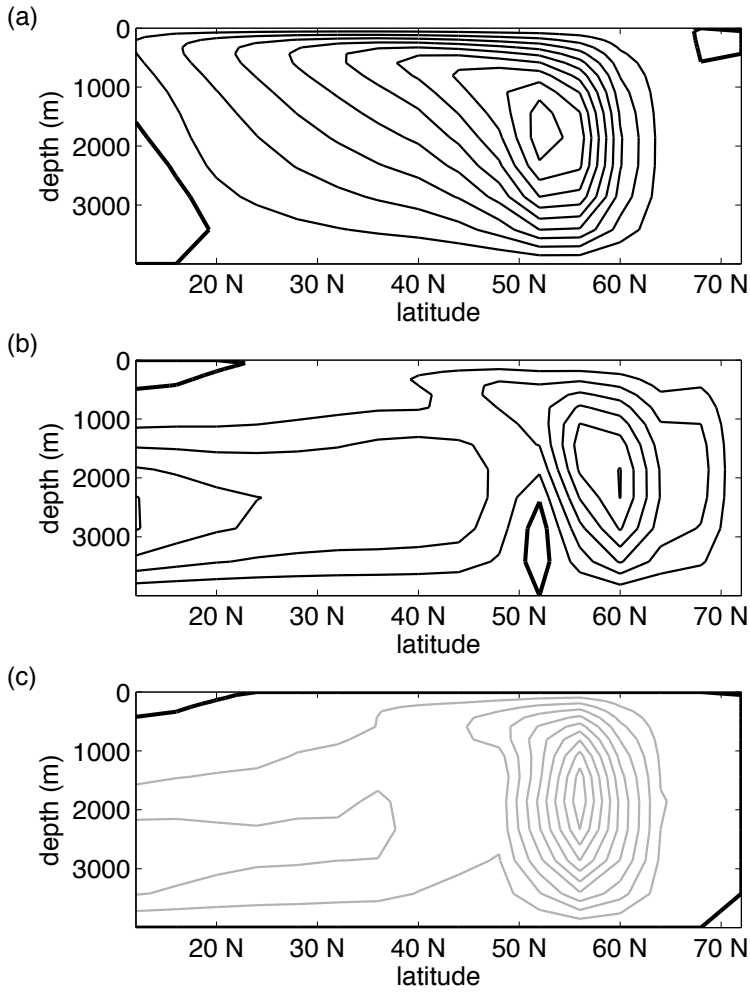

FIGURE 3.8: *(a) Meridional overturning streamfunction of the steady state under steady (no noise) forcing with $\gamma = 0.8$. Contour interval is 2 Sv, zero contour is bold. (b) Difference between the meridional overturning of the steady state reached under permanent NAO+ forcing and the steady state shown in (a). Contour interval is 0.5 Sv. (c) Same as (b) but for NAO− forcing. Negative contours are in grey.*

figure 3.7(b), where the amplitude of the oscillations is larger when relaxing back to the equilibrium state from permanent NAO+ forcing than from permanent NAO− forcing.

This difference in stability under NAO± forcing can be most clearly illustrated by superimposing spatially coherent, temporally white noise on the two equilibrium states reached under steady NAO+ or NAO− forcing (runs $Q_{S,W,NAO+}$ and $Q_{S,W,NAO-}$). Figure 3.9(a) shows SST anomalies (relative to their respective equilibrium states) for the two cases. The same type of forcing is used in each case, yet the amplitude of variability excited in the NAO+ case is larger. This is also seen in the spectra of the two

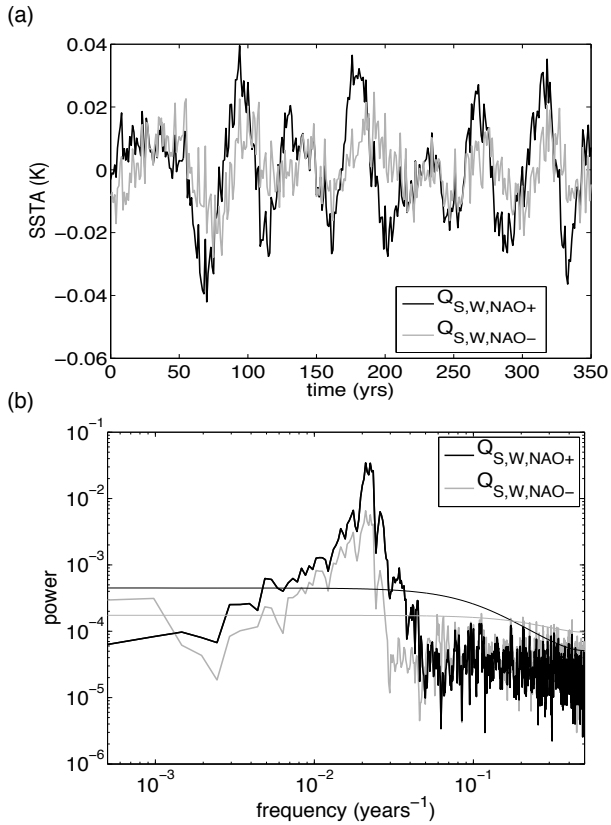

FIGURE 3.9: *(a) SST anomalies from two runs, $Q_{S,W,NAO+}$ (black line) and $Q_{S,W,NAO-}$ (grey line), where spatially coherent, temporally white noise is added to the equilibrium states reached under steady NAO+ or NAO− forcing. (b) Spectra of the two runs as in (a). 99% significance levels are also plotted.*

cases in figure 3.9(b), where the larger peak at multidecadal frequencies in the NAO+ case shows that the mean state under permanent NAO+ conditions is more unstable to the multidecadal mode than the mean state under permanent NAO− conditions.

3.4 DISCUSSION AND CONCLUSIONS

A systematic study was performed on the noise induced variability in the North Atlantic using an idealised, so-called minimal, model. The effect of atmospheric damping was considered by introducing a parameter γ in the heat flux, such that at $\gamma = 1$ there are sustained oscillations while at $\gamma = 0$, there is no oscillatory behavior. The use of the minimal model with simple boundary conditions allowed us to perform calculations for a range of γ values rather than being restricted to the value inherent to one particular model. This means that we can follow the mode and study the effect of the noise as the growth rate changes. In the deterministic case, the transition value between no os-

cillations and sustained oscillations is found near a critical value $\gamma_c = 0.85$. From a mathematical point of view we know that the system undergoes a Hopf bifurcation at this critical value of γ. In our case we have used γ as the control parameter, but the critical value also depends on other model variables. In te Raa and Dijkstra (2002), for example, both horizontal diffusivity K_H and vertical diffusivity K_V were used as control parameters.

With the addition of noise a so-called Stochastic Hopf bifurcation occurs. In this case, oscillatory variability with an amplitude depending on the noise arises for values of $\gamma \leq \gamma_c$ while for $\gamma > \gamma_c$ the variability does not differ much from the deterministic case. For $\gamma \leq \gamma_c$ oscillations are damped in the deterministic case and, in the absence of further excitation, decay back to the stable steady state. The presence of noisy forcing continuously excites the variability, and a spectrum shows that the variability has the same multidecadal period as in the cases where γ is greater than the critical value, while EOFs confirm that the same spatial pattern of the variability also reappears. This clearly shows that for $\gamma < \gamma_c$ the noise excites the normal multidecadal mode which in the deterministic case obtains a positive growth factor only for $\gamma > \gamma_c$.

When the minimal model is run at a small value of γ such that the background state is very stable, each of the noise forcing is only able to cause very small variability (not shown). Hence, the presence of the AMO mode and the occurrence of the Hopf bifurcation certainly play a central role in the amplitude of the multidecadal variability. Other possible mechanisms such as a passive response of the ocean on the atmospheric noise (Hasselmann, 1976) or the extension by Saravanan and McWilliams (1998), where the effect of horizontal advection leads to a preferred time scale, are therefore less likely. It is also interesting that in the noise-forced cases one sees normal mode patterns in the variability, instead of non-normal mode patterns (Farrell and Ioannou, 1996). It is likely that the time scale on which non-normal modes grow is much faster than the typical time scale of the variability. Without knowing the non-normal modes for the minimal primitive equations model, it is difficult to assess their role in the multidecadal variability.

It was demonstrated that both spatial and temporal coherence in the random part of the heat flux forcing are important to excite the multidecadal variability to reasonable amplitude. The spatial coherence is important as it modifies the surface heat flux so as to cool the northern part of the basin and warm the southern part, or vice versa. For temporally uncorrelated white noise, these two situations have the same probability and the background state is only slightly rectified, which can only slightly alter the effective growth factor of the multidecadal mode. When temporal coherence is introduced, by using the NAO index for example, the noisy heat flux directly influences the background state and hence a relatively large modification of the growth factor can occur.

These results are for the minimal model, but how about more realistic models, i.e. extensions of the minimal model? Until now, only the AMO mode and the periodic oscillations under prescribed flux conditions have been studied in extensions of the minimal model. While continental shape is irrelevant for ENSO, the shape of the continents is essential for the deformation of the AMO mode into a pattern which resembles patterns obtained in coupled climate models (Delworth and Greatbatch, 2000) and observations (Dijkstra et al., 2006). Results in idealised models with two basins showed that the AMO mode is localised in the sinking regions of the global thermohaline flow (von der Heydt

and Dijkstra, 2007). This indicates that the AMO mode is unique to the North Atlantic.

Together with results in previous papers where the effects of salinity, wind, continental geometry, bottom topography (te Raa and Dijkstra, 2003; te Raa et al., 2004), cross-equatorial flow and interbasin exchange (von der Heydt and Dijkstra, 2007; Dijkstra and von der Heydt, 2007) were considered, we have now, with the effect of noise presented here, considered all relevant extensions of the minimal model. With this framework, we can try to interpret results of CGCM studies on this topic in particular those by Delworth and Greatbatch (2000). Their CLIM simulation (the ocean model forced with only climatological atmospheric fluxes) nicely demonstrates that the flow regime is not supercritical, i.e., there is no sustained variability and the multidecadal mode is damped. The TOTAL (ocean forced by total fluxes of the coupled model run) and RANDOM (ocean forced by only the annual-mean atmospheric fluxes chosen at random) simulations demonstrate that coupled feedbacks and atmospheric noise on time scales < 1 year are not central to the generation of multidecadal variability. As the multidecadal variability has a much smaller amplitude under HEAT_HP (only low-frequency part < 20 year) than under HEAT_LP (only low-frequency part > 20 year) forcing, it appears that the low-frequency component of the atmospheric variability is driving the multidecadal variability as is indeed the interpretation in Delworth and Greatbatch (2000). However, as we have shown here, it is both the spatial and temporal correlations in the noise which are important for the excitation of the multidecadal mode, with the amplitude of the mode increasing with increasing temporal correlation.

Although both Delworth and Greatbatch (2000) and our study find that low frequency variability excites the mode, there is a striking difference in the timescales involved. Delworth and Greatbatch (2000) found that atmospheric variability on timescales less that a year were not necessary to excite the mode, whereas here we find that the variability can be excited to an appreciable amplitude using noise forcing with a temporal coherence on the timescale of days. This is related to the relative stabilities of the modes in the two models. The mode in the model of Delworth and Greatbatch (2000) may have a lower growth rate than the mode in our simple model (topography, for example, is observed to stabilise the mode (te Raa et al., 2004)), which is equivalent to the Delworth and Greatbatch (2000) mode having a value of γ further away from the bifurcation point. Increasing levels of noise (and coherence in the noise) are then necessary to excite the variability.

In conclusion, according to our results, multidecadal variability in the North Atlantic is not directly driven by the low-frequency atmospheric variability (in particular the NAO). Instead the variability results from the excitation of a multidecadal internal ocean mode through atmospheric noise. This noisy forcing rectifies the background state which affects the growth rate of the underlying multidecadal mode and hence determines the amplitude of the resulting multidecadal variability.

4

SUB-SURFACE SIGNATURES OF THE ATLANTIC MULTIDECADAL OSCILLATION

Sub-surface signatures of the Atlantic Multidecadal Oscillation (AMO) are identified using expendable bathythermograph (XBT) measurements of temperature from the surface down to a depth of 400 m. Basin averaged temperature anomalies in the North Atlantic at different depths display multidecadal variability with a phase shift between temperature anomalies at the surface and at depth. Westward propagation of temperature anomalies is observable at depth and there is a lag correlation between east-west and north-south temperature gradients, with the east-west temperature gradient leading. These sub-surface characteristics of the AMO agree with those expected from the noise-driven internal ocean mode view of the AMO, as derived from a hierarchy of ocean-atmosphere models.

This chapter is based on:
Sub-surface signatures of the Atlantic Multidecadal Oscillation, by L. M. Frankcombe, H. A. Dijkstra and A. S. von der Heydt, *Geophysical Research Letters*, **35**, L19602, 2008.

4.1 INTRODUCTION

It is now well established that North Atlantic sea surface temperature (SST) displays variability on multidecadal time scales (Kushnir, 1994; Enfield et al., 2001), a phenomenon usually referred to as the Atlantic Multidecadal Oscillation (AMO) (Kerr, 2000). An AMO index, defined by Enfield et al. (2001) as a ten year running mean of SST anomalies averaged over the Atlantic basin north of the equator, shows that North Atlantic SSTs were cooler than average in the periods 1900–1920 and 1970–1990 with an intervening warmer period during 1940–1960.

Multidecadal to centennial SST variability has been simulated in various coupled general circulation models (Delworth et al., 1993; Vellinga and Wu, 2004; Dong and Sutton, 2005; Jungclaus et al., 2005) and several different mechanisms have been proposed. While there is a general consensus that the Atlantic Meridional Overturning Circulation (MOC) is involved, some researchers attribute a central role to the tropics (Vellinga and Wu, 2004; Knight et al., 2005), some stress the importance of the Arctic ocean (Jungclaus et al., 2005), while others find that only North Atlantic processes are essential (Delworth et al., 1993; Dong and Sutton, 2005).

Another approach to understanding AMO variability uses a hierarchy of ocean and coupled ocean-atmosphere models and follows the characteristics of the multidecadal variability through this model hierarchy (Huck et al., 1999; te Raa and Dijkstra, 2002, chapter 2). Uncoupled ocean models provide a detailed picture of how multidecadal variability arises from the geostrophic and hydrostatic response to westward propagating temperature (or density) anomalies, with an out of phase response of the MOC and the zonal overturning (te Raa and Dijkstra, 2002). More sophisticated models have clarified the role of the atmosphere: low-frequency components of atmospheric variability are important to excite the multidecadal variability in the ocean (Delworth and Greatbatch, 2000, chapter 3 of this thesis).

The noise-driven internal mode view of the AMO which arises from the minimal modelling approach has two central elements: the westward propagation of temperature anomalies and a phase difference between east-west and north-south temperature differences. The westward propagation is associated with so-called thermal Rossby modes and hence is affected by the background time mean ocean state. Ocean-only models show that the propagation is clearest below the ocean surface because of the smaller background zonal velocities and the decreased influence of noisy surface forcing. While the characteristics of the AMO in terms of SST variability are more or less well established, basin wide variability in sub-surface layers has not been investigated due to the scarcity of data and the short length of the available timeseries compared to the estimated period of the variability. Motivated by this minimal model view of the AMO we investigate westward propagation and lateral temperature differences in the sub-surface North Atlantic using XBT data.

The present study uses ocean temperatures from the Joint Environment Data Analysis (JEDA) Center (http://jedac.ucsd.edu/index.html). This data set consists of monthly mean ocean temperatures from January 1955 to December 2003 (588 months) in 11 layers between the sea surface and 400 m depth. The data is interpolated on to a 5° longitude by 2° latitude grid between 60°N and 60°S. Anomalies are calculated with respect to the time mean over the whole time period. No trends have been removed due to the difficulty of separating the anthropogenic warming trend from natural variability.

4.2 SUB-SURFACE AMO INDICES

Following Enfield et al. (2001) we define subsurface AMO indices as the ten year running mean of North Atlantic temperature anomalies in each layer over the region 0 – 60°N, 85°W – 5°E. The results are shown in figure 4.1(a). It is apparent that there is a phase shift between the surface and the lower layers, particularly in the earlier part of the record. While the basin-averaged SST was cooling over the period 1960–1972 for example, by 1967 the temperature at 400 m was already increasing. After 1990 the sub-surface and surface signal are more in phase, consistent with the warming trend in the upper-ocean heat content (Levitus et al., 2000) attributed to anthropogenic climate change.

We examine the sub-surface spatial pattern of the AMO by dividing the basin into nine sub-regions (north west, central north, north east, central west, center, etc.) and calculating temperature anomalies at each level within each region. The results are shown in figure 4.1(b). The largest temperature anomalies are seen in the north-west of the basin. The anomalies in the west, particularly the central- and north-western regions, are more uniform with depth while the phase difference between different layers seen in the overall AMO index (figure 4.1(a)) is more apparent in the central and eastern parts of the basin.

Another interesting feature which can be seen in figure 4.1(b) is the warming after 1990. In the north of the basin the warming starts in all layers at the same time while in the south there is a delay between the onset of warming in the upper and lower layers. It is very likely that this is related to the presence of the sinking region in the north of the basin (Levitus et al., 2000).

4.3 SUB-SURFACE PROPAGATION CHARACTERISTICS

Following Kushnir (1994) we calculate the difference between two warm and two cool periods to illustrate the patterns of warming and cooling of the upper and lower layers at different times. First we use the periods 1970–1972 (upper layers anomalously cool) and 1959–1961 (upper layers anomalously warm). Figure 4.2 shows the spatial pattern of the difference between these two periods at two different depths, the upper (0–80 m, figure 4.2(a)) and lower (300–400 m, figure 4.2(b)) layers.

In figure 4.2(a) the temperature anomalies are positive over most of the basin, with a particularly strong anomaly in the east. A strong negative anomaly, the remains of the previous cool phase, appears in the north west. This cool anomaly can also be seen at depth in figure 4.2(b) where much of the basin is covered by negative temperature anomalies. This is consistent with the idea that temperature anomalies are more uniform with depth in the western part of the basin.

Similar figures are shown using the periods 1986–1988 (lower layers anomalously cool) and 1975–1977 (lower layers anomalously warm; figures 4.2(c) and (d)). These patterns are almost the opposite of those in figures 4.2(a) and (b). At the surface a warm anomaly covers most of the north while a cold anomaly is just beginning to develop in the south. In the deeper layers a warm anomaly covers most of the basin. The intense warm anomaly seen at the surface in the north west is also apparent at depth.

Basin-wide westward propagation of temperature anomalies is an important feature

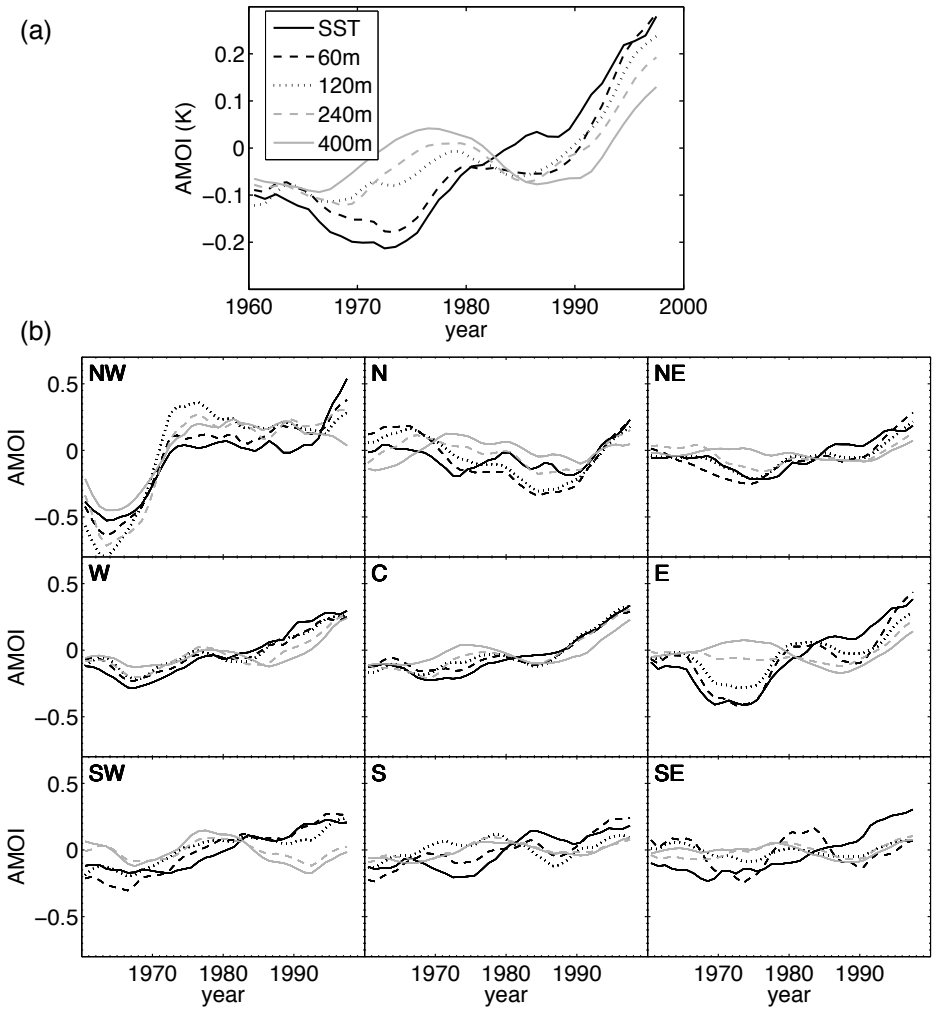

FIGURE 4.1: *(a) Temperature anomalies at different levels averaged over the North Atlantic basin with a ten year running mean. The solid black line shows the basin averaged temperature over all layers from the surface to 400 m. Note that no trends have been removed from this data. (b) Similar indices calculated over sub-regions within the North Atlantic. Line styles are as in a and the regions are the north-west (NW; top left), central north (N; top centre), north-east (NE; top right) and so on.*

of the AMO as found in simpler models (te Raa and Dijkstra, 2002). A Hovmöller diagram of temperature anomalies averaged over 10°–60°N at a depth of 300–400 m is shown in figure 4.3(a). Since the anomalies are advected northwards by the mean circulation as they travel west across the basin it is necessary to average over a range of latitudes to see the full propagation. Averaging over the entire basin highlights the basin-wide nature of the phenomenon. A cold (warm) anomaly in the eastern part of the basin after 1960 (1970) travelled westwards, reaching the western part of the basin after

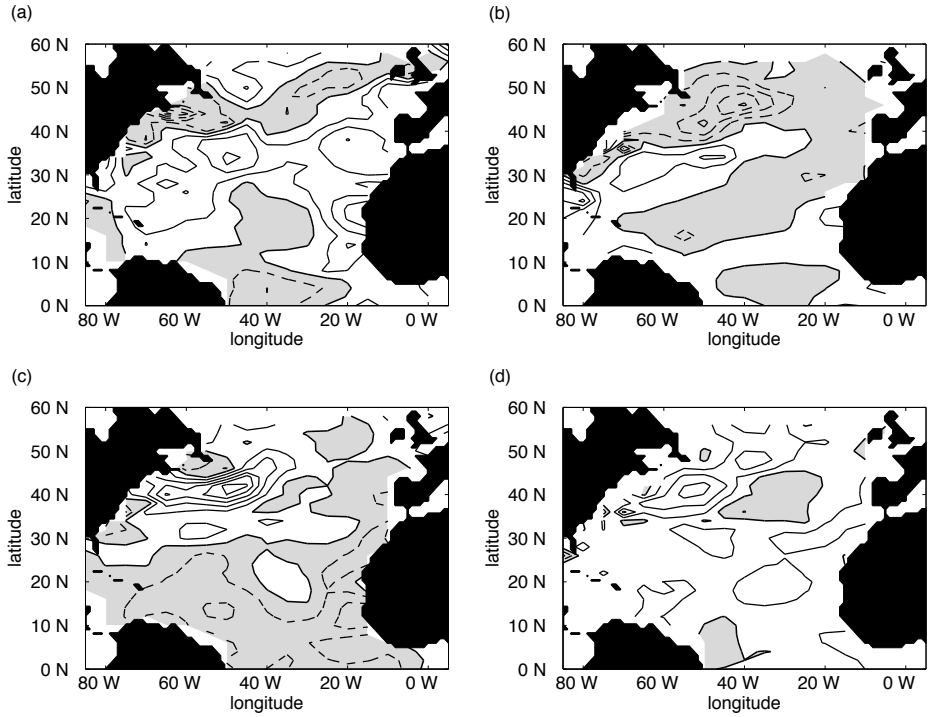

FIGURE 4.2: *Surface and sub-surface patterns. The temperature during the period 1970–1972 (cool in upper layers) has been subtracted from the temperature during the period 1959–1961 (warm in upper layers) for two different depths, (a) the upper (0–80 m) and (b) lower (300–400 m) layers. (c) and (d) as for a and b but for the period 1986–1988 (cool in lower layers) subtracted from the period 1975–1977 (warm in lower layers). Contour interval is 0.3°C, negative contours are dashed.*

1970 (1980). A second cold anomaly developed in the east after 1980, however by this time the warming trend begins to dominate the signal and propagation is less clear. The westward propagation is most clearly seen at a depth of 300–400 m, the lowest levels included in the data set. It is also most clearly seen in boreal summer (JJA), when the shallower mixed layer keeps noise confined to the surface, and between the latitudes 20° - 30°N (south of the Gulf Stream; not shown). Eastward propagation of anomalies is observed in the upper layers at the latitude of the Gulf Stream, in agreement with Hansen and Bezdek (1996) and Sutton and Allen (1997).

A Hovmöller plot of heat content from the surface to a depth of 400 m is shown in figure 4.3(b). The timing of the warm and cool anomalies agrees with the temperature anomalies although westward propagation is not seen in the heat content due to the strong eastward flow of the Gulf Stream and North Atlantic Drift at the surface. If the averaging is restricted to 10°–30°N then westward propagation becomes visible at the beginning of the record (not shown). Figure 4.3(b) can be used to interpret the pattern of heat storage found by Levitus et al. (2000) between the period 1970–1974 and 1988–1992 (their figure 3a). The change in heat content during this time can be largely

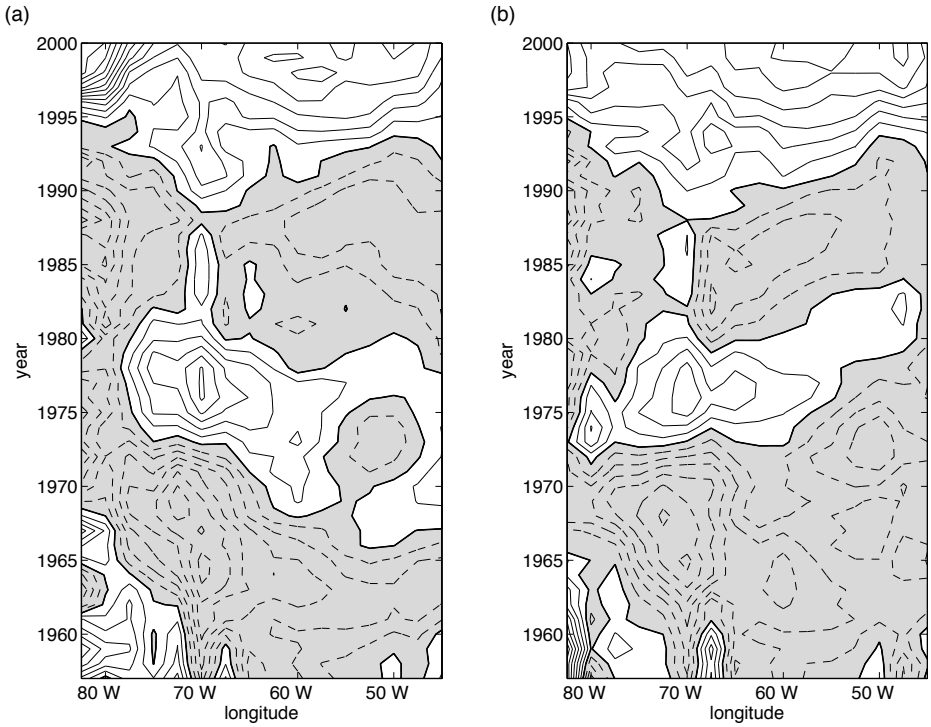

FIGURE 4.3: *Hovmöller plot averaged over 10° - 60°N across the North Atlantic of (a) temperature anomalies at a depth of 300–400 m and (b) heat content from the surface to 400 m. Five year running means have been applied. Contour interval is 0.05°C or 1×10^8 Ws/m^2. Negative contours are dashed.*

attributed to the AMO (although it also includes the signal of anthropogenic warming) and the pattern of the anomalies is related to the temperature anomalies in figure 4.2.

Another feature of the AMO central to the noise driven internal mode view is a phase difference between the zonally averaged north-south surface temperature difference T_{N-S} and the meridionally averaged east-west surface temperature difference T_{E-W}, with T_{E-W} leading by about a quarter of a period (te Raa and Dijkstra, 2002). Temperature anomalies in the east, west, north and south of the basin were calculated using the masks shown in figure 4.4(a). The lag correlation of five year running means of T_{N-S} and T_{E-W} is plotted in figure 4.4(b) for temperatures measured at the surface (black) and averaged from the surface to a depth of 400 m (grey). Significant correlations occur when T_{E-W} leads T_{N-S}, with a peak around 8 years at the surface and around 5 years for the depth averaged temperatures. The positive correlation at positive lag in figure 4.4(b) agrees qualitatively with the propagation mechanism suggested in te Raa and Dijkstra (2002) which, given the quarter period lead in this mechanism, would suggest a period of 20 to 32 years. This agrees with the number of anomalies seen in figure 4.3 and is also consistent with the results of a number of GCMs (Dong and Sutton, 2005, for example).

On the other hand, AMO indices calculated from longer observational timeseries of

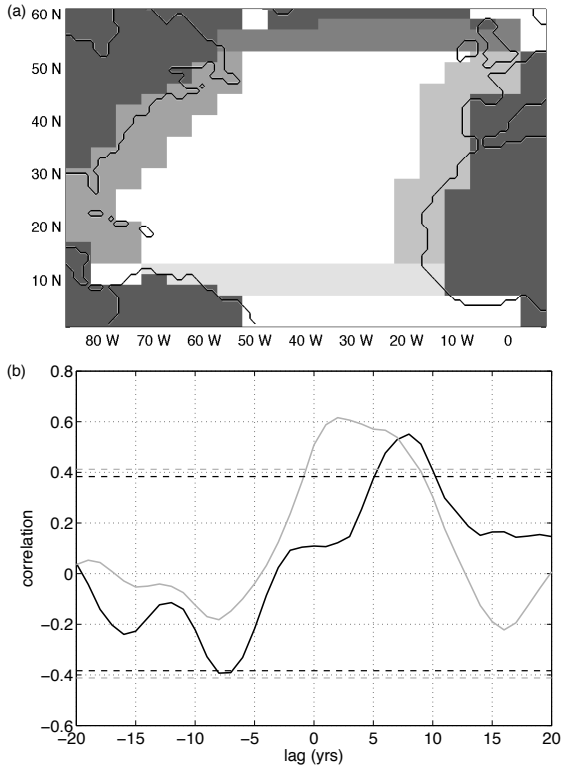

FIGURE 4.4: *(a) The masks used to calculate the east-west and north-south temperature differences. Dark grey indicates land or areas with no data and the masks used, in order of increasing lightness, are T_N, T_W, T_E and T_S. (b) Lag correlation between T_{N-S} and T_{E-W} at the surface (black) and averaged from the surface to 400 m (grey), with positive lags indicating that T_{E-W} leads. Dashed lines are 95% significance levels.*

SST (Delworth and Mann, 2000; Enfield et al., 2001) estimate a considerably longer period of 50-70 years. Hence modulation of longer time scale SST variability is likely to be involved. The short length of the timeseries used here does not allow us to calculate periods with any certainty.

4.4 DISCUSSION

We have investigated long-term variability in XBT data down to 400 m for the North Atlantic over the period 1955–2003. Although there may be a positive temperature bias of the XBT data with respect to CTD data (Gouretski and Koltermann, 2007), this should not affect the phase difference between the surface and sub-surface temperature as found here over the period 1960-1990. After 1990 the temperature signal of the upper 400 m is in phase and is most likely the global warming signal as determined from heat content studies (Levitus et al., 2000, etc.).

As expected from the mechanism of the AMO found in ocean-only models (as described in section 2.3.1), we find westward propagation of sub-surface temperature anomalies and a phase difference between north-south and east-west temperature differences. This mechanism can be used to explain several features of the data. Anomalies develop at the surface close to the eastern boundary of the basin (as seen in figures 4.2(a) and (c)) and travel north-westwards across the basin. At the western boundary the temperature anomalies extend to their greatest depth. Figures 4.2(b) and (d) indeed have their largest anomalies in this part of the basin. This is supported by Figure 4.1(b) showing that in the western part of the basin the phase difference between surface and depth is small and in the north west the anomalies become uniform with depth. This is most likely related to the poleward deepening of the mixed layer. The phase difference between surface and depth was also observed by Molinari et al. (1997) in XBT data in the midlatitude western North Atlantic.

The westward propagation also becomes clear by comparing the AMO index in the north west of the basin (top left box in figure 4.1(b)) to the AMO index over the whole basin (figure 4.1(a)): In the early 1960s, while SSTs over the basin as a whole were cooling, temperatures in the north west were just beginning to warm. This is due to the temperature anomaly from the previous phase of the oscillation remaining in the northern part of the basin while the next temperature anomaly is spreading (center right in figure 4.1(b)). The newly developing warm anomaly (figure 4.2(b)) is appearing at depth while the previous cool anomaly is advected to the north.

As with most studies of multidecadal variability, the data record is too short to be able to make a strong statement on the periodicity of the AMO. The main point here is that the sub-surface phase lag, westward propagation and the lag between meridional and zonal temperature gradients that are predicted by the noise-driven internal ocean mode hypothesis (as described in chapter 2) as signatures of the AMO are all seen in the XBT data.

ACKNOWLEDGEMENTS

We thank Molly Baringer (NOAA, Miami) and Amy Clement (RSMAS, Miami) for suggesting an analysis of the XBT data.

5

Coherent multidecadal variability in North Atlantic sea level

Tide gauge records from around the North Atlantic are examined and found to show variability on 20-30 year time scales. Sea surface height variability along the western boundary of the North Atlantic shows a particularly strong and coherent signal. Similar variability is also found in an ensemble of runs using a state-of-the-art climate model (GFDL CM2.1). This sea surface height variability is linked to variability of temperatures in the upper layers of the ocean and thence to the Atlantic Multidecadal Oscillation. The variability is consistent with the excited internal ocean mode mechanism of multidecadal variability derived from idealised models and the timescale is consistent with that derived from observations of sub-surface temperature variability.

This chapter is based on:
Coherent multidecadal variability in North Atlantic sea level, by L. M. Frankcombe and H. A. Dijkstra, *Geophysical Research Letters*, **36**, L15604, 2009.

5.1 INTRODUCTION

Investigations of multidecadal climate variability in the North Atlantic were originally based on a spatial sea surface temperature (SST) pattern which varies on a time scale of 50-70 years (Schlesinger and Ramankutty, 1994; Kushnir, 1994). Since then global signatures of the so-called 'Atlantic Multidecadal Oscillation' (AMO) have been determined (Enfield et al., 2001; Sutton and Hodson, 2005). General Circulation Model (GCM) studies have suggested a range of mechanisms for the phenomenon (Delworth et al., 1993; Timmermann et al., 1998; Vellinga and Wu, 2004; Dong and Sutton, 2005; Jungclaus et al., 2005; Knight et al., 2005). An important element common to all these mechanisms is a link between the AMO and the strength of the Atlantic meridional overturning circulation (MOC). This relationship is also behind the internal ocean mode mechanism for the AMO found in idealised ocean models (te Raa and Dijkstra, 2002).

An important element common to many of the mechanisms described in GCM studies of the AMO is a link between the AMO and the strength of the Atlantic meridional overturning circulation (MOC). This relationship is also behind the internal ocean mode mechanism for the AMO found in idealised ocean models (te Raa and Dijkstra, 2002). The time scale of the variability however, remains to be satisfactorily explained. Enfield and Cid-Serrano (2006) found that the long period of the AMOI in the observational record is anomalous compared to a proxy reconstruction. In addition, in many GCMs the dominant variability in the North Atlantic has a time scale closer to 20-30 years (Timmermann et al., 1998; Cheng et al., 2004; Dong and Sutton, 2005) rather than 50-70 years. Jungclaus et al. (2005) and Vellinga and Wu (2004), on the other hand, found Atlantic variability on time scales of 70 to 100 years, respectively. These different results, combined with the limited number of observations, have led to some confusion about the characterisation of the AMO.

Variability on 20-30 year time scales was has been found in sub-surface temperature observations in the North Atlantic (chapter 4). This, in addition to the GCM results, indicates that multidecadal variability in the North Atlantic may not be limited to the 50-70 year time scale.

Variability in decadal rates of sea level change was observed by Holgate (2007), while Zhang (2008) showed that sea surface height (SSH) in the North Atlantic is highly correlated with upper ocean temperature. Yan et al. (2004) analysed SSH variations in northwest Europe and suggested that SSH changes are related to changes in heat content and heat fluxes. In light of the inter- to multidecadal variability observed in upper ocean temperatures (Molinari et al., 1997, chapter 4 of this thesis) it is interesting to analyse long SSH records for similar signals. Tide gauge data have been used to study SSH variability over a range of temporal and spatial scales, from local interannual variability to global mean sea level changes (Unal and Ghil, 1995). Here we investigate decadal to multidecadal variations in SSH as measured by tide gauges on either side of the North Atlantic. In addition we compare the observed variability with an ensemble of four GCM simulations.

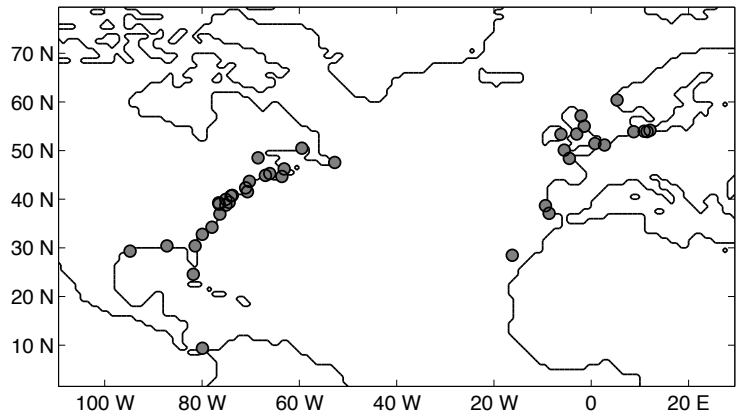

FIGURE 5.1: *Locations of the North Atlantic tide gauges used in the analysis.*

5.2 DATA AND MODEL

The data used in this study consists of Revised Local Reference (RLR) records from the Permanent Service for Mean Sea Level (Woodworth and Player, 2003). Annual means from the longest available records from stations along the eastern and western boundaries of the North Atlantic were selected, linearly detrended and smoothed with a ten year running mean. Analysis showed that the inverted barometer correction has a negligible effect on the results so only the uncorrected data are used here.

Since the available observations are limited in both spatial and temporal extent we also consider data from an ensemble of four simulations of the climate of the 20th century using the Geophysical Fluid Dynamics Laboratory Climate Model version 2.1 (GFDL CM2.1). Model details can be found in Delworth and coauthors (2006). The simulations cover the period 1860 - 2000 using historical forcings and land use changes, with initial conditions for the ensemble members taken from different times during a pre-industrial control run. Since we are interested in natural variability of the climate system rather than the externally forced signal we remove the ensemble mean from each ensemble member before analysis. The data has also been smoothed with a ten year running mean. The AMO in a CM2.1 pre-industrial control run was analysed by Zhang (2008) and it is clear that the dominant period is 20-30 years, as is commonly found in GCMs, rather than 50-70 years as suggested by early observations.

5.3 MULTIDECADAL VARIABILITY IN TIDE GAUGE DATA

Individual tide gauge stations from along the eastern and western boundaries of the North Atlantic are listed in tables 5.1 and 5.2 and the data are plotted in figure 5.2.

The tide gauges records from either side of the North Atlantic are plotted all together in figure 5.3(a) and (b). There is notable synchronicity between the records, particularly

Name	Location	Period
Santa Cruz de Tenerife	28°29'N 16°14'W	1927-1990
Lagos	37°06'N 08°40'W	1908-1999
Cascais	38°41'N 09°25'W	1882-1993
Brest	48°23'N 04°30'W	1807-2006
Newlyn	50°06'N 05°33'W	1915-2007
Nieuwpoort	51°09'N 02°43'E	1943-2006
Sheerness	51°27'N 00°45'E	1832-2007
Dublin	53°21'N 06°13'W	1938-2001
Liverpool	53°24'N 03°00'W	1858-1983
North Shields	55°00'N 01°26'W	1895-2007
Cuxhaven	53°52'N 08°43'E	1843-2006
Warnemunde	54°11'N 12°05'E	1855-2007
Travemunde	53°58'N 10°53'E	1856-2007
Wismar	53°54'N 11°28'E	1848-2007
Aberdeen (1)	57°09'N 02°05'W	1931-2007
Aberdeen (2)	57°09'N 02°05'W	1862-1965
Bergen	60°24'N 05°18'E	1883-2006

TABLE 5.1: *Names, locations and dates of selected tide gauge records along the European margin of the North Atlantic.*

along the western boundary of the North Atlantic. Longer records are available on the eastern side of the Atlantic and, while not as obvious or coherent as in the west, the multidecadal variability remains pronounced. The time scale is clearly 20-30 rather than 50-70 years.

Single time series of SSH along the two coasts are calculated by averaging the available records for each year from the stations along each respective boundary. These are plotted in figure 5.3(c) along with an AMO index (AMOI) which is calculated by averaging SST anomalies (from the HadISST dataset; Rayner et al., 2003) over the North Atlantic from 10°N to the pole. Results are similar if the domain 0° to 75°N is used for the AMOI.

5.4 GCM RESULTS

The AMOI (averaged over the same latitude range as the observations) of the four CM2.1 ensemble members are plotted in figure 5.4(a). All the ensemble members show generally similar behaviour, although there are small differences; ensemble member 3 has the most, and ensemble member 1 the least, regular oscillations. Ensemble member 4 shows

Name	Location	Period
St. John's (Nfld)	47°34'N 52°43'W	1935-2007
Harrington Harbour	50°30'N 59°29'W	1910-1989
Pointe-au-Pere	48°31'N 68°28'W	1900-1983
Charlottetown	46°14'N 63°07'W	1938-2007
Halifax	44°40'N 63°35'W	1895-2007
Saint John	45°16'N 66°04'W	1914-1999
Eastport	44°54'N 66°59'W	1929-2007
Portland	43°40'N 70°15'W	1912-2007
Boston	42°21'N 71°03'W	1921-2007
Woods Hole	41°32'N 70°40'W	1932-2007
Willets Point	40°48'N 73°47'W	1931-2000
New York	40°42'N 74°01'W	1856-2007
Philadelphia	39°57'N 75°08'W	1900-2007
Atlantic City	39°21'N 74°25'W	1911-2007
Lewes	38°47'N 75°06'W	1919-2007
Baltimore	39°16'N 76°35'W	1902-2007
Annapolis	38°59'N 76°29'W	1928-2007
Hampton Roads	36°57'N 76°20'W	1927-2007
Wilmington	34°14'N 77°57'W	1935-2007
Charleston	32°47'N 79°56'W	1921-2007
Mayport	30°24'N 81°26'W	1928-2000
Key West	24°33'N 81°48'W	1913-2007
Pensacola	30°24'N 87°13'W	1923-2007
Galveston	29°19'N 94°48'W	1908-2007
Cristobal	09°21'N 79°55'W	1909-1980

TABLE 5.2: *As for table 5.1 but for the North American side of the North Atlantic.*

slightly longer period variability, closer to 30 than to 20 years.

We look in detail at the AMO in one ensemble member. Figure 5.4 shows Hovmöller plots of temperature (both at the surface and between depths of 284.5 and 415.8 m) and SSH anomalies for ensemble member 2. Westward propagating temperature anomalies with a time scale of 20-30 years are clearly visible below the surface in figure 5.4(c), while 5.4(d) shows that the propagation is not visible at the surface. There is a lag between central and eastern temperatures at the surface of the basin and sub-surface temperatures on the western side of the basin, as seen in the left panels of figure 5.4(c)

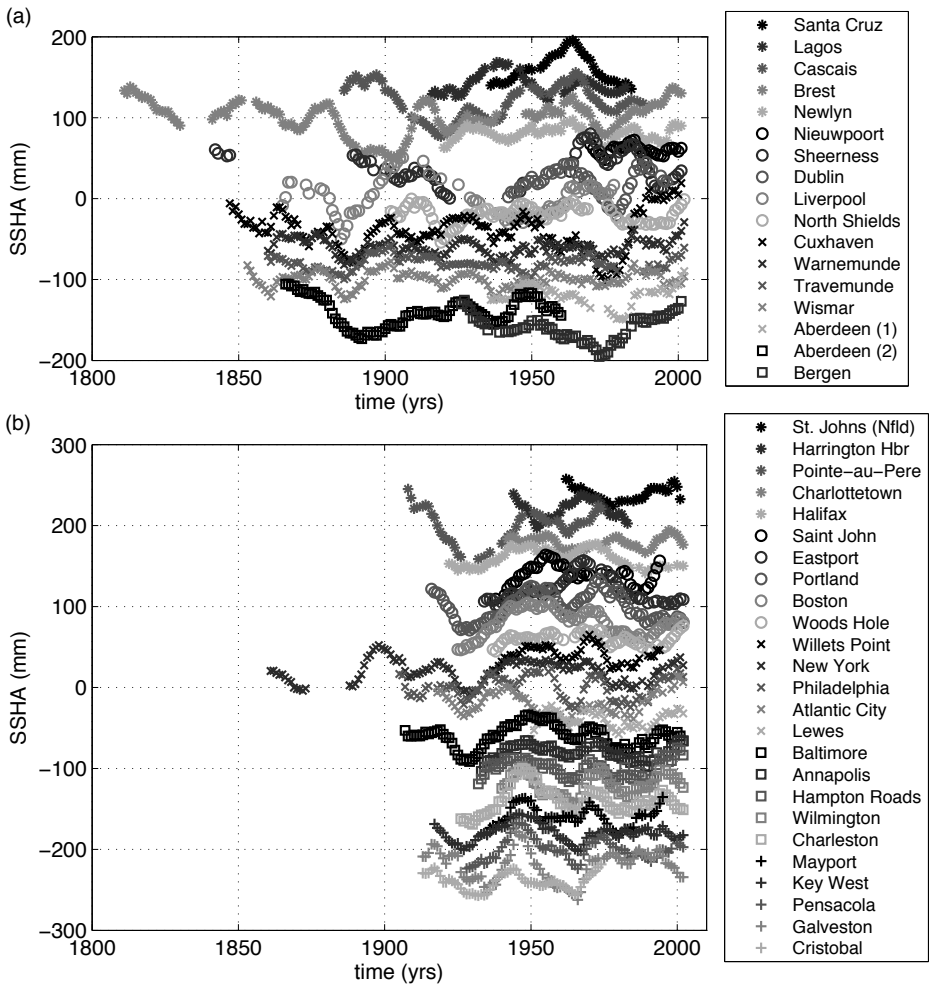

FIGURE 5.2: *North Atlantic tide gauge records used in the analysis. (a) Records from the eastern boundary of the North Atlantic (from Tenerife to Norway), (b) records from the western boundary of the North Atlantic (from Newfoundland to Panama). Each record has been linearly detrended and offset by 20mm.*

and (d), particularly in the earlier part of the time series. Similar features have also been found in observations (chapter 4).

To mimic tide gauge measurements in the model the annual average SSH in the grid points closest to land are taken. Figures 5.4(b) and 5.4(e) show SSH anomalies (SSHA) along the coasts on the western and eastern sides of the North Atlantic for one ensemble member. Comparing figures 5.4(b) and 5.4(e) we see that the strongest signals in both the east and west are found in the northern part of the basin and, similarly to observations, SSH variability is much more coherent with latitude along the western boundary than in the east. This is in agreement with Bingham and Hughes (2009) and Yin et al. (2009),

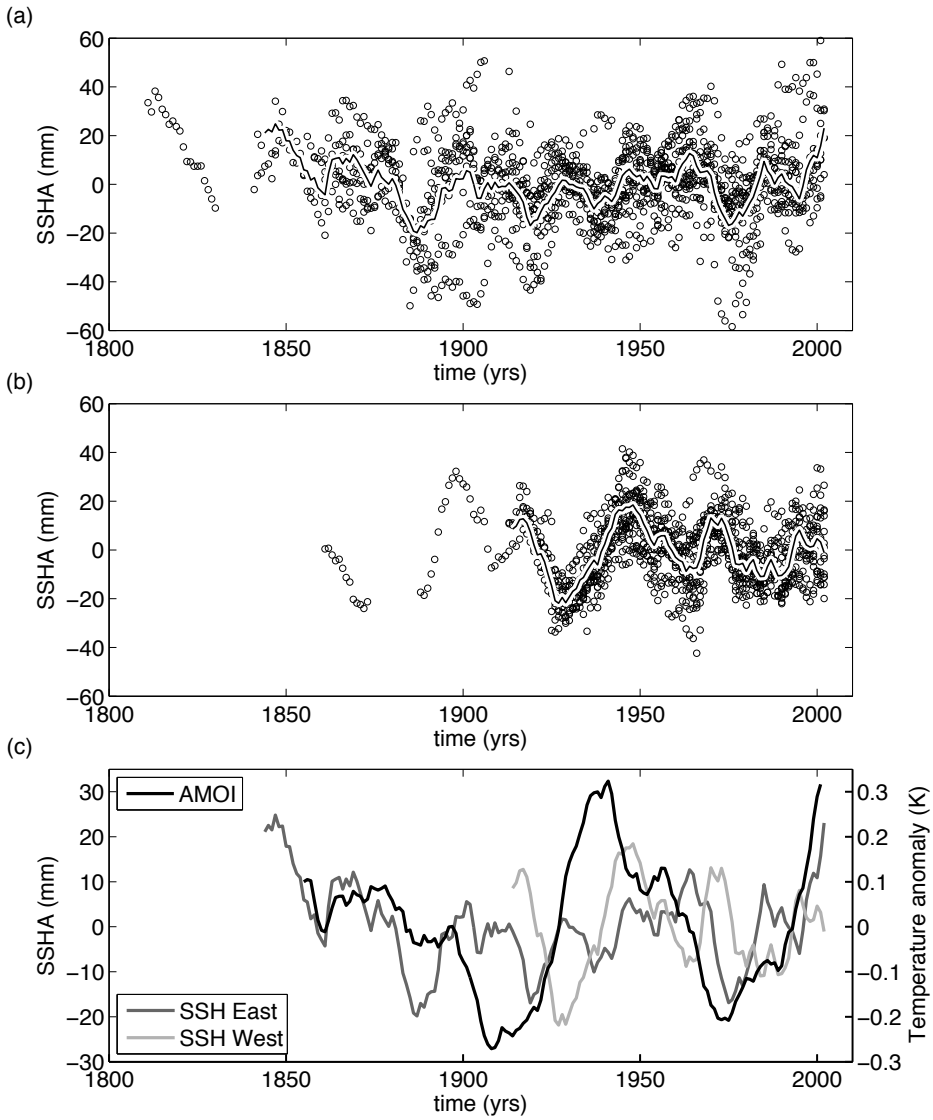

FIGURE 5.3: *(a) Records from the eastern boundary of the North Atlantic (from Tenerife to Norway). Black circles are the individual tide gauge records and the average is shown by the solid curve. (b) As for part (a) but for the western boundary of the North Atlantic (from Panama to Newfoundland). The time series from each tide gauge was linearly detrended before averaging. (c) Averaged SSH anomalies (SSHA) in the east and west (from (a) and (b), in mm, on the left axis), along with the AMO index (AMOI, in K, on the right axis).*

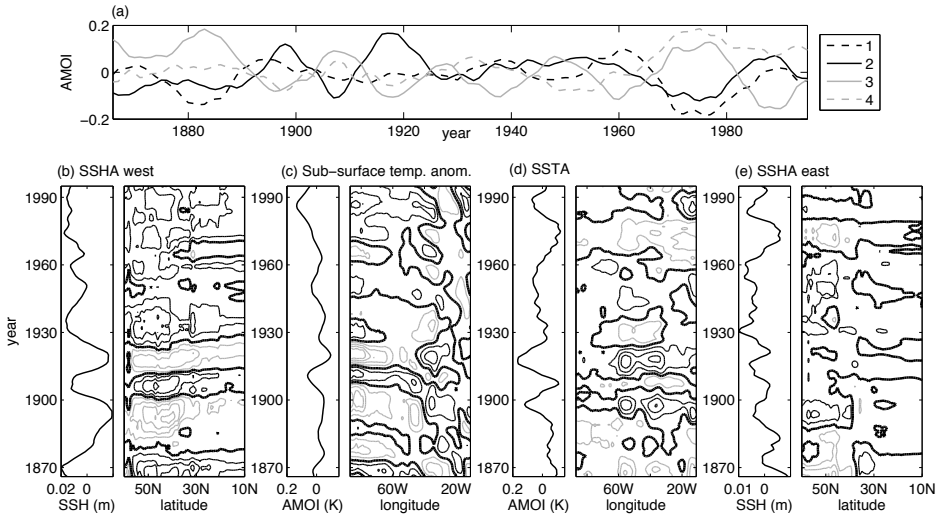

FIGURE 5.4: *(a) AMOI of the four GFDL CM2.1 ensemble members. Results from the second ensemble member showing (b) SSHA along the western boundary of the North Atlantic, both averaged along the coastline (left panel) and as a Hovmöller plot of latitude and time (right panel), (c) temperature anomalies in the North Atlantic between 284.5 and 415.8 m depth averaged over the whole basin (left panel) and as a Hovmöller plot of longitude and time (right panel), (d) as in (c) but for SSTA, and (e) as in (b) but for SSHA along the eastern boundary of the North Atlantic. Contour intervals are 0.01 m for SSH and 0.1 K for temperature, negative contours are in grey. The other three ensemble members show similar behaviour.*

who found coherent signals in SSH along the western boundary related to the strength of the AMOC with a negligible contribution from the eastern boundary. Zhang (2008) found both SST and SSH in the North Atlantic to be significantly correlated with AMOC strength.

Figure 5.4 also indicates that SSH in the model shows the same 20-30 year time scale as temperature. There is a relationship between temperature and SSH which is particularly strong in the west, where warm (cool) sub-surface temperature anomalies are associated with higher (lower) than average SSH. SSH in the east appears to be more closely linked to SST, which is in turn related to sub-surface temperatures in the east.

5.5 CORRELATIONS

Westward propagation of anomalies is a characteristic feature of the internal ocean mode mechanism derived from idealised models (te Raa and Dijkstra, 2002). This mechanism relies on an out of phase response of the meridional and zonal overturning to density anomalies, leading to the westward propagation. This theory also predicts a lag between temperature anomalies (and therefore SSHA) on either side of the basin, with high SSH on the eastern side preceding a high AMOI by zero to a few years, followed about half a period later by high SSH in the west and low SSH in the east, beginning the second half

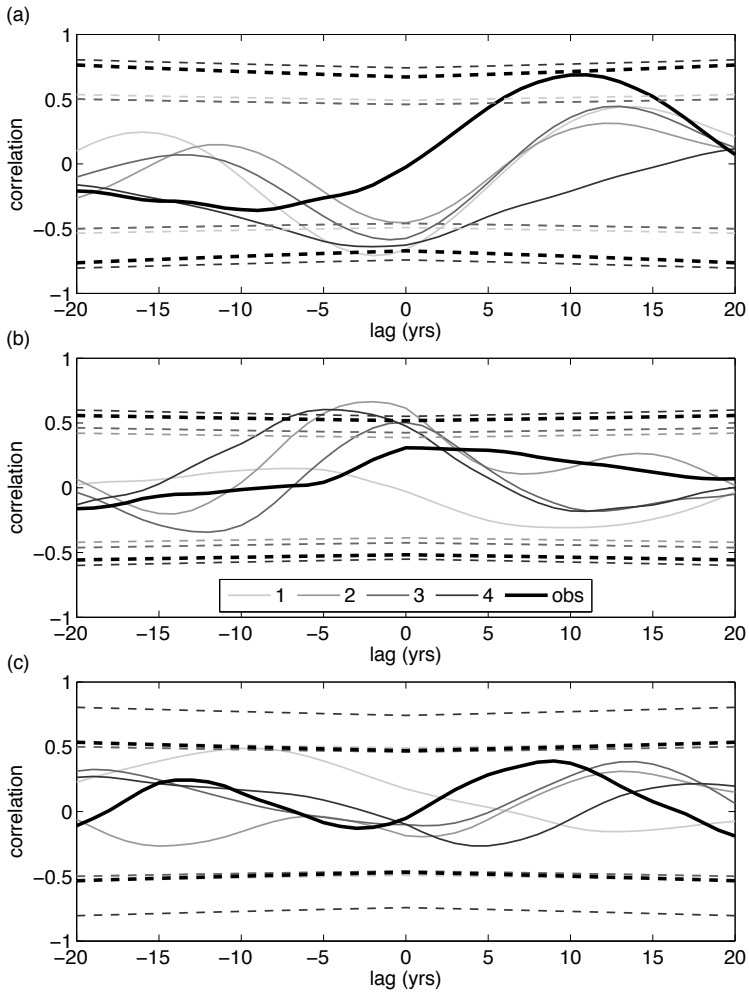

FIGURE 5.5: *Correlations between (a) AMOI and SSHA in the west (positive lag means that AMOI leads), (b) AMOI and SSHA in the east (positive lag means that AMOI leads) and (c) SSHA along the eastern and western boundaries of the North Atlantic (positive lag means that SSH in the east leads) for observations (black curves) as well as the four ensemble members (grey curves). Dashed lines indicate the 95% significance levels.*

of the oscillation.

To determine whether these lags are indeed observed we calculate lag correlations between AMOI and SSH on each coast for observations as well as for the four ensemble members; the results are shown in figure 5.5.

Correlations between AMOI and SSH in the west are plotted in figure 5.5(a). Since the time series are of limited length none of the observational and only a few of the model correlation peaks are significant at the 95% level. We can, however, still check

for consistency with the internal mode mechanism of the AMO. The highest peak in the observed correlations (significant at the 90% level) indicates that a high AMOI leads high SSH in the west by about ten years, consistent with the mechanism. A similar peak is found in three of the four ensemble members (with two of the three peaks significant at the 90% level). All ensemble members show a negative correlation at small negative lags (with two of the four significant at the 95% level), indicating that low (high) SSH on the western boundary leads a high (low) AMOI index. The observations show no such peak. This peak captures the change from one phase of the AMO to the other and indicates that the AMO in the model is more regular than in reality.

Figure 5.5(b) shows correlations between the AMOI and SSHA in the east. Observations are most highly correlated at zero lag, meaning that warmer than average SSTs in the North Atlantic coincide with high sea level along the European coast, as is also seen in the model in figure 5.4(d) and (e). Three of the four ensemble members show significant correlations with SSH in the east leading the AMOI by a few years, consistent with the internal mode mechanism. The observed correlations are not significant, indicating that the signal of the AMO is clearer on the eastern boundary in the model than it is in reality.

Finally, figure 5.5(c) shows correlations between SSH on either side of the basin. The result in this case is unclear; the ensemble members show variable behaviour and there are no significant peaks. The clearest peak in the observed correlations indicates that SSH in the east leads SSH in the west by 8 to 10 years, consistent with the picture of anomalies propagating westward across the basin. Three of the ensemble members have similar peaks, although at longer lags, which, along with the longer lags in the model than in observations in figure 5.5(a) indicates that the model AMO has a slightly longer period than the observed AMO.

5.6 DISCUSSION

The results presented here, together with those of chapter 4, show that there is multidecadal variability in the North Atlantic on 20-30 year time scales, and that this variability is consistent with the internal ocean mode mechanism derived from idealised models (te Raa and Dijkstra, 2002). We have also found the same time scale in both temperature and SSH in the GCM simulations, along with westward propagation of temperature anomalies and consistent correlations between temperature and SSH around the basin.

As mentioned in the introduction, 20-30 year variability has been found in a number of GCMs. Timmermann et al. (1998) explained the 35 year peak in the spectrum of MOC strength in their model as a coupled air-sea mode in which a strong MOC carries warm water to the North Atlantic, affects the atmospheric circulation and leads to negative sea surface salinity anomalies in the convection region which weaken the MOC. Cheng et al. (2004) used a similar explanation for the 20-30 year variability in the MICOM/CCM3 model. Dong and Sutton (2005), on the other hand, did not use atmospheric effects to explain the 25 year peak in the MOC spectrum in HadCM3. In that model a weak MOC led to a build up of cold water and acceleration of the subpolar gyre, which enhanced salinity transport into the convection region, causing enhanced convection and an increase in the MOC.

The link between variability of overturning strength and variability of North Atlantic

temperatures is a consistent feature in both idealised models as well as many GCMs on both the longer and shorter time scales (Delworth et al., 1993; Knight et al., 2005). The pattern of SST generally associated with the AMO on both longer (Kushnir, 1994) and shorter (figure 4.2) time scales is also found in both the idealised model (te Raa and Dijkstra, 2002) and in GCMs (Delworth et al., 1993). In the absence of a longer time series of observations it is difficult to ascertain the dominant period of multidecadal variability in the North Atlantic. An additional consideration is the interaction of the AMO with anthropogenic aerosol variations which may mask shorter term variability (Mann and Emanuel, 2006). The long tide gauge records analysed here certainly point to the importance of the 20-30 year period over the 50-70 year period more commonly associated with the AMO.

ACKNOWLEDGEMENTS

Tide gauge records were obtained from the Permanent Service for Mean Sea Level (http://www.pol.ac.uk/psmsl/datainfo/) and the GCM data from the GFDL coupled climate model webpage (http://nomads.gfdl.noaa.gov/CM2.X/).

6

North Atlantic Multidecadal Climate Variability: An investigation of dominant time scales and processes

The issue of multidecadal variability in the North Atlantic has been an important topic of late. It is clear that there are multidecadal variations in several climate variables in the North Atlantic, such as sea surface temperature and sea level height. The details of this variability, in particular the dominant patterns and time scales, are confusing from both an observational as well as a theoretical point of view. After analysing results from observational data sets and a 500 year simulation of an IPCC-AR4 climate model we propose that there are two dominant time scales (20–30 years and 50–70 years) of multidecadal variability in the North-Atlantic. The 20–30 year variability is characterised by westward propagation of subsurface temperature anomalies. The hypothesis is that the 20–30 year variability is caused by internal variability of the Atlantic Meridional Overturning Circulation (MOC) while the 50–70 year variability is related to atmospheric forcing over the Atlantic Ocean and exchange processes between the Atlantic and Arctic Ocean.

This chapter is based on:
North Atlantic Multidecadal Climate Variability: An investigation of dominant time scales and processes, by L. M. Frankcombe, A. S. von der Heydt and H. A. Dijkstra, *accepted by the Journal of Climate*.

6.1 INTRODUCTION

Analysis of multiple data sets of the Atlantic climate system has shown that many quantities show variations on a multidecadal time scale. The first analyses (Schlesinger and Ramankutty, 1994; Kushnir, 1994) were based on sea-surface temperature (SST) and indicated variability on a time scale of 50–70 years. Indeed, when a ten-year running mean of North Atlantic SST anomalies is constructed, the Atlantic is found to have been coldest around 1920 and 1980, and relatively warm around 1950 as well as over the last decade (Enfield et al., 2001; Sutton and Hodson, 2005). Although only a few cycles can be identified from the instrumental SST record, the variability is often referred to as the 'Atlantic Multidecadal Oscillation' (AMO; Kerr, 2000).

Water from the North Atlantic enters the Arctic Ocean through Fram Strait and the Barents Sea. The return flow of water from the Arctic occurs mainly via the East Greenland Current. This exchange forms an oceanic connection between the climates of the Arctic and the North Atlantic. Century long records of sea-ice extent in the Arctic display multidecadal variability (Venegas and Mysak, 2000), which has been referred to as the Low Frequency Oscillation (LFO; Polyakov and Johnson, 2000). This variability is strongest in the Kara Sea and decays towards the Canada Basin (Polyakov et al., 2003a). There are also multidecadal variations in sea-ice transport through Fram Strait associated with the sea-ice extent variability (Vinje et al., 2002).

The other connection between the North Atlantic and Arctic climate occurs through the atmosphere. The dominant atmospheric winter variability is the pattern of the North Atlantic Oscillation (NAO), with its Arctic extension, the Northern Annular Mode (NAM; Thompson and Wallace, 2001). Although it cannot be demonstrated that the NAO has any significant preferential frequency, the Atlantic westerlies were relatively weak in the period between 1940–1970 and relatively strong from 1980 to present. NAO variations impose a relatively well-known tri-polar SST anomaly on the North Atlantic Ocean on seasonal to interannual time scales (Eden and Jung, 2001; Alvarez-Garcia et al., 2008) while the low frequency response of the ocean to the NAO is more of a basin wide single sign pattern (Visbeck et al., 2003).

A mechanistic understanding of the phenomena of multidecadal variability is important for several reasons. There are strong indications that summer temperatures in Western Europe and precipitation variations, in particular in the continental USA, are related to the AMO (Enfield et al., 2001; Sutton and Hodson, 2005). Second, multidecadal variations may contribute to changes in global mean surface temperature and hence may alternately mask and enhance temperature and precipitation changes due to increasing levels of greenhouse gases (Zhang et al., 2007). Third, if there are preferred patterns of multidecadal variability then these may play a significant role in climate predictability on these time scales (Griffies and Bryan, 1997; Keenlyside et al., 2008). Finally, understanding this variability is an important component of any general theory of climate variability and climate change.

This study is motivated by the rather contradictory results which have appeared in studies with general circulation (climate) models (GCMs) of multidecadal variability in the North Atlantic climate system. A time scale of SST variability close to 25 years has been found in several GCMs (Timmermann et al., 1998; Cheng et al., 2004; Dong and Sutton, 2005). On the other hand, Jungclaus et al. (2005) and Vellinga and Wu (2004) found dominant Atlantic SST variability on time scales of 70 and 100 years, respectively.

A variety of mechanisms of the phenomena (Delworth et al., 1993; Vellinga and Wu, 2004; Jungclaus et al., 2005; Knight et al., 2005) have been suggested based on GCM results. Some suggest that coupled ocean-atmosphere interaction (Timmermann et al., 1998) is necessary. Others explain it as a dynamical oceanic response to atmospheric low-frequency variability (Delworth and Greatbatch, 2000). Finally, a central role for the Atlantic-Arctic ocean connection has been suggested (Jungclaus et al., 2005) while others attribute a role for processes in the Tropical Atlantic (Vellinga and Wu, 2004; Knight et al., 2005).

In this paper, we analyse results from many observational data sets and from a long simulation of the Geophysical Fluid Dynamics Laboratory CM2.1 climate model to provide a more detailed picture of North Atlantic multidecadal variability and the dominant processes involved. Our study provides support to the hypothesis that there are two dominant time scales of multidecadal variability in the North Atlantic climate system: a 20–30 year and a 50–70 year variability. We argue that the 20–30 year variability is caused by internal variability of the Atlantic Meridional Overturning Circulation (MOC), while the longer 50–70 year variability is related to low-frequency atmospheric forcing and Arctic-Atlantic exchange processes.

In section 6.2 we (re)analyse both oceanic, atmospheric and cryospheric observations as well as a control simulation of the GFDL CM2.1 with a focus on the dominant time scales of multidecadal variability in the North Atlantic and Arctic oceans. In section 6.3 we study the spatial patterns of variability by using Multichannel Singular Spectrum Analysis (M-SSA; Ghil et al., 2002a) and in section 6.4 we discuss possible mechanisms for the 20–30 year and the 50–70 year variability. Our main conclusions are presented and discussed in section 6.5.

6.2 DOMINANT MULTIDECADAL TIME SCALES

In this section, we consider the temporal signature of North Atlantic climate multidecadal variability using observations (subsection 6.2.1) and GCM results (subsection 6.2.2).

6.2.1 OBSERVATIONS

The fact that the North Atlantic SST observations used to define the AMO are at most 150 years long gives rise to problems in detecting and understanding multidecadal variability. We can, however, also study variability in the North Atlantic ocean by using land based observations, since the basin-wide temperature anomalies that characterise the AMO affect the climate of the surrounding land masses (Sutton and Hodson, 2005).

There are only a few directly measured time series from which multidecadal variability can be reliably determined. One of these is the Central England Temperature (CET) record which dates back to the second half of the 17^{th} century (figure 6.1(a)). The SSA spectrum (Ghil and Vautard, 1991) of this time series (figure 6.1(b)) indicates that the dominant time scales of variability are in the 20–30 year band (consistent with the analysis of this time series presented in Plaut et al., 1995) and at $\sim$70 years. Both these peaks are significant at the 99% level.

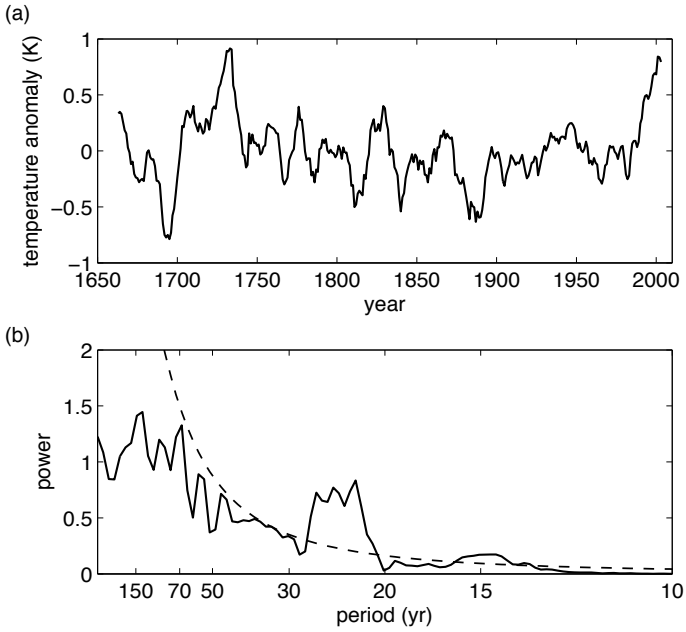

FIGURE 6.1: *(a) Time series (linearly detrended and smoothed with a ten year running mean filter) and (b) SSA spectrum of the (unsmoothed) Central England Temperature record. The dashed curve is the 99% significance level using red noise as the null hypothesis.*

In the absence of other long instrumental time series we turn to proxy records. Proxy data go back longer in time, but for these data an additional interpretation step is needed. Long series of net snow accumulation rates in central Greenland were obtained by Banta and McConnell (2007) and the time series and SSA spectra of the two longest of their four records are shown in figure 6.2. Both cores show variability at periods of 20–30 years that is significant at the 90% level.

So why is it that the CET and Greenland ice cores show a dominant 20–30 year variability while the basin-wide SST variability is suggested to have a dominant 50–70 year variability (Schlesinger and Ramankutty, 1994; Enfield et al., 2001)? To explain this we consider so-called latitudinal AMO indices, where the 10-year running mean of the North Atlantic SST anomaly in 10° latitude bands is determined (figure 6.3) using SSTs from the HadSST2 data set (Rayner et al., 2006). Before about 1900 the variability at low latitudes appears to be out of phase with the variability at mid latitudes so that the basin-wide averaged variability (solid black curve in figure 6.3) is very small. This may also be due to the scarcity of data during this period. After 1900 the variability is much more coherent over latitude with the cooler period around 1950 being much more pronounced at lower latitudes than at higher latitudes. The 20–30 year component is dominant in each individual latitudinal band, but although it remains visible in the basin wide AMO index (AMOI) it appears overwhelmed by the 50–70 year component. Further signatures of the 20–30 year variability were found from the analysis of subsur-

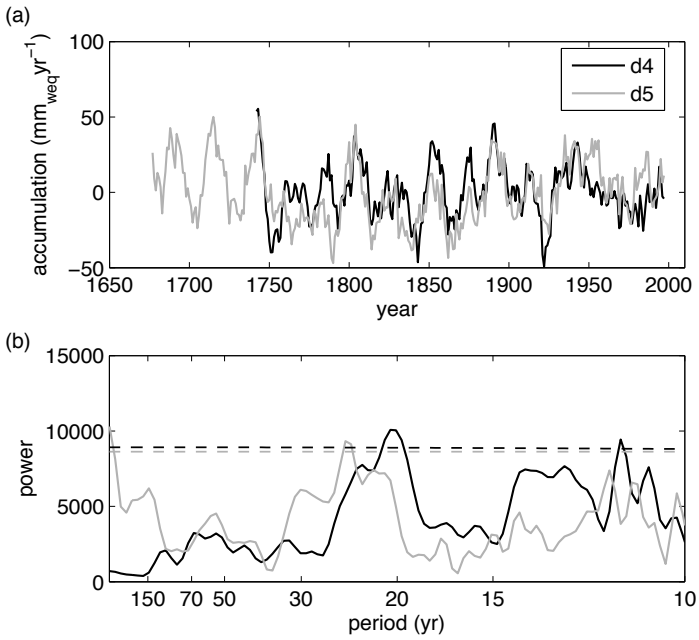

FIGURE 6.2: *(a) Time series (linearly detrended and smoothed with a ten-year running mean filter) and (b) SSA spectra of the (unsmoothed) net snow accumulation rates (in mm of water equivalent per year) for two Greenland ice cores (Banta and McConnell, 2007). The dashed curves are the 90% significance level.*

face temperature (XBT) data in chapter 4. Although there are only subsurface data from 1960–2000, it was suggested that the dominant period of variability is 20–30 years. In chapter 5, it is shown that tide gauge data around the North Atlantic also supports the notion of a dominant time scale of 20–30 years.

Apart from temperature (and salinity) anomalies in the North Atlantic ocean, there are many other signatures of multidecadal variability in the North Atlantic climate system. In the Arctic, sea-ice extent, the temperature of the Atlantic core water and the atmospheric surface temperature all vary on multidecadal time scales (Venegas and Mysak, 2000; Polyakov et al., 2003c, 2004; Divine and Dick, 2006), with indications of a 50–70 year period. In addition, there are the decadal scale appearances of the Great Salinity Anomalies in the North Atlantic, of which several are thought to be connected to large sea-ice exports out of the Arctic (Belkin et al., 1998). This makes the Arctic a likely candidate for affecting variability in the North Atlantic on the time scales of interest.

It is clear that variability in the North Atlantic ocean propagates towards the Arctic through Fram Strait as well as along the Norwegian coast into the Barents Sea. Long time series of observations of sea ice extent in four Arctic seas are available and are plotted with the AMOI in figure 6.4(a). As already shown by Polyakov et al. (2004), there is substantial multidecadal variability in sea-ice extent, and correlations with the AMO index (significant at the 95% level in the Kara sea, figure 6.4(b)) show that a high AMO index precedes a minimum in sea ice extent. This is consistent with the

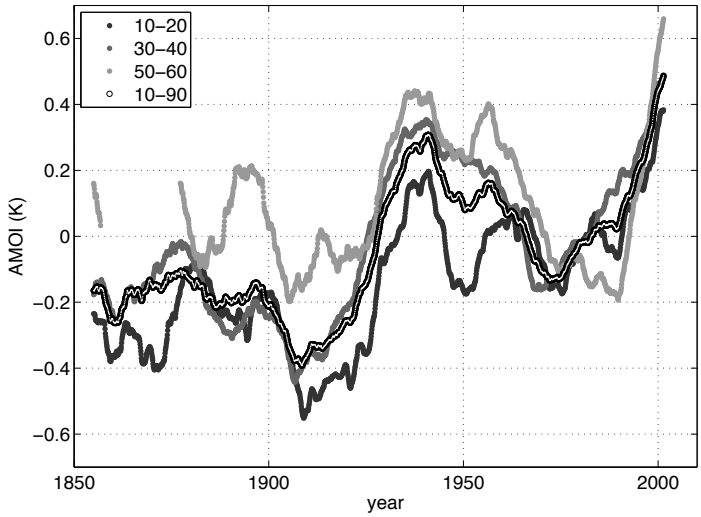

FIGURE 6.3: *Latitudinal band averages of temperature anomalies in the North Atlantic from the HadSST2 data set. The solid black curve shows temperature anomalies averaged over the basin from 10°N – 90°N, the dashed black curve shows anomalies averaged from 10°N – 20°N, the solid grey curve from 30°N – 40°N and the dashed grey curve from 50°N – 60°N. A 10-year running mean filter has been applied to remove short time scale variability.*

propagation of warm Atlantic water into the Arctic causing a decrease in sea ice.

In summary, from observations it is clear that in addition to the previously described 50–70 year variability found in the North Atlantic and Arctic, a dominant time scale of 20–30 years may be found in SST over the North Atlantic as well as in temperatures in central England and net snow accumulation rates in Greenland.

6.2.2 GCM RESULTS

Several models from the Coupled Model Intercomparison Project (CMIP) suite (Stouffer et al., 2006) display clear multidecadal variability in the North Atlantic. We focus here only on the model control simulations, which have a time integration interval of longer than 500 years. In particular, the recent analysis (Zhang, 2008) of the 1000 year control simulation of the GFDL CM2.1 model shows dominant variability in the 20–30 year time scale (figure 2b in Zhang (2008)). The first EOF shows a dipolar pattern in both SSH and subsurface temperature with strong positive anomalies south of Greenland and negative anomalies in the Gulf Stream separation region. We analysed the last 500 years of this simulation (for which data were available) in more detail by looking at the variability in surface as well as subsurface temperatures. The AMO indices (North Atlantic between 10°N and 80°N) for SST and for the 300-400 m averaged subsurface temperature are plotted in figure 6.5(a) and their spectra in figure 6.5(b). The basin-wide signal displays variability on both the 20–30 and 50–70 year time scales, both at and below the surface. When the spectra of the AMO indices (surface and subsurface) are

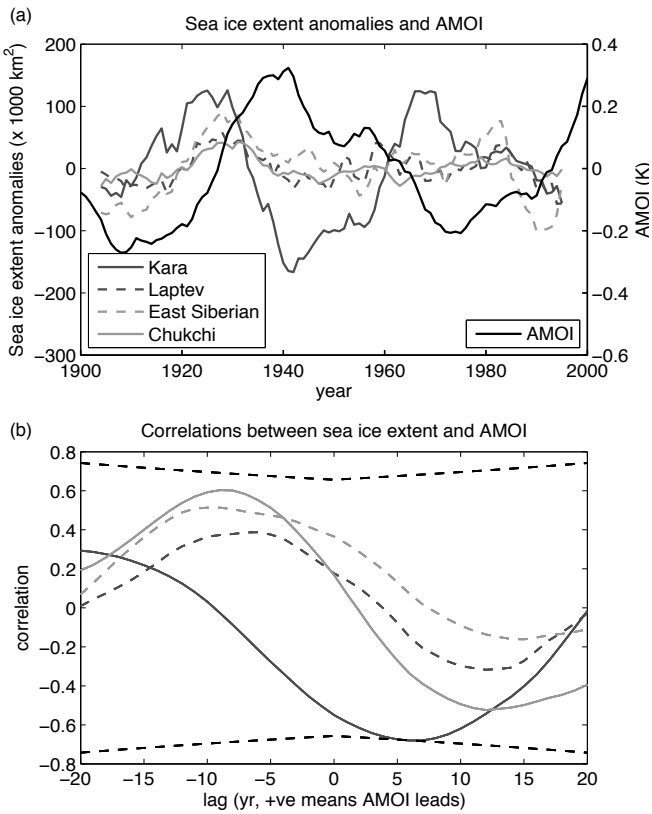

FIGURE 6.4: *(a) Observations of sea ice extent (smoothed with a ten year running mean filter) in four Arctic seas (from Polyakov et al., 2003c) along with the basin wide AMO index (AMOI; 10°N – 90°N) and (b) correlations between each of them and the AMOI (the dotted line represents the 95% confidence interval).*

analysed per latitudinal band (figure 6.6), one finds (similar as in observations) shorter periods at lower latitudes and in the subsurface and larger periods at midlatitudes and at the surface. Note that for every latitude, however, the 20–30 year subsurface variability has significant energy.

The result from the GFDL CM2.1 model that there exists two dominant time scales of variability is also in accordance with some other GCMs in the CMIP suite. In a 1000-yr control simulation of HadCM3, Dong and Sutton (2005) find variability in the Atlantic MOC with a dominant time scale of about 25 years. There is also variability at the 50–70 year band, but this is not significant (not even at the 90% level, their figure 2) although there is significant variability at the 100 year time scale. Vellinga and Wu (2004) analyse this 100 year variability in a 1600 year control simulation of HadCM3. From the anomaly patterns of the model at this time scale, it is clear that there is no westward propagation and that the time scale is too long for their mechanism to be a plausible candidate for the 20–30 year variability as found in the observations. The HadCM3 model simulation, however, also shows variability at the 20–30 year time scale

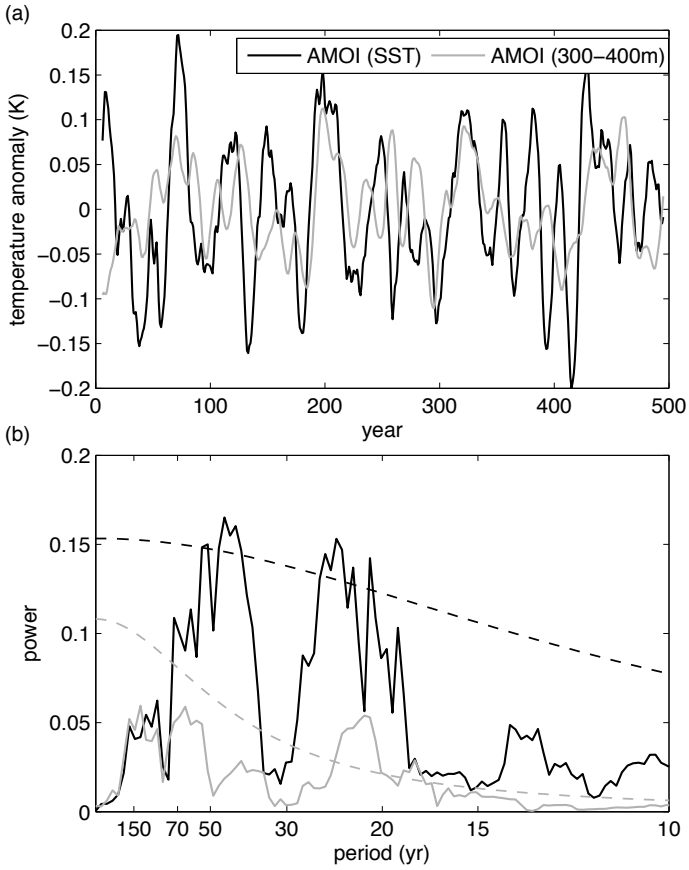

FIGURE 6.5: *(a) Time series (linearly detrended and smoothed with a ten year running mean filter) and (b) SSA spectra of two (unsmoothed) AMOI (black: surface, grey: subsurface) of the last 500 years of the CM2.1 control simulation (Zhang, 2008). Dashed curves show the 99% significance levels.*

(figure 4 in Vellinga and Wu (2004)). Jungclaus et al. (2006) analyse a 500 year control integration with the ECHAM5/MPI-OM model and find a pronounced multidecadal fluctuations in the Atlantic MOC and associated heat transport with a period of 70-80 years. From a different simulation with the same model (Sterl et al., 2008) it appears that the dominant variability in the AMO index is in the 20-40 year band. Variability on the longer time scale, 50-80 years, also exists but it is not significant at the 95% level (van Oldenborgh et al., 2009).

6.3 DOMINANT SPATIAL PATTERNS

Because of the relatively short observational time series ($\sim$150 year of SST and SLP), it is difficult to extract a dominant pattern of multidecadal variability with much confi-

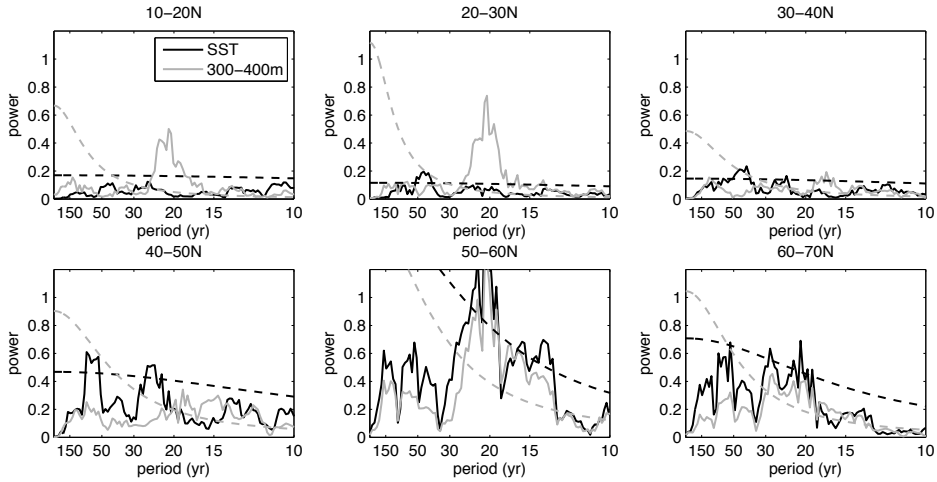

FIGURE 6.6: *Spectra of the latitudinal band anomalies of (unsmoothed) temperature in the GFDL CM2.1 control simulation (black: SST, grey: subsurface). Dashed curves show the 95% significance levels.*

dence. Kaplan et al. (1997) and Delworth and Mann (2000) present a reconstruction of a signal with a ~ 50 year period which shows a near standing pattern in SST and SLP. The SST pattern is basin wide with the largest anomalies appearing south of Greenland.

In the GFDL CM2.1 model results, however, much more detail on spatial patterns can be obtained. In the meridionally averaged Hovmöller diagrams at the surface (figure 6.7(a)) the dominant period appears to be 50–70 years while in the subsurface data (especially in the western part of the domain) the anomalies have larger amplitude and the shorter period appears dominant (figure 6.7(b)). The difference between the dominant time scales of variability at different depths is most clearly seen in figure 6.7(c), in which the upper part of the plot shows the basin averaged temperature anomalies at various depths. The lower plot shows a Hovmöller diagram of time versus basin averaged temperature anomalies down to a depth of 1000 m. The time scale of variability is shortest in the subsurface (at around 200–300 m depth) and is longer both above and below this depth.

An M-SSA analysis was performed on the model results, focusing on the periods and horizontal patterns of temperature and salinity at the surface and at a depth of 400 m, both over the North Atlantic up to the Arctic basin (with the domain 18.7°N – 90°N and 78°W – 40°E) and over the Arctic alone (domain north of 70°N). The depth of 400 m was chosen since that is the approximate depth of the layer of Atlantic water in the Arctic ocean. A window length of 100 years was used and the data was not smoothed beforehand. Two methods of estimating the lag covariance matrix were used (Vautard-Ghil (Vautard et al., 1992) and Reduced covariance), as well as two significance tests (Monte-Carlo and Chi-squared). A peak was judged to be significant if it was above the 95% significance level in both tests using both estimation methods. The significant M-SSA modes are listed in table 6.1 along with the percentage of the variance that they explain and their periods (where the period was calculated using the spectra of the

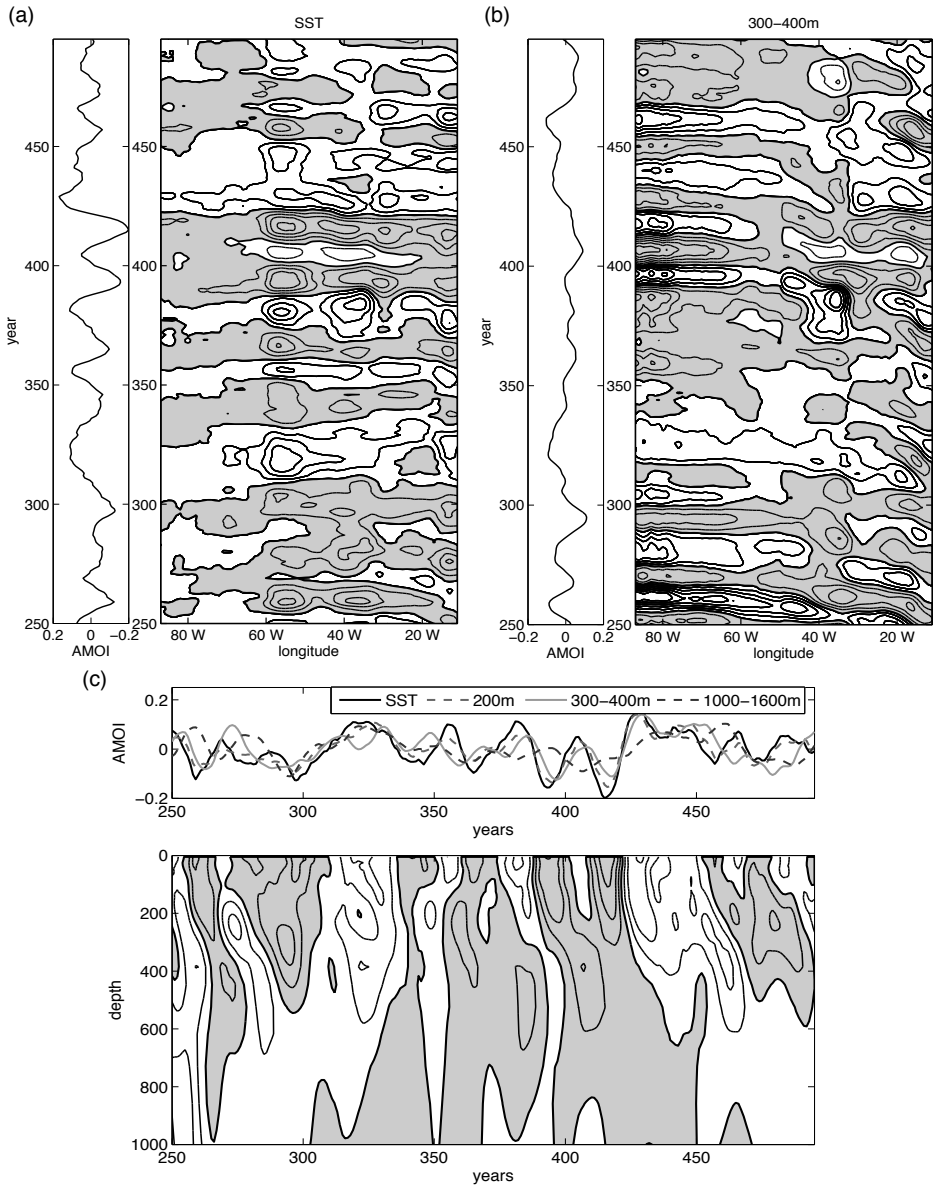

FIGURE 6.7: *(a) Basin averaged AMOI (left) and a Hovmöller diagram of meridionally (10°N – 90°N) averaged temperature anomalies of SST (right) from the last 250 years of the CM2.1 control simulation. (b) Same as (a) but for the subsurface temperature anomalies. (c) Basin averaged temperature anomalies at different depths (upper) and a Hovmöller plot of basin averaged temperature anomalies versus depth (lower). Data has been smoothed with a ten year running mean filter. Negative regions are shaded.*

Domain	Quantity	Period	% Variance	
	SST	20–30 yrs	7.4%	figure 6.8
		∼15 yrs	4.6%	
North	SSS	20–30 yrs	7.7%	
Atlantic	T_{400}	20–30 yrs	13.7%	figure 6.9
		∼15 yrs	6.6%	
	S_{400}	20–30 yrs	15.7%	
	SST	30–50 yrs	5.2%	figure 6.10
		20–30 yrs	4.6%	
	SSS			
	T_{400}	20–30 yrs	10.2%	
Arctic		>50 yrs	35.4%	figure 6.11
		30–70 yrs	18.4%	
	S_{400}	30–50 yrs	13.6%	
		30 yrs	9.5%	figure 6.12
		20–30 yrs	4.2%	

TABLE 6.1: *Periods and variance of the significant M-SSA modes. The analysis was carried out over two domains, the North Atlantic (18.7°N – 90°N, 78°W – 40°E) and the Arctic (north of 70°N) for four variables: sea surface temperature (SST), sea surface salinity (SSS), temperature at 400 m depth (T_{400}) and salinity at 400 m depth (S_{400}). For each significant mode the period and % variance explained are listed, along with the figure number of the modes whose spatial patterns are plotted.*

principle components of each mode). The analysis found, in general, that certain periods emerged repeatedly from the M-SSA analysis; the recurring peaks were at approximately 15 years, 20–30 years, 30–50 years, 50–70 years and occasionally a greater than 70 year peak. However not all of these peaks were found to be significant. When the domain included the North Atlantic only the 20–30 and sometimes the 15 year peaks were significant, while in the Arctic the longer periods also emerged above the red noise.

Figure 6.8 shows the leading pattern that results from the M-SSA analysis of SST anomalies in the GFDL CM2.1 control simulation. This oscillation has a period of 20–30 years. Other very similar spatial patterns with periods of 30–50 and 50–70 years also emerge, although they are not found to be significant. The temperature patterns at 400 m depth have their main region of variability further south (figure 6.9) although the 20–30 year period remains the same. As for SST, similar patterns are found for longer periods. The M-SSA modes of salinity at the surface and at a depth of 400 m over this domain show very similar periods and spatial patterns to the temperature modes.

M-SSA modes of temperature in the Arctic show that the dominant variability at both the surface and 400 m is in the Nordic Seas and the Atlantic section of the Arctic, as in figure 6.10. The temperature anomalies do not penetrate far into the Arctic proper,

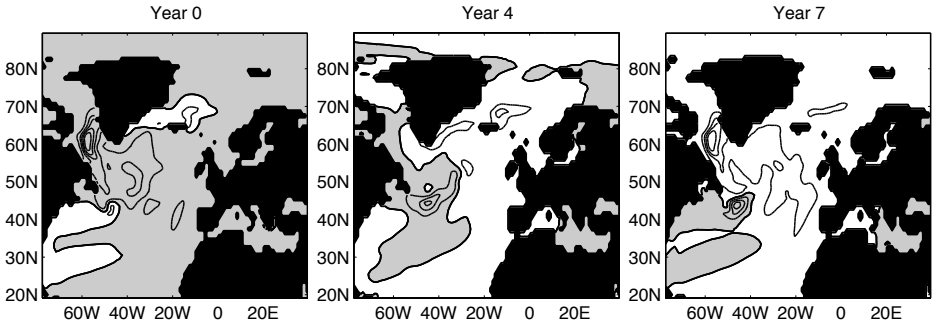

FIGURE 6.8: *Spatial pattern of the first M-SSA pair of North Atlantic SST, with a period of 20–30 years, explaining 7.4% of the variance in SST. The amplitude is arbitrary, negative regions are shaded.*

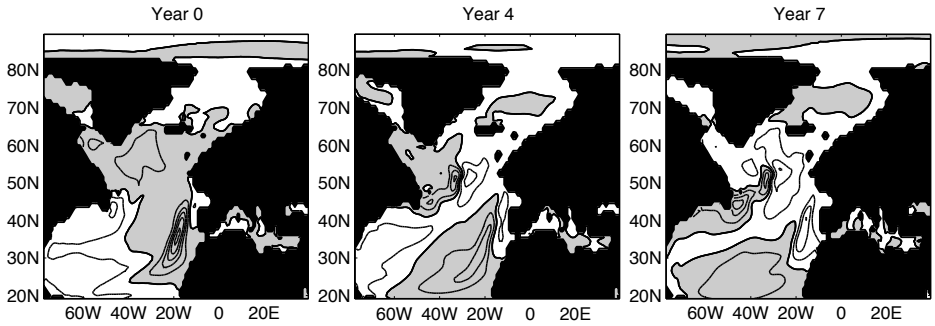

FIGURE 6.9: *Spatial pattern of the first M-SSA pair of temperature at 400 m (T_{400}), with a period of 20–30 years, explaining 13.7% of the variance in 400 m temperatures.*

although some deeper anomalies do propagate along the continental shelf. Warm water from the North Atlantic can thus contribute to melting sea ice in the Arctic marginal seas which is consistent with the observations of sea-ice extent lagging AMO index (shown in figure 6.4).

No significant oscillatory variability is found in salinity at the surface in the Arctic ocean. There is, however, significant variability in salinity at 400 m depth on a range of time scales. The dominant period is 50-100 years. This variability is concentrated in the Beaufort Sea but anomalies spread over the whole Arctic (figure 6.11). Coupling between the North Atlantic and the Arctic is seen in salinity at the same depth but on the shorter 20–30 year time scale. figure 6.12 shows how a salinity anomaly from the North Atlantic enters the Arctic and travels eastwards around the basin. Anomalies propagating from the Arctic back to the North Atlantic would flow through Fram Strait and along the coast of Greenland and may provide a mechanism for the so-called 'Great Salinity Anomalies' (Belkin et al., 1998).

Modes of atmospheric variability over the Arctic can be studied through an M-SSA analysis of modeled sea level pressure. The unfiltered time series shows variability only on shorter time scales (less than 20 years) but if the data is filtered to allow periods of

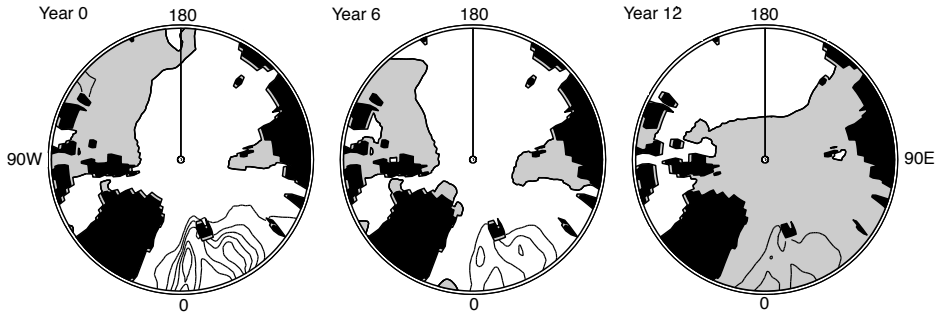

FIGURE 6.10: *Spatial pattern of the first M-SSA pair of SST over the Arctic with a period of 30–50 years, explaining 5.2% of the variance.*

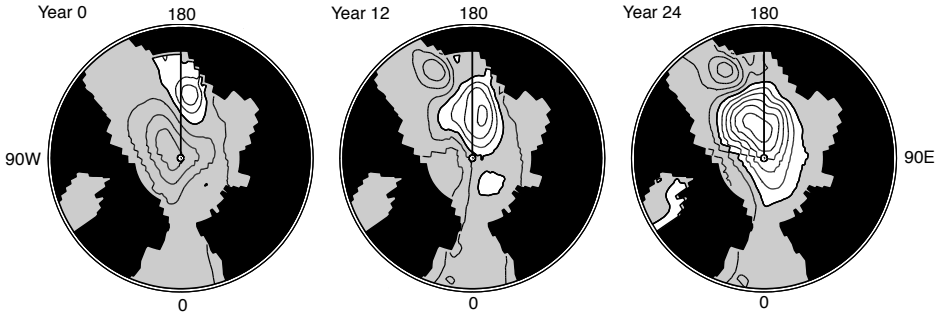

FIGURE 6.11: *Spatial pattern of the first M-SSA pair of salinity at 400 m depth (S_{400}) over the Arctic with a period longer than 50 years. This pair explains 35.4% of the variance in 400 m salinity.*

between 30 and 100 years then significant variability between 30 and 50 years becomes apparent (not shown).

6.4 PHYSICAL MECHANISMS

From the analysis of available observations and control runs of AR4 coupled models, it can be concluded that the 20–30 year variability is present in both observations and models, and that the subsurface temperature signal is associated with westward propagation. Another signal appears at the 50–70 year time scale and also variability at centennial scales ($\sim$ 100 years) is found in models such as HadCM3. In the first subsection below, we discuss a possible mechanism for the 20–30 year variability. This is followed by a section where we propose several mechanisms to explain the 50–70 year variability.

6.4.1 PHYSICS OF THE 20–30 YEAR VARIABILITY

The 20–30 year variability can be understood in terms of the excited internal mode mechanism as developed from idealised models (te Raa and Dijkstra, 2002, chapter 2 of this thesis).

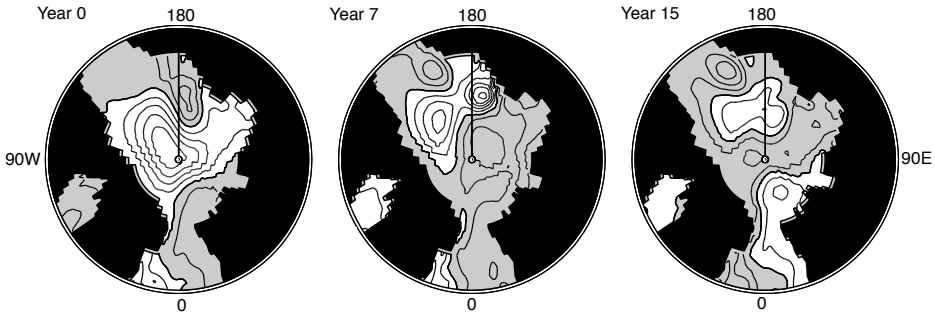

FIGURE 6.12: *Spatial pattern of the fourth M-SSA pair of salinity at 400 m depth over the Arctic with a period of 30 years, explaining 9.5% of the variance.*

The most convincing characteristic of this mechanism, i.e., the westward propagation of temperature anomalies, is indeed found in subsurface temperature observations. Figure 4.3 in chapter 4 shows a Hovmöller plot of temperature anomalies, basin (10°N – 60°N) and vertically averaged over 300-400 m, westward propagation is easily identified. For example, the mid Atlantic subsurface warming (at 60°W) which was at a maximum around 1978 started in the eastern past of the basin around 1970 and reached the west coast around 1981. The phase differences between zonal and meridional temperature differences shows a maximum correlation around 5 years, which leads, according to the mechanism above, to an estimate of the period of about 20 years, consistent with the variability in the Central England Temperature record (figure 6.1). Phase differences between variability on the eastern and western boundaries of the North Atlantic is also found in sea level (Miller and Douglas, 2007, chapter 5) and can also be explained by westward propagating anomalies with a time scale of 20–30 years.

There is also clear westward propagation in the subsurface temperature field in the GFDL CM2.1 control simulation, as can be seen from figure 6.7(b). The SST signal is much more stationary at the surface in figure 6.7(a), which is also seen in observations. This difference in propagation can be explained by the theory of te Raa and Dijkstra (2002) as the background zonal flow is a parameter in the propagation speed.

Results from other GCMs may be reconsidered in relation to this mechanism. Dong and Sutton (2005) found two significant peaks in the spectrum of MOC variability in HadCM3, one at $\sim$25 years and one at $\sim$90 years. The shorter period variability was associated with variations in density in the northern North Atlantic, with the lagged correlations between density and overturning strength consistent with the mechanism discussed here. Delworth et al. (1993) also found MOC variability lagging density variations, as well as westward propagation of anomalies at the surface.

With these many indications of westward propagation and a mechanism based on clear physics independent of frictional parameterisations (i.e. only based on thermal wind), we tend to put a great deal of confidence on the hypothesis that the 20–30 year variability can be attributed to an excited multidecadal internal ocean mode, as described in chapter 2. We are then left with the issue of explaining the 50–70 year variability.

6.4.2 POSSIBLE CAUSES OF THE 50–70 YEAR VARIABILITY

Considering the results of the analyses above, the 50–70 year variability has the following properties distinguishing it from the 20–30 year variability:

(i) It is more pronounced at the surface than in the subsurface in the North Atlantic.

(ii) It is the dominant variability in the Arctic ocean, seen most clearly in subsurface salinity.

There are several possibilities for the source of the longer period variability:

(i) Modulation of the 20–30 year variability.

(ii) Excitation by the atmosphere.

(iii) Interaction between the North Atlantic and the Tropical Atlantic.

(iv) Interaction between the North Atlantic and the Arctic.

Each of these will be discussed below.

One possibility is that the 50–70 year variability is caused by the same processes as the 20–30 year variability. In idealised models, where an internal ocean mode is excited by atmospheric noise, the spectrum shows a broad peak at multidecadal frequencies (see, for example, figure 3.6). This means that both the 20–30 year and 50–70 year periods could be encompassed by the same spectral peak. However, figure 6.5 shows that the spectra of temperature variability in the North Atlantic seem to have distinct peaks at 20–30, 30–50 and 50–70 years, thus it seems that the variability has a preference for particular periods rather than being purely red (Hasselmann, 1976). This could be caused by a series of weak oscillations followed by a particularly strong anomaly, making the period of the oscillation appear longer than the underlying 20–30 years. This hypothesis is borne out by the M-SSA analysis of temperature and salinity in the North Atlantic in the GFDL CM2.1 control run, which finds oscillatory M-SSA pairs at the various frequencies which have very similar spatial patterns, but only the pairs showing variability at around 30 years are significant.

A second possibility is that the 50–70 year variability is forced by the atmosphere, in particular through multidecadal variability of the North Atlantic Oscillation. This mechanism was considered in the nice study of Eden and Jung (2001), where an eddy-permitting ocean GCM was forced by heat, freshwater and momentum anomalies of multidecadal NAO variability. Although it was found that direct forcing by the NAO heat flux anomalies cannot explain the SST cooling in the 70's, for example, it was shown that a lagged response of the Atlantic MOC to the forcing can explain this behavior. Clearly, the variability in Eden and Jung (2001) is on a much larger time scale than the 20–30 year variability (their figure 3, for example) and so the NAO forcing combined with a lagged MOC response cannot explain this shorter time scale variability. Eden and Jung (2001) also show that the variability is mainly temperature controlled, i.e., salinity is not essential for its existence. Note that if the atmospheric forcing mechanism above describes the primary processes of the 50–70 year variability, we would expect variability in the MOC on both the (internal) 20–30 and the (forced) 50–70 year time scale.

A third possibility for the source of the 50–70 year variability is modulation of the 20–30 year variability by a tropical connection. Vellinga and Wu (2004) found that centennial fluctuations in the strength of the meridional overturning in HadCM3 were caused by processes in the tropics, with the period set by the travel time of salinity anomalies from their generation region near the equator to the convection region in the subpolar North Atlantic. This process, however, is on a time scale too long to cause variability on the 50–70 year time scale.

Hawkins and Sutton (2007) showed three-dimensional patterns of propagation of temperature and salinity anomalies in HadCM3 and found that salinity anomalies in the Arctic may also play an important role in the variability in that model, although in their case the variability was also on a centennial rather than multidecadal time scale.

This brings us to the final possible mechanism which arises through the interaction of the Atlantic with the Arctic. This appears to be a mechanism where salinity plays a crucial role. There is inflow of Atlantic water into the Arctic which is a source of multidecadal variability of sea-ice as shown by Polyakov et al. (2004). However, the signal quickly dissipates along the mean Arctic subsurface circulation. The strong and significant subsurface salinity variability in the Arctic (as found by the M-SSA analysis) hence indicates that the Arctic has internal variability on 50–70 year time scales. This variability may be associated with the Low Frequency Oscillation (LFO) as suggested by Polyakov et al. (2004) and possibly also to the Great Salinity Anomalies (GSAs). The LFO mechanism has an atmospheric component and requires feedback from the atmosphere to control the inflow of Atlantic water to the Arctic. This would entail variability in the atmosphere over the Arctic on the same time scale as the Arctic variability. An M-SSA analysis of sea level pressure over the Arctic does indeed find long period variability, but the only significant periods are between 30 and 50 years rather than 50–70 years. We must also consider that the major variability in the Arctic in this model is in salinity rather than temperature, and below rather than at the surface, so that variability in the Arctic atmosphere could very well be driven by something other than variability in the Arctic ocean. While the ocean-atmosphere mechanism of the LFO can not be discounted it appears more likely, in this model, that variability in the Arctic atmosphere is driven by SSTs in the North Atlantic, inheriting the time scale from there, while variability in the Arctic ocean could be generated internally and thus has its own time scale.

The involvement of the Arctic-Atlantic exchange is supported by GCM results where such a mechanism has been suggested to explain multidecadal variability. For example, Jungclaus et al. (2005) found that in the ECHAM5/MPI-OM model the overturning strength was affected by density anomalies generated in the Arctic and the subsequent oscillations had a period of 70-80 years. A similar mechanism was suggested by Delworth et al. (1997) to explain 40-80 year oscillations in the GFDL model. The Arctic exchange mechanism would be most visible at high latitudes and at the surface of the Atlantic ocean while one would not see strong subsurface signals which is consistent with the distinguishing properties of the 50–70 year variability discussed above. The role of the GSAs and subsequent changes in the Atlantic MOC is not clear: results on how the MOC changes due to salinity anomalies appear very model dependent with Zhang and Vallis (2006) finding a strong response, but Haak et al. (2003) hardly any.

6.5 SUMMARY AND CONCLUSIONS

In this paper an analysis of time scales and patterns of North Atlantic multidecadal variability was presented. Explaining this variability is a daunting task because of lack of data and a multitude of possible processes which may be involved and that may not be limited to the North Atlantic itself. The main result of this paper is that there are indications from both observations as well as GCM results for dominant variability on both 20–30 year and 50–70 year time scales.

The 20–30 year variability is clearly visible in midlatitude subsurface temperature fields both in observations and in GCM simulations. M-SSA analysis of the GFDL CM2.1 output shows that the spatial subsurface patterns in the North Atlantic display westward propagation, consistent with observations. As this propagation is a characteristic feature of the excited internal ocean mode mechanism, this mechanism is the best candidate to explain many of the features of the 20–30 year variability.

The simplest explanation for the longer period (50–70 year) variability is a modulation of the shorter period (20–30 year) variability. This would lead to both periods being visible in the spectrum of MOC variability, but would not explain why the longer period variability is most pronounced in high latitude SST anomaly fields, nor the depth dependence of the time scale of basin averaged temperature anomalies in the GFDL CM2.1 control simulation as shown in figure 6.7(c). M-SSA analysis of the GFDL CM2.1 model results suggests that the source of the 50–70 period variability is an oscillation seen in salinity at 400 m depth in the Arctic. Note that 400 m is the approximate depth of the layer of Atlantic water in the Arctic. While the Low Frequency Oscillation of Polyakov et al. (2004) is an attractive explanation for this variability we can find no firm basis for it in the GFDL model results. An alternative is that the inflow from the Atlantic may be exciting an internal salinity mode in the Arctic basin, which, in turn, feeds anomalies back into the North Atlantic on longer time scales. This then suggests that GSAs are coupled to the internal variability of the Arctic.

Finally, these results may start the discussion what one really calls the AMO. As research has developed, it would probably be better to reserve the term AMO for the longer 50–70 year variability while referring to the 20–30 year variability as the Atlantic Interdecadal Oscillation (AIO). In this case the AMO index needs to be redefined. Measurements of SST remain the most accessible method for constructing an index, but the domains may be altered. Restricting the domain, as in figure 6.3, to a narrower latitudinal band, 50°N to 60°N, for example, would suffice for an index for the interdecadal variability, while the multidecadal variability could be indexed by expanding the domain to include the Arctic. This would allow a distinction between the various time scales and patterns of variability.

ACKNOWLEDGEMENTS

The GCM data was obtained from the GFDL coupled climate models webpage (http://nomads.gfdl.noaa.gov/CM2.X/), the CET record from the Hadley Centre Central England Temperature dataset (http://hadobs.metoffice.com/hadcet/) and the Greenland ice-cores from the National Climatic Data Center/World Data Center for Paleoclimatology (http://www.ncdc.noaa.gov/paleo/icecore/).

7

INTERNAL MODES OF MULTIDECADAL VARIABILITY IN THE ARCTIC OCEAN

Observations of sea-ice extent and atmospheric temperature in the Arctic, although sparse, indicate variability on multidecadal time scales. Recent analyses of one of the IPCC-AR4 Global Climate Models (the GFDL CM2.1) have indicated that Arctic ocean variability on these time scales is associated with changes in basin-wide salinity patterns. In this paper we determine the internal modes of variability in an idealised Arctic basin by considering the stability of salinity driven flows. We find an internal ocean mode with a multidecadal time scale of which the spatial pattern is similar to that obtained in the analyses of the CM2.1 results. The physical mechanism explaining the spatial pattern of this mode and its propagation is presented.

This chapter is based on:
Internal modes of multidecadal variability in the Arctic Ocean, by L. M. Frankcombe and H. A. Dijkstra, *submitted to the Journal of Physical Oceanography*.

7.1 INTRODUCTION

Natural variability of the climate of the Arctic on decadal to multidecadal time scales is a topic which has recently begun to receive a great deal of attention. Anthropogenic climate change appears to be having its greatest effects in the Arctic, yet we have so far been unable to accurately predict the rate of the changes using state of the art climate models (Stroeve et al., 2007). The 2007 minimum in sea-ice extent, for example, was not adequately projected by any of the IPCC-AR4 models. This begs the question as to whether natural variability may be enhancing anthropogenically induced changes and if so, what mechanisms may be responsible.

The study of multidecadal variability in the North Atlantic also leads to questions about variability in the Arctic. Temperature and salinity anomalies from the North Atlantic may propagate into the Arctic and vice versa, connecting variability in the two basins. Long term observations in the Arctic region are limited, however there are indications of decadal to multidecadal variability in air pressure and temperature (Polyakov et al., 2003b), sea ice (Polyakov et al., 2003a) and temperature of Atlantic core water entering the Arctic (Polyakov et al., 2004). Multidecadal variability in century long records of sea-ice is found to be strongest in the Kara Sea, decaying towards the Canada Basin (Venegas and Mysak, 2000; Polyakov et al., 2003a). This multidecadal variability has been referred to as the Low Frequency Oscillation (LFO; Polyakov and Johnson, 2000). There are also multidecadal variations in sea-ice transport through Fram Strait associated with the variability of sea-ice extent (Vinje et al., 2002). In addition, there are the Great Salinity Anomalies (GSAs) in the North Atlantic, of which several are thought to be connected to large sea-ice exports out of the Arctic (Belkin et al., 1998).

Another connection between the North Atlantic and Arctic climate occurs through the atmosphere. The dominant atmospheric winter variability is associated with the pattern of the North Atlantic Oscillation (NAO), with its Arctic extension, the Northern Annular Mode (NAM; Thompson and Wallace, 2001). Although it cannot be demonstrated that the NAO has any significant preferential frequency, the Atlantic westerlies were relatively weak in the period between 1940 – 1970 and relatively strong from 1980 to present (Eden and Jung, 2001). NAO variations impose a well-known tri-polar sea surface temperature (SST) anomaly on the North Atlantic Ocean on seasonal to interannual time scales (Alvarez-Garcia et al., 2008), while a hemisphere wide response is associated with low frequency time scales (Visbeck et al., 2003).

In chapter 6 we found multidecadal variability in the North Atlantic on two time scales and proposed that the shorter 20 – 30 year time scale arises due to an ocean mode intrinsic to the North Atlantic basin (te Raa and Dijkstra, 2002), while the longer 50 – 70 year time scale is associated with Arctic variability. Based on observations and an analysis of a 500 year long control run of the GFDL CM2.1, we found that the source of the 50 – 70 period variability is an oscillation seen in salinity at 400 m depth in the Arctic. Note that 400 m is the approximate depth of the layer of Atlantic water in the Arctic. We suggested that the inflow from the Atlantic may be exciting an internal ocean mode in the Arctic basin, which, in turn, feeds buoyancy anomalies back into the North Atlantic on longer time scales. The salinity signatures of these anomalies may be related to GSAs, which would consequently be due to internal multidecadal variability of the Arctic.

In this chapter we take the first step towards determining salinity related internal mul-

tidecadal variability in the Arctic. The temperature related internal modes of variability in the North Atlantic were studied in Dijkstra (2006) by considering the linear stability of thermally driven three-dimensional ocean flows in an idealised single-hemispheric basin. Under zero forcing, it was shown that the normal modes of the motionless state are stationary. With increasing equator-to-pole temperature gradient, the growth rates of these modes are affected by the strength of the meridional overturning circulation and some of the stationary modes merge to become oscillatory modes which have multi-decadal periods under realistic forcing. Following the approach in Dijkstra (2006) we can immediately anticipate that if we consider salinity driven flow in an idealised Arctic basin, mergers of stationary modes may also occur. The issue, however, is whether they will have a multidecadal period and whether the patterns of these modes will correspond to those found in the GFDL CM2.1 results from chapter 6.

In section 7.2, the model and methodology used to determine the internal modes for a hierarchy of idealised Arctic Ocean models is presented. In section 7.3, results are presented for a circular basin with a polar island and it is shown that both westward and eastward propagating multidecadal modes exist. In section 7.4, we analyse the effects of geometry and idealised bottom topography on the modes. We summarise the results in section 7.5 and discuss them in the context of results of general circulation models and observations.

7.2 STABILITY OF ARCTIC OCEAN FLOWS

In the first subsection, we present the model used to address the internal variability in the Arctic, while in the second subsection we present the methodology by which internal modes of variability are computed.

7.2.1 OCEAN MODEL

We consider ocean flows in a model domain on the sphere bounded by the longitudes $\phi_w = 0^\circ$ and $\phi_e = 360^\circ$ and by the latitudes θ_s and θ_n (which will be specified later); the ocean basin has a mean depth D. The flows in this domain are forced by restoring surface boundary conditions (with a restoring time scale τ_S) to a salinity field S_R given by

$$S_R = S_0 + \Delta S f(\phi, \theta)$$

where ΔS is the amplitude of the salinity anomaly over the basin and $f(\phi, \theta)$ is a prescribed spatial pattern.

Salinity differences in the ocean cause density differences according to

$$\rho = \rho_0(1 + \alpha_S(S_* - S_0))$$

where α_S is the volumetric expansion coefficient, S_0 and ρ_0 are a reference salinity and density, respectively and S_* is the total salinity. The governing equations are the same as equations 2.8 and 2.9 with salinity in place of temperature.

Slip conditions and zero salt flux are assumed at the bottom boundary and, as the forcing is represented as a body force over the first layer, slip and zero salt flux conditions apply at the ocean surface. Hence, the boundary conditions at the top and bottom

2Ω	=	$1.4 \cdot 10^{-4}$	$[s^{-1}]$	r_0	=	$6.4 \cdot 10^{6}$	$[m]$
D	=	$4.0 \cdot 10^{3}$	$[m]$	τ_S	=	$7.5 \cdot 10^{1}$	$[days]$
α_S	=	$7.6 \cdot 10^{-4}$	$[K^{-1}]$	H_m	=	250	$[m]$
A_H	=	$1.6 \cdot 10^{5}$	$[m^2 s^{-1}]$	S_0	=	35.0	$[psu]$
ρ_0	=	$1.0 \cdot 10^{3}$	$[kgm^{-3}]$	A_V	=	$1.0 \cdot 10^{-3}$	$[m^2 s^{-1}]$
K_H	=	$1.0 \cdot 10^{3}$	$[m^2 s^{-1}]$	K_V	=	$2.3 \cdot 10^{-4}$	$[m^2 s^{-1}]$

TABLE 7.1: *Standard values of parameters used in the numerical calculations.*

boundaries are

$$z = -D, 0: \quad \frac{\partial u}{\partial z} = \frac{\partial v}{\partial z} = w = \frac{\partial S}{\partial z} = 0 \tag{7.1}$$

The lateral boundary conditions will be specified in each of the different cases below. The parameters for the standard case are the same as in typical large-scale low-resolution ocean general circulation models and their values are listed in table 7.1.

7.2.2 STEADY STATES AND THEIR STABILITY VERSUS ΔS

Using the model in the previous subsection, we will compute steady three-dimensional salinity driven flow solutions for different amplitudes of the surface salinity gradient ΔS and determine their linear stability.

First the steady governing equations (equations 2.8) and boundary conditions (equations 7.1) are discretised on an Arakawa B-grid using central spatial differences. On a $N \times M \times L$ grid with 5 unknowns per point (u, v, w, p and S), this leads to a system of $d = 5 \times N \times M \times L$ nonlinear algebraic equations. These are solved with ΔS as control parameter using a pseudo-arclength continuation method; details on this methodology are provided in Dijkstra (2005).

For each of the steady states, we now consider the evolution of infinitesimally small disturbances within the model. Linearising the equations 2.8 and 7.1 in the amplitude of the perturbations and separating the equations for these disturbances in time, an elliptic eigenvalue problem is obtained for the complex growth factor σ of each perturbation. When this elliptic eigenvalue problem is discretised, a generalised eigenvalue problem is obtained of the form

$$\mathcal{A}\mathbf{x} = \sigma \mathcal{B}\mathbf{x} \tag{7.2}$$

where $\mathcal{A}$ and $\mathcal{B}$ are $d \times d$ matrices. We solve for the 12 'most dangerous' modes, i.e., those with real part closest to the imaginary axis, using the Jacobi-Davidson QZ method (Sleijpen and van der Vorst, 1996) and order the eigenvalues $\sigma = \sigma_r + i\sigma_i$ according to the magnitude of their real part (the growth factor). For each eigenvalue σ, there is a corresponding eigenvector $\mathbf{x} = \mathbf{x}_r + i\mathbf{x}_i$ according to equation 7.2. Oscillatory modes appear as complex conjugate pairs of eigenvalues and the time-dependence of these oscillatory modes can be represented by the function

$$\Phi(t) = e^{\sigma_r t}(\mathbf{x}_r \cos \sigma_i t - \mathbf{x}_i \sin \sigma_i t)$$

Propagation of the pattern can therefore be determined by plotting $\mathbf{x}_r$ (which represent the spatial pattern of the mode at $t = 0$) and $\mathbf{x}_i$ (which represent the spatial pattern of the mode at $t = -\pi/2$).

7.3 CIRCULAR BASIN WITH A POLAR ISLAND

To illustrate the methodology as described above we will start with the idealised case of a circular basin with a polar island with $\theta_s = 70°$N and $\theta_n = 87.5°$N. No-slip and zero salt flux conditions are applied along the northern and southern boundaries, periodic conditions apply along the eastern and western boundaries. We use a 90×16 grid over the ocean region and there are 16 evenly spaced levels in the vertical.

7.3.1 STATIONARY SALINITY MODES

For the zero forcing case ($\Delta S = 0$) the flow is motionless ($(u, v, w) = 0$) and the salinity field is determined by the equation:

$$\frac{\partial S}{\partial t} = \frac{K_H}{r_0^2 \cos\theta}\left[\frac{\partial}{\partial\phi}\left(\frac{1}{\cos\theta}\frac{\partial S}{\partial\phi}\right) + \frac{\partial}{\partial\theta}\left(\cos\theta\frac{\partial S}{\partial\theta}\right)\right] + K_V\frac{\partial^2 S}{\partial z^2} \tag{7.3}$$

with boundary conditions

$$\begin{aligned} z = -D, 0 \quad &: \quad \frac{\partial S}{\partial z} = 0 \\ \theta = \theta_s, \theta_n \quad &: \quad \frac{\partial S}{\partial\theta} = 0 \end{aligned}$$

and we apply periodic boundary conditions in the ϕ direction, i.e.,

$$S(0,\theta,z) = S(2\pi,\theta,z)\ ;\ \frac{\partial S}{\partial\phi}(0,\theta,z) = \frac{\partial S}{\partial\phi}(2\pi,\theta,z)$$

The general solution can be found by separation of variables:

$$S(\phi,\theta,z,t) = \Phi(\phi)\Theta(\theta)Z(z)e^{\sigma t}$$

and as the problem is homogeneous, it has only nontrivial solutions for specific values of σ. The eigenvalue problem can be reduced to that of a one-point boundary eigenvalue problem, as is shown in the Appendix. Although this problem can be solved analytically in terms of Legendre functions, we have chosen to solve it numerically (again details are provided in the Appendix). For this case, it turns out that all the eigenvalues σ are real and hence the internal modes are stationary. We can label the internal modes according to the indices (n, m, l) where each index indicates the number of zeros of the eigenfunction in the domain; n representing zeros in the zonal direction, m in the meridional direction and l the number of zeros with depth.

In table 7.2, results for the growth rates of the (n, m, l) modes are provided for two values of K_V. For $K_V = 2.3 \times 10^{-4}$ m^{2}s^{-1}, the middle column provides the growth factors as computed numerically from the two-point boundary eigenvalue problem as

			$K_v = 2.3 \times 10^{-4}$			$K_v = 1.0 \times 10^{-4}$
n	m	l	90°N (analytic)	87.5°N (analytic)	87.5°N (model)	87.5°N (analytic)
0	0	1	-4.4742$\times 10^{-3}$	-4.4742$\times 10^{-3}$	-4.5043$\times 10^{-3}$	-1.9453$\times 10^{-3}$
0	0	2	-1.7897$\times 10^{-2}$	-1.7897$\times 10^{-2}$	-1.7843$\times 10^{-2}$	-7.7812$\times 10^{-3}$
1	0	0	-2.1708$\times 10^{-2}$	-2.0161$\times 10^{-2}$	-2.0814$\times 10^{-2}$	-2.0161$\times 10^{-2}$
1	0	1	-2.6182$\times 10^{-2}$	-2.4635$\times 10^{-2}$	-2.5319$\times 10^{-2}$	-2.2106$\times 10^{-2}$
1	0	2	-3.9605$\times 10^{-2}$	-3.8058$\times 10^{-2}$	-3.8658$\times 10^{-2}$	-2.7942$\times 10^{-2}$
0	0	3	-4.0268$\times 10^{-2}$	-4.0268$\times 10^{-2}$	-3.9506$\times 10^{-2}$	-1.7508$\times 10^{-2}$
2	0	0	-6.0332$\times 10^{-2}$	-6.0111$\times 10^{-2}$	-6.1145$\times 10^{-2}$	-6.0111$\times 10^{-2}$
1	0	3	-6.1976$\times 10^{-2}$	-6.0429$\times 10^{-2}$	-6.0321$\times 10^{-2}$	-3.7669$\times 10^{-2}$

TABLE 7.2: *Growth rates (in yr^{-1}) of the least damped modes for different values of K_V (in m^2/s) and θ_n.*

in the Appendix. The third column shows the values as directly computed by solving the eigenvalue problem (equation 7.2) from the discretised model in section 7.2.1. The agreement of both values provides a check on the eigenvalue computation through equation 7.2. We find that the growth factor of the modes depends slightly on the size of the polar island (compare the $\theta_n = 87.5°$N and $\theta_n = 90.0°$N results). In addition, the growth rates are also dependent on the value of K_V, for example when K_V is decreased from 2.3×10^{-4} m^2/s to 1.0×10^{-4} m^2/s the (0,0,3) mode switches from being the sixth to the third least damped mode.

Spatial patterns for the eight least damped modes are shown in figure 7.1 for the case where $\theta_n = 87.5°$N and $K_V = 2.3 \times 10^{-4}$ m^2/s. Note that the amplitudes of the patterns are arbitrary. The patterns do not change as θ_n and K_V vary. The two least damped modes, (0,0,1) and (0,0,2), have exactly the same growth rates as in the North Atlantic basin used in the normal mode calculations of Dijkstra (2006), and these are also independent of the size of the polar island. This is because the growth rates for the $n = 0, m = 0$ modes only depend on the vertical diffusion time scales. Modes with $m = 1, 2, \ldots$ have very negative growth rates (i.e. they are highly damped).

7.3.2 MODE MERGING DUE TO NON-ZERO FORCING

To study the emergence of oscillatory modes, an idealised salinity pattern is applied as the surface boundary condition. Salinity is restored to a sinusoidal profile with amplitude ΔS, i.e.

$$f(\phi, \theta) = -\cos \pi \frac{\theta - \theta_s}{\theta_n - \theta_s}$$

with saline water near the polar island and fresher waters along the outer edge of the basin. This causes an anticlockwise (eastwards) circulation pattern to develop. Starting

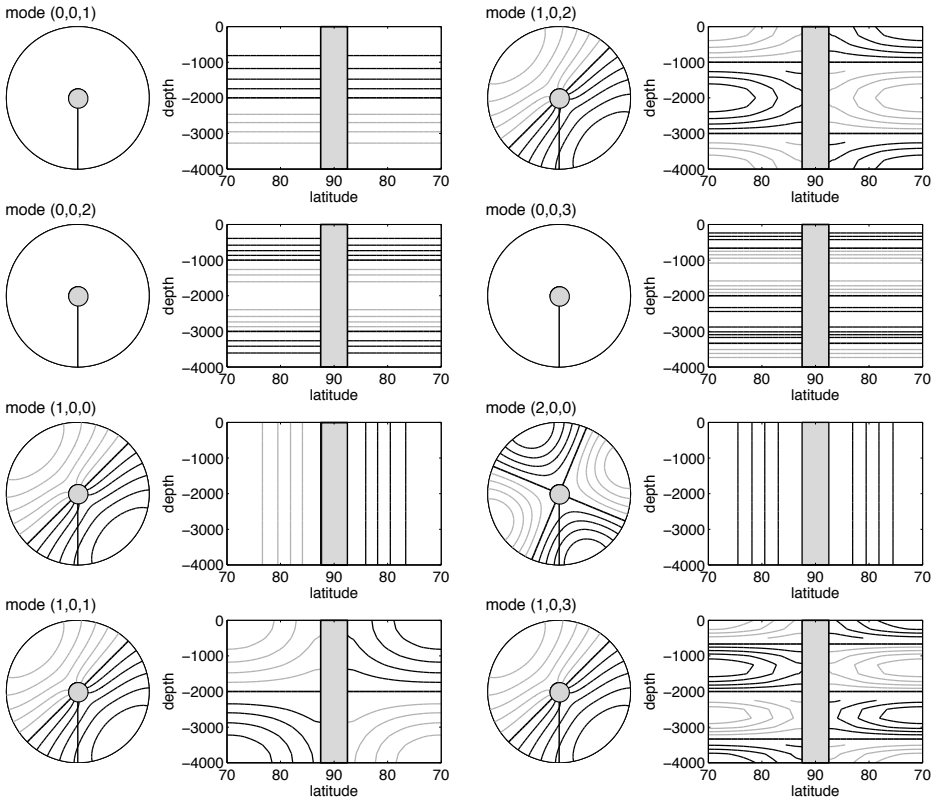

FIGURE 7.1: *Spatial salinity pattern at the surface (left) and in a vertical section (right) of the eight least damped modes. Land is shaded grey, negative contours are plotted in grey, the zero contour is bold. The amplitude of the modes is arbitrary.*

from $\Delta S = 0$ we increase the amplitude of the forcing (and thus the strength of the background circulation) and determine steady circulation states versus ΔS. We then diagnose the freshwater flux which is needed to maintain this steady state and determine the linear stability of the steady state under prescribed flux conditions. This procedure is similar to that in Dijkstra (2006).

Figure 7.2(a) shows how the growth rates of four of the modes that appear in the circular basin change with increasing strength of the forcing. All the modes have a negative growth rate, indicating that the steady equilibrium solution is stable. The various (0,0,l) modes have growth rates that are almost constant as forcing increases (after an initial adjustment) while the other modes show a strong dependence of growth rate on forcing strength. Due to the circular symmetry of the basin there are two copies of each stationary (1,0,l) mode, each having the same spatial pattern under a rotation, i.e. the corresponding real eigenvalue has an algebraic multiplicity 2. The two copies of each mode merge for very small values of ΔS, giving rise to an oscillatory mode. The periods of two of these oscillatory modes are plotted in figure 7.2(b).

The mode with the shortest period as ΔS increases is the (1,0,2) mode. The propa-

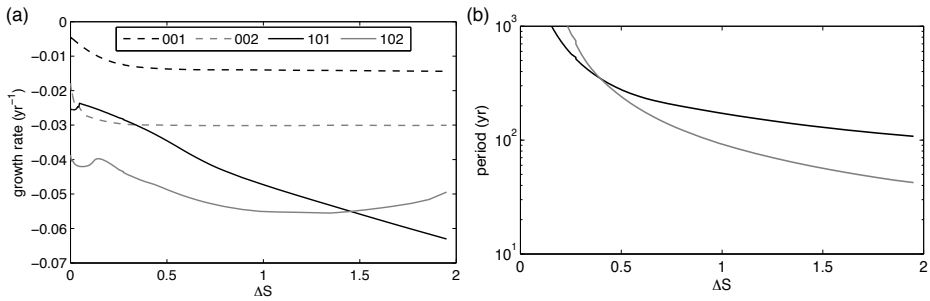

FIGURE 7.2: *(a) Growth rate and (b) period of four of the modes as forcing ΔS increases.*

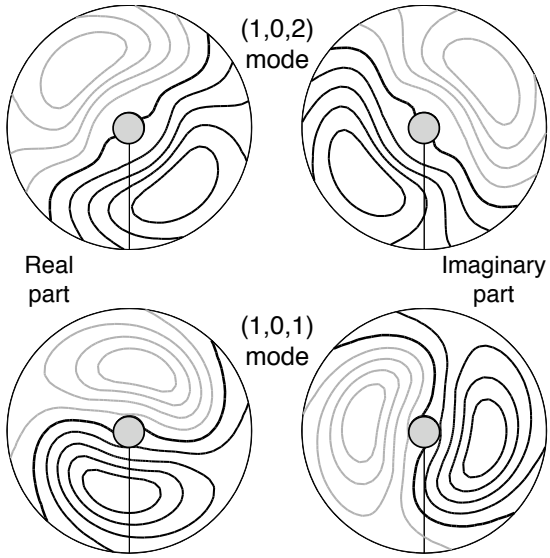

FIGURE 7.3: *Real and imaginary parts of the oscillatory (1,0,2) mode (a) and (1,0,1) mode (b) for $\Delta S = 1.62$. Format as in figure 7.1.*

gation of the mode can be visualised using the real and imaginary parts, shown in figure 7.3(a). The imaginary part is the pattern at time $t = -\pi/2$ and the real part is the pattern at time $t = 0$. The anomalies move anti-clockwise (cyclonically, eastwards around the pole), in the same direction as the background flow. The mode with the second shortest period is the (1,0,1) mode. It propagates clockwise (anti-cyclonically, westwards around the pole) against the background flow, the real and imaginary parts are shown in figure 7.3(b). As explained in te Raa and Dijkstra (2002), the phase speed of these modes is related to the background north-south salinity gradient and the background zonal flow. In the case of the (1,0,2) mode (the (1,0,1) mode), the background flow velocity is larger (smaller) than the intrinsic westward propagation velocity due to the background salinity gradient, leading to an eastward (westward) propagating salinity anomaly pattern.

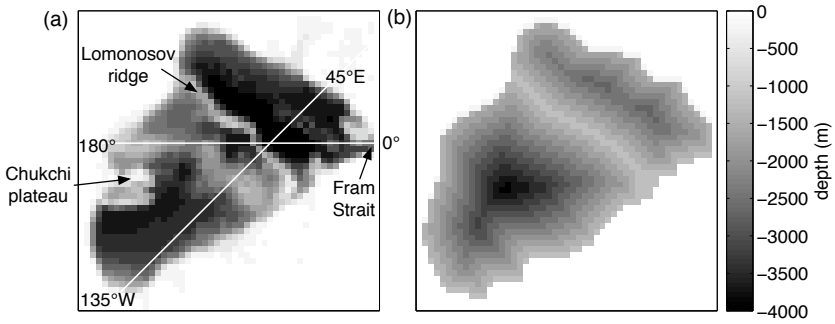

FIGURE 7.4: *Map showing (a) real bathymetry of the Arctic basin and (b) idealised bathymetry with a ridge. The white lines indicate the sections used in figure 7.13.*

7.4 ARCTIC BASIN

We now apply the ideas from the previous section to more realistic Arctic Ocean basin configurations. The topography of the Arctic basin is shown in figure 7.4(a). There are shallow seas around much of the Arctic and these are closed in the model topography. To avoid the problems associated with the convergence of the grid at the poles the Earth's rotation vector is rotated so that it is at the equator. The Arctic basin is then also positioned at the equator. This is equivalent to rotating the grid so that the poles of the grid are at the equator, however the implementation is simpler since only the Coriolis parameter has to be changed, from $2\Omega \sin\theta$ to $2\Omega \cos\theta \cos\phi$. We use a 51×51 grid over the Arctic basin, which gives a resolution of approximately 60 km in the horizontal. Again, there are 16 evenly spaced vertical layers, each is 250 m thick.

7.4.1 BASIN GEOMETRY

First we only consider the effect of the basin geometry on the stability of the salinity driven flows and study the case of a flat bottom. For $\Delta S = 0$, the growth factors of the salinity modes are listed in table 7.3. For simplicity, n is the number of zeros in the long axis of the basin (i.e. along the 135°W – 45°E line in figure 7.4(a)), m is the number of zeros in the short axis (i.e. rotating the basin by 45°) and l is the number of zeros with depth, as before. These modes, for which the salinity patterns are shown in figure 7.5, can be compared to the kind of modes seen the circular basin. Once again the least damped modes are the (0,0,1) and (0,0,2) modes, followed by the (1,0,0) mode. The (0,m,0) modes are also strongly damped in this case, as in the circular basin. Note that, because there is no longer any circular symmetry, the algebraic multiplicity of each of the modes is now equal to one.

We again apply a simplified surface salinity forcing, of which the pattern of $f(\phi, \theta)$ is shown in figure 7.6(a). Here the regions nearest to the Atlantic inflow area are saltier. ΔS once again represents the amplitude of the forcing, i.e. the difference between the saltiest water at the Atlantic inflow region and the freshest water on the opposite side of the basin. This salinity forcing pattern results in a surface circulation pattern shown in figure 7.6(b). While this circulation does not represent the Arctic Circumboundary

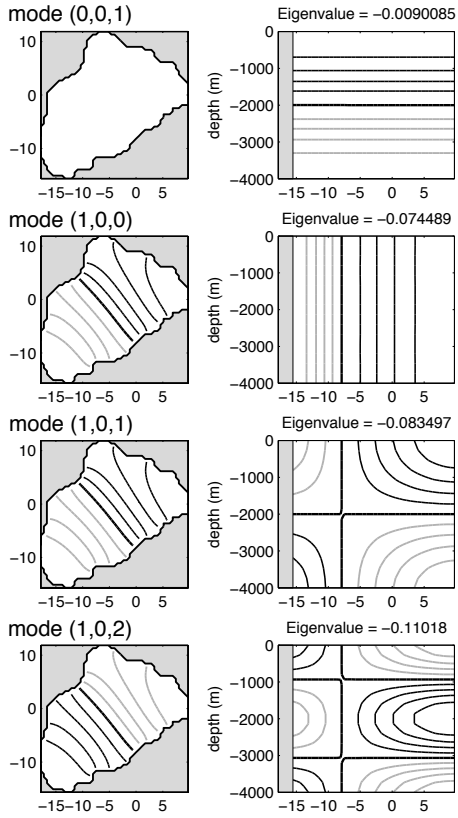

FIGURE 7.5: *Spatial salinity pattern at the surface (left) and in a vertical section (right) of the first, third, fifth and sixth least damped modes in the flat bottomed Arctic basin under zero forcing. Format as in figure 7.1.*

Current, it mimics the anti-cyclonic circulation in the internal of the Arctic basin (Nøst and Isachsen, 2003), making it adequate for a first estimate of the internal modes.

As the forcing strength (ΔS) is increased oscillatory modes once again appear, of which one has a period in the multidecadal range. This oscillatory mode is created through the merging of two different stationary modes, the (1,0,1) mode and the (1,0,2) mode. The real and imaginary parts of the eigenvalues of these two modes are shown in figure 7.7. Both modes are stationary for small ΔS, thus the imaginary part of their eigenvalues are zero (figure 7.7(b)). For very small values of ΔS the eigenvalues of the modes are difficult to follow, in fact for some steps the model could not find the modes at all, leading to gaps in the curves in figure 7.7. However once the modes were reacquired by the model they are recognisable by their spatial patterns as the (1,0,1) and (1,0,2) modes.

As the two modes merge the imaginary parts of their eigenvalues become non-zero and the real parts of their eigenvalues become identical. That is, their eigenvalues are of the form $\sigma_r \pm i\sigma_i$. This is the same type of merger that occurs in modes as studied in Dijkstra (2006). The pattern of propagation is shown in figure 7.8, where we can

n	m	l	growth rate
0	0	1	-4.5042$\times 10^{-3}$
0	0	2	-1.7844$\times 10^{-2}$
1	0	0	-3.7244$\times 10^{-2}$
0	0	3	-3.9506$\times 10^{-2}$
1	0	1	-4.1749$\times 10^{-2}$
1	0	2	-5.5089$\times 10^{-2}$
0	0	4	-6.8659$\times 10^{-2}$
1	0	3	-7.6751$\times 10^{-2}$

TABLE 7.3: *Growth rates (in yr^{-1}) of the least damped modes for the flat bottomed Arctic basin.*

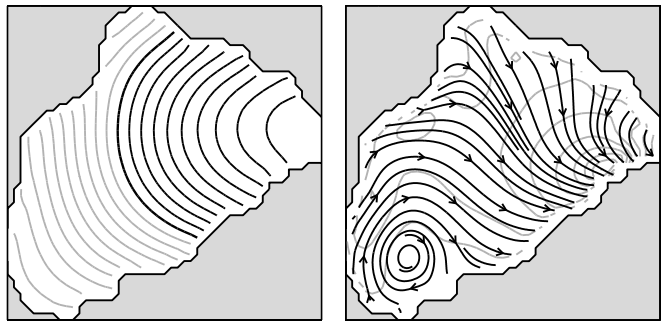

FIGURE 7.6: *(a) Surface salinity forcing with negative contours in grey and (b) resulting surface circulation with streamlines (black with arrows) and speed contours (grey). Surface speeds reach a maximum of just under 20 cm/s for $\Delta S = 1$.*

see that anomalies develop in the Canada basin and propagate across the pole towards the Atlantic inflow region. The period of this mode is in the multidecadal range and its dependence on the forcing strength ΔS is plotted in figure 7.12.

7.4.2 BOTTOM TOPOGRAPHY

Circulation in the Arctic is greatly influenced by the large ridges that stretch across the basin, and the pattern and propagation of internal modes depends on the background circulation. Intricate topography is not possible in the model, but we make an approximation of the Lomonosov ridge as shown in figure 7.4(b).

Figure 7.9 shows that the stationary modes that appear under zero forcing ($\Delta S = 0$) in this case differ from the modes seen in the previous two cases. The two least damped modes, for example, are a kind of (0,0,1) mode where the negative anomaly at depth is found on one side of the ridge or the other. Similarly, the patterns for many of the more damped modes are not as easily classified as in the flat bottomed Arctic case as some of

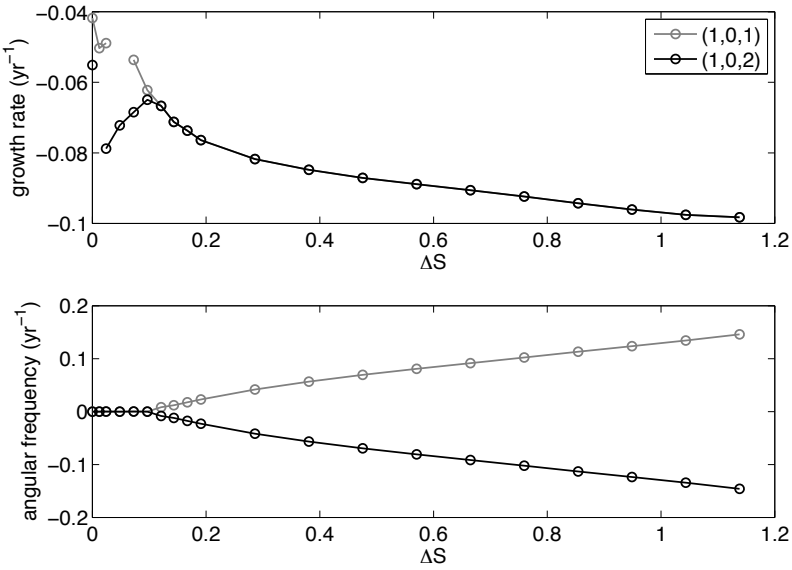

FIGURE 7.7: *(a) Growth rate and (b) angular frequency of the (1,0,1) and (1,0,2) modes as the amplitude of the forcing ΔS increases. The merger of the two modes creates an oscillatory mode.*

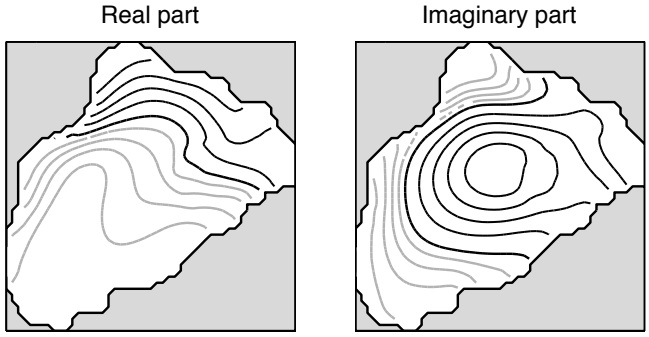

FIGURE 7.8: *Real and imaginary part of the oscillatory mode with the shortest period for the flat bottomed Arctic basin for $\Delta S = 1.14$. Format as in figure 7.1.*

them appear to have different (n, m, l) patterns in each of the two sub-basins.

The same surface salinity forcing pattern (figure 7.6) is used as in the flat bottomed Arctic case, with salty water near the Atlantic inflow region. The resulting steady surface circulation for $\Delta S = 1$ is shown in figure 7.10. Comparing this pattern to the circulation pattern in the case with no bottom topography (figure 7.6(b)) we can see that the ridge causes circulation in the basin to be separated into two parts, one on either side of the ridge, as is the case for the real Arctic ocean. However to make the model circulation resemble circulation in the real Arctic more closely would require intricate bottom topography (and also a representation of Atlantic inflow), in which case find-

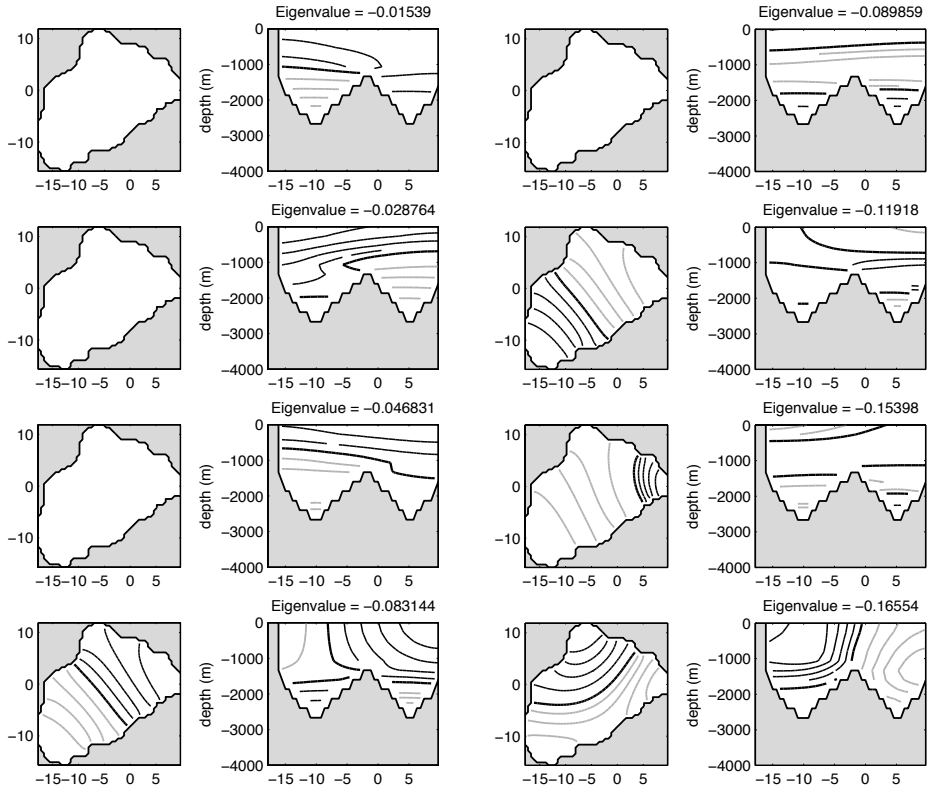

FIGURE 7.9: *Spatial salinity pattern at the surface (left) and in a vertical section (right) of the eight least damped modes under zero forcing in the Arctic basin with a ridge. Format as in figure 7.1.*

FIGURE 7.10: *Surface circulation for the Arctic basin with a ridge. Streamlines are shown in black, grey contours indicate velocity. Surface velocities reach a maximum of about 10 cm/s for* $\Delta S = 1$.

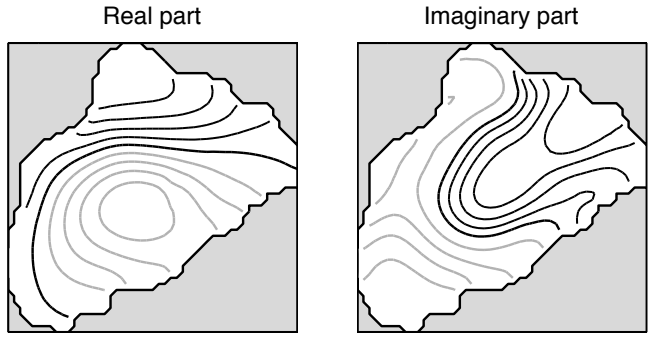

FIGURE 7.11: *Real and imaginary part of the least damped oscillatory mode in the Arctic basin with a ridge for $\Delta S = 0.75$. Format as in figure 7.1.*

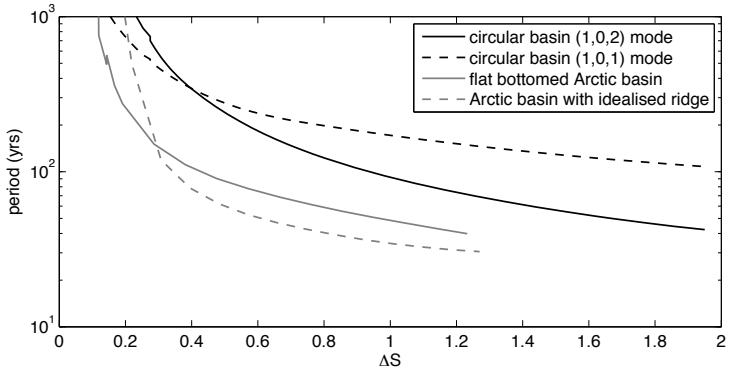

FIGURE 7.12: *Periods of the oscillatory modes versus ΔS for the different cases considered.*

ing solutions with the pseudo-arclength continuation method becomes difficult. We are therefore restricted to simplified versions of the topography (and no Atlantic inflow).

As in the flat bottomed case there is one oscillatory mode with a multidecadal period. The spatial pattern and period of this mode are similar to the flat bottomed case. The real and imaginary parts of the mode are plotted in figure 7.11 and the dependence of the period on ΔS is plotted in figure 7.12. The main difference in the spatial pattern is that the salinity anomalies do not penetrate so strongly towards the Atlantic side of the ridge, showing that the idealised ridge is blocking the propagation of the mode.

The spatial pattern of the oscillatory modes depends on the background circulation. Circulation in the real Arctic is largely controlled by bathymetry, whereas in the model Arctic it depends more on the surface forcing (which is unrealistic). An attempt to make the model circulation appear more like the real one (by making three peaks in salinity forcing to mimic the circulation in the three main Arctic basins) resulted in an oscillatory mode with a time scale very similar to those already shown here. The spatial pattern was deformed by the surface forcing but the mode still propagated in the same way as in the two cases shown above. This shows that the multidecadal oscillatory mode is reasonably robust in the model Arctic.

7.4.3 COMPARISON WITH THE CM2.1 MSSA MODE

The exact time scale of the oscillatory modes found in the idealised model depends on the amplitude of the surface forcing (figure 7.12) and also on the values of mixing coefficients, in particular K_V (te Raa and Dijkstra, 2002; Huck et al., 2001), however it remains in the multidecadal range. The spatial patterns of the modes do not change much with small variations in these parameters. Instead of precisely tuning the periods of the oscillatory modes here to the time scale of the oscillatory MSSA mode in the GFDL CM2.1 model as found in chapter 6, we compare the spatial pattern of the modes over one oscillation period.

Figure 7.13 shows Hovmöller plots along the two longitudinal sections marked with the white lines in figure 7.4(a): (1) along 180° through the pole then along 0° (parallel to the model grid) and (2) along 135°W through the pole then along 45°E (approximately along the long axis of the basin). From these Hovmöller plots we can see some similarities between the spatial patterns. Firstly, comparing the patterns from the simple model with and without a ridge we can see that the presence of the ridge effects the propagation of the anomalies towards the Atlantic side of the basin. Secondly, if we compare the pattern from the coupled model with the patterns from the simple model along the 180° – 0° line we see the same general pattern of propagation.

However, there are also some discrepancies between the spatial patterns of both modes, which becomes clear when looking along the 135°W – 45°E line. In the GFDL CM2.1 model the anomaly propagates southwards away from the pole (in both directions) but in the simple model it propagates from the Canada basin over the pole towards the Atlantic inflow region. This difference can be attributed to the absence of the Chukchi plateau in the simple model. In the GFDL CM2.1 model the pattern appears to propagate from close to the Chukchi plateau towards the pole with anomalies then spreading southwards through the Canada basin. In the simple model the anomalies propagate from the Canada basin itself. More sophisticated bathymetry would have to be implemented in the model to investigate how the presence of the Chukchi plateau as well as the shallow seas along the Russian shelf would affect the spatial pattern of the mode.

7.5 SUMMARY AND DISCUSSION

In this paper, we have investigated the internal modes of variability of salinity driven flows in idealised Arctic basins. These modes can be determined by solving the linear stability problem of a particular salinity driven steady state under prescribed flux conditions. As a control parameter, we have used the parameter ΔS, the amplitude of the salinity forcing.

For $\Delta S = 0$ the modes are stationary (real eigenvalue) in all configurations investigated. The easiest modes to understand are those on the circular basin with a polar island. These are the solutions to the anisotropic Laplace equation on a near-polar circular sector and their meridional structure is given by Legendre functions (see Appendix). The different modes for this case can still be recognised for the flat bottom Arctic basin and also in the case with bottom topography, where the spatial structures of each mode are deformed by the presence of topography.

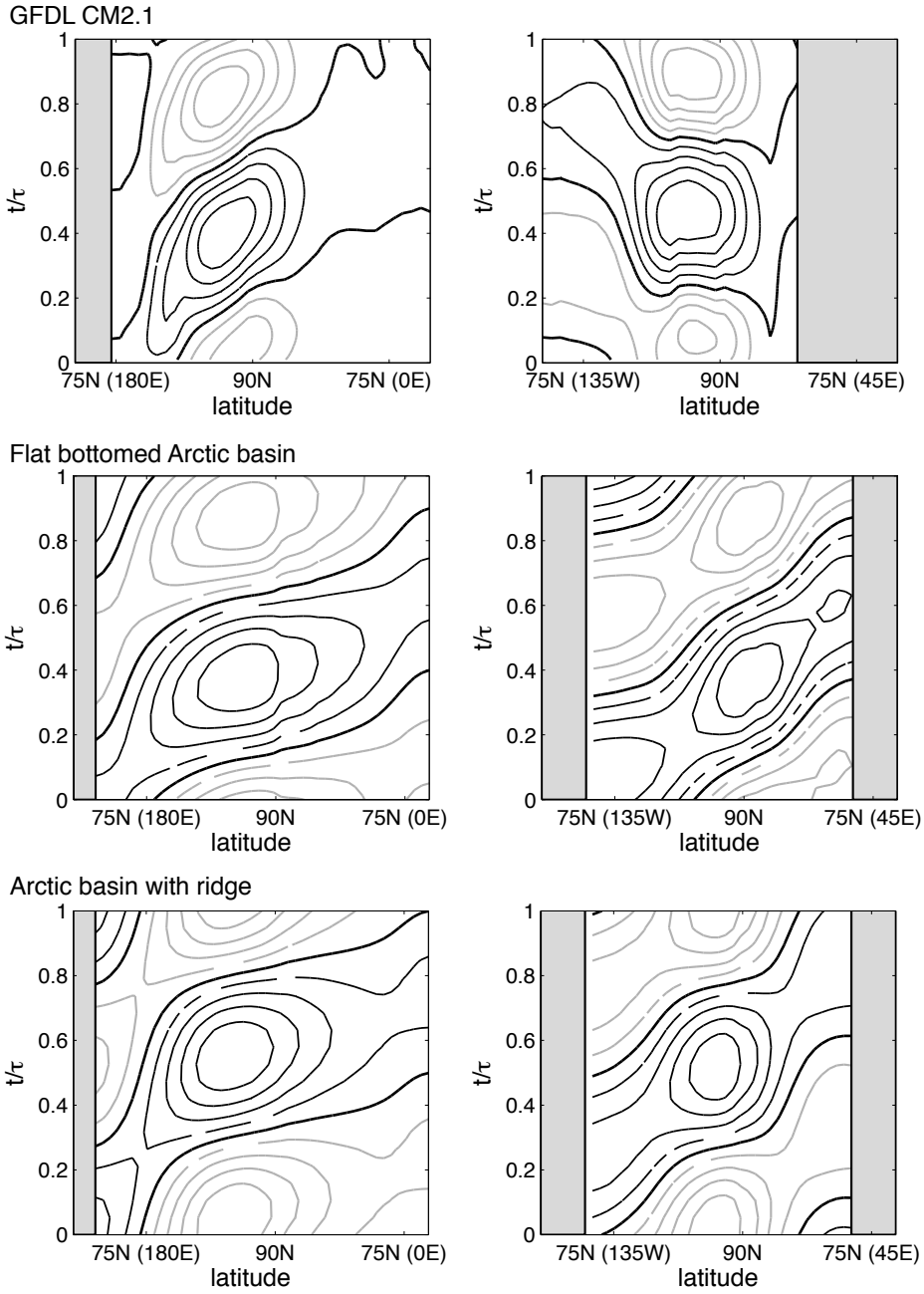

FIGURE 7.13: *Hovmöller plots of the propagation of the salinity anomaly normalised by the period τ across two longitudinal sections from the GFDL CM2.1 coupled model ($\tau \approx 100$ yrs; upper), the oscillatory mode of the flat bottomed Arctic basin (from figure 7.8, $\tau \approx 43$ yrs; middle) and that for the Arctic basin with a ridge (from figure 7.11, $\tau \approx 42$ yrs; lower). The longitudinal sections (shown in figure 7.4) are along $180^\circ - 0^\circ$ (left) and $135^\circ W - 45^\circ E$ (right).*

When the forcing (ΔS) is increased, many of the modes remain stationary and damped (i.e. negative, real eigenvalues). However, merging occurs for some modes, which leads to oscillatory modes (non-zero imaginary parts). The periods of these modes eventually reach multidecadal values under a reasonable salinity contrast over the basin. The mechanism of propagation here is the 'saline' Rossby wave which is induced by the background gradient in salinity, analogous to the 'thermal' Rossby waves discussed in Dijkstra (2006). The modes intrinsically propagate westwards (just like ordinary Rossby waves) but they can be arrested by the eastward background flow; eastwards propagating anomalies are therefore also possible. This is illustrated by the eastwards propagating (1,0,2) mode and the westwards propagating (1,0,1) mode in the circular basin (figure 7.3). It seems that oscillatory modes with multidecadal periods are a robust feature of our model Arctic. Under the most realistic configuration considered here, and taking into account the simplified bathymetry in our model, the pattern of the least damped oscillatory mode tends to look like the MSSA mode of multidecadal variability which was found in the GFDL CM2.1 model in chapter 6.

The growth factor for all modes found is negative, hence for the modes to be observable they would have to be excited. Growth rates depend strongly on the background circulation since modes can only grow if the salinity anomalies transported by the circulation lead to circulation anomalies which reinforce the original salinity anomalies. Since the background circulation in our idealised Arctic is not realistic we cannot expect to have realistic growth rates.

Now, as we have no thermal and momentum forcing in the model, as well as no parametrisation for sea-ice, the patterns of the modes should be interpreted as occurring below the Arctic halocline. This is consistent with the appearance of the mode from the GFDL CM2.1 model, which was found below the halocline in that model. It was shown in chapter 3 that damped oscillatory modes can be excited by the inclusion of noise in the system. The most plausible mechanism of the excitation of the internal modes in this kind of situation is variability in the inflow of Atlantic water. Once excited, the internal variability would cause circulation changes in the Arctic, altering heat and freshwater storage.

The model Arctic considered in this paper is highly idealised. Improvements on this model would be necessary in order to make a closer comparison with the results from the GFDL CM2.1 model. In addition, in order to study the exchange between the Arctic and the North Atlantic, the next step would be to make a model coupling the two basins. This would allow us to study the influence of the internal oscillations found in the North Atlantic on the Arctic, and vice versa.

7.6 APPENDIX: ANALYTICAL SOLUTION

For the case of a circular basin with a polar island, the general solution to equation 7.3 can be found by separation of variables:

$$S(\phi, \theta, z, t) = \Phi(\phi)\Theta(\theta)Z(z)\Gamma(t)$$

leading to four problems:

$$\frac{\Phi''}{\Phi} = -\mu^2 \tag{7.4a}$$

$$\Theta'' \cos\theta = \Theta' \sin\theta - \Theta\left(\chi \cos\theta - \frac{\mu^2}{\cos\theta}\right) \tag{7.4b}$$

$$\frac{Z''}{Z} = (\chi + \lambda)\frac{K_H}{K_V r_0^2} \tag{7.4c}$$

$$\frac{\Gamma'}{\Gamma} = \lambda \frac{K_H}{r_0^2} \tag{7.4d}$$

where μ, χ and λ are separation constants. The boundary conditions become:

$$Z'(-D) = Z'(0) = 0 \tag{7.5a}$$

$$\Theta'(\theta_s) = \Theta'(\theta_n) = 0 \tag{7.5b}$$

The solutions to equations 7.4a and 7.4c are sinusoids while the solution to equation 7.4d is an exponential. Using the boundary conditions we can solve for the separation constants:

$$\begin{aligned} \mu &= 0, 1, 2, \ldots \\ -(\chi + \lambda) &= (l\pi)^2 \frac{K_V r_0^2}{K_H D^2}, \quad l = 0, 1, 2, \ldots \end{aligned}$$

So our solutions to equations 7.4a and 7.4c and (7.4d) are:

$$\begin{aligned} \Phi &= C_1 \sin(\mu\phi) + C_2 \cos(\mu\phi), \qquad \mu = 0, 1, 2, \ldots \\ Z &= C_3 \cos(\frac{\pi l}{D} z), \qquad l = 0, 1, 2, \ldots \\ \Gamma &= C_4 \, e^{\frac{\lambda K_H}{r_0^2} t} \end{aligned}$$

where C_1-C_4 are constants.

The solution to equation 7.4b may be found by substituting $x = \sin\theta$ into the equation, which then becomes:

$$\Theta''(1 - x^2) - 2x\Theta' + \Theta(\chi - \frac{\mu^2}{1 - x^2}) = 0$$

Introducing $\chi = \nu(\nu + 1)$, this equation reduces to the standard form of the Legendre equation. Instead of solving this equation analytically, we solve equation 7.4b by discretising the equation with boundary conditions 7.5b on a one-dimensional grid with $M = 16$ points and solving the resulting algebraic eigenvalue problem numerically using a standard library (NAG) routine.

CONCLUSIONS AND OUTLOOK

In this thesis we have examined the variability in the North Atlantic ocean on decadal to multidecadal time scales in terms of dynamical systems theory. Using this theory the AMO is viewed as an oscillatory normal mode to which the background state (i.e. the MOC) becomes unstable under certain conditions.

The simplest system in which the AMO mode can be found (the so-called 'minimal model') is a three-dimensional ocean-only single basin model of the North Atlantic, forced only with a temperature boundary condition at the surface. The presence of an overturning cell with sinking in the north of the basin is essential, i.e. similar variability does not appear in the North Pacific. Salinity and wind forcing are, however, not necessary for the existence of the mode. Neither is bathymetry, however the inclusion of continental boundaries in the minimal model is required to deform the spatial pattern of the mode so that there is a remarkable correspondence between the pattern of SST anomalies observed in the North Atlantic and those obtained from the minimal model.

Extensions of the minimal model to include salinity, wind forcing, continents, bathymetry and other geometries (including double hemisphere and double basin configurations) have previously been investigated. One element that still remained was the effect of atmospheric damping and noise, and this was the subject of chapter 3. The AMO mode in the minimal model is damped (i.e. the mode has a negative growth rate) under restoring boundary conditions, which corresponds to large atmospheric damping, and the growth rate of the mode increases as the damping is decreased. The growth rate crosses zero at the critical value of the damping parameter and the oscillation is thereafter excited. The mode thus arises through a Hopf bifurcation with the strength of the damping as the control parameter. This may explain why AMO behaviour varies so greatly between GCMs since it depends on the growth rate of the mode in a particular model.

It is also possible to excite the mode in a regime where the growth rate is negative (i.e. below the critical value) by adding noise to the system. The variability that then appears includes the spatial pattern and time scale of the mode as it would appear if the system was above the critical point. This is known as a stochastic Hopf bifurcation, a simple example of which is given in chapter 2. The idea is applied to the minimal model in chapter 3 where it is found that spatial and temporal patterns in the noise can be effective at exciting the AMO mode to higher amplitudes. This translates to the real

ocean as the AMO mode being a damped internal ocean mode which can be efficiently excited by patterns of atmospheric variability such as the NAO.

We have already noted that the observed pattern of SST anomalies associated with the AMO bears a strong resemblance to the pattern from the minimal model, which gives confidence that the mechanism derived from the simple model (involving an out of phase relationship between meridional and zonal overturning) may indeed be responsible for the observed AMO. However, this mechanism is not the only one which has been proposed as a cause for the AMO. To validate the mechanism we require further comparisons with observations.

One important phenomenon associated with the minimal model mechanism is the westward propagation of temperature anomalies in the surface ocean. This propagation is not expected to be found in SST observations since in the real ocean it is disturbed by atmospheric noise and the presence of the strong, eastwards flowing Gulf Stream. However it is observed in temperature measurements taken below the surface, as shown in chapter 4. Although no firm conclusions about the time scale can be drawn due to the limited length of the observational record, it does appear that the variability occurs on a time scale closer to 20-30 years than to 50-70 years which is the period more usually associated with the AMO.

The variability of temperature causes variability in sea surface height. Variations in SSH observed by tide gauges around the North Atlantic are discussed in chapter 5. Tide gauges on the North American and European sides of the North Atlantic both show coherent variability along the coast. The link between SSH and the AMO is made using results from the GFDL CM2.1 GCM which shows AMO-like variability in the North Atlantic on 20-30 year time scales. In this model there are westward propagating temperature anomalies, as in the observations, and these anomalies are associated with anomalies in SSH on the eastern and western boundaries of the North Atlantic. The correlation is strongest along the western boundary (the North American coast) where the temperature anomalies, and thus the SSH anomalies, have a larger amplitude than along the eastern boundary. The longer time series of tide gauge observations that is available around the North Atlantic allows us to distinguish the 20-30 year period variability from the 50-70 year period.

The different periods attributed to the AMO raises the issue of how the AMO should be defined. Which time scale and pattern should be associated with it? Are the 20-30 and 50-70 year time scales really different and do they have different spatial patterns? From the short observational record it is difficult to be sure. Additionally, different GCMs show different time scales. The 50-70 year time scale that is generally associated with the AMO comes from the classical AMO index which is the detrended SST averaged over the North Atlantic basin. The shorter time scale comes from examining subsurface temperatures (from XBTs) and SSH (from tide gauges). In chapter 6 we found that the 20-30 year period is present in other data sets such as the Central England Temperature record and two records of net snow accumulation from ice cores in Greenland. Returning once again to the SST record, the 20-30 year period is found when a smaller area is chosen for the averaging of anomalies while the 50-70 year period appears when averaging over the whole basin. The two time scales are also found in the control run of the GFDL CM2.1 GCM. The time scale of westward propagating anomalies in observations suggests that the shorter period is caused by the internal mode from the minimal model

but the observational record is too short to make any similar statements about the longer period variability. In the GFDL CM2.1 model there is variability of salinity in the Arctic ocean from which anomalies may propagate into the North Atlantic.

Salinity variability in the Arctic was further investigated in chapter 7. Using a minimal model of multidecadal variability in the Arctic the normal modes of the salinity driven flow were investigated. Under zero forcing the modes are all damped and stationary, as forcing is increased a merger between two stationary modes occurs, resulting in an oscillatory mode with a multidecadal period. The spatial pattern of this mode, bearing in mind the deformational effect of realistic bathymetry, resembles the salinity variability found in the GFDL CM2.1 model in chapter 6.

There remain many questions around the AMO. While it appears that the same mechanism is at work in the GFDL CM2.1 model as in the minimal model, studies using other GCMs have offered alternative explanations. It would be very interesting to ascertain whether phenomena such as the westward propagation of temperature anomalies across the North Atlantic and the variability of salinity in the Arctic are visible in these GCMs, and whether the variability described under the alternative explanations can be linked back to the basic minimal model mechanism.

From the point of view of the minimal model, further investigation into the salinity modes in the Arctic is warranted. The effect of more realistic bathymetry on the spatial pattern of the mode is an interesting question, as is the effect of more realistic forcing. Another important issue is whether oscillations of a similar character appear in other models, not only coupled GCMs but also other Arctic models of varying complexity.

In addition, there is the connection between the Arctic and the North Atlantic to consider. Can the salinity oscillations in the Arctic be excited by variability in the North Atlantic, and will the anomalies which feed back into the North Atlantic from the Arctic be enough to cause the Arctic time scale to appear in the North Atlantic? Since the oscillations in the Arctic are found in salinity rather than temperature we require a mechanism to transfer this Arctic salinity variability into temperature variability in the North Atlantic on the same time scale. A first step in this direction would be to couple the minimal model of the North Atlantic with the minimal model of the Arctic and examine the variability of the joint system.

Coming back to the issue of predictability of the climate which was raised in the introduction to this thesis, having a robust theory of the mechanism behind the low frequency variability of the North Atlantic and Arctic is important in making more accurate long term forecasts for this part of the climate system. Given the links between the AMO and the climate of the surrounding continents, and the possible links between North Atlantic variability and the recent dramatic changes in Arctic sea-ice, this becomes a very timely question, one that it is hoped this thesis goes some way towards answering.

BIBLIOGRAPHY

Alvarez-Garcia, F., Latif, M., and Biastoch, A., On multidecadal and quasi-decadal North Atlantic variability, *Journal of Climate*, *21*, 3433–3452, 2008.

Banta, J. R. and McConnell, J. R., Annual accumulation over recent centuries at four sites in central Greenland, *Journal of Geophysical Research*, *112*, 2007.

Barsugli, J. J. and Battisti, D. S., The basic effects of atmosphere-ocean thermal coupling on midlatitude variability, *Journal of Atmospheric Science*, *55*, 477–493, 1998.

Belkin, I. M., Levitus, S., Antonov, J. I., and Malmberg, S.-A., "Great Salinity Anomalies" in the North Atlantic, *Progress in Oceanography*, *41*, 1–68, 1998.

Bingham, R. J. and Hughes, C. W., Signature of the Atlantic meridional overturning circulation in sea level along the east coast of North America, *Geophysical Research Letters*, *36*, 2009.

Broecker, W. S., The great ocean conveyor, *Oceanography*, *4*, 79–89, 1991.

Cane, M. A., Climate science: Decadal predictions in demand, *Nature Geoscience*, *3*, 231–232, 2010.

Cayan, D. R., Latent and sensible heat flux anomalies over the northern oceans: The connection to monthly atmospheric circulation, *Journal of Climate*, *5*, 354–369, 1992a.

Cayan, D. R., Latent and sensible heat flux anomalies over the northern oceans: Driving the sea surface temperature, *Journal of Physical Oceanography*, *22*, 859–881, 1992b.

Chen, F. and Ghil, M., Interdecadal variability in a hybrid coupled ocean-atmosphere model, *Journal of Physical Oceanography*, *26*, 1561–1578, 1996.

Cheng, W., Bleck, R., and Rooth, C., Multi-decadal thermohaline variability in an ocean-atmosphere general circulation model, *Climate Dynamics*, *22*, 573–590, 2004.

Delworth, T. L. and coauthors, GFDL's CM2 global coupled climate models. part I: Formulation and simulation characteristics, *Journal of Climate*, *19*, 643–674, 2006.

Delworth, T. L. and Greatbatch, R. J., Multidecadal thermohaline circulation variability driven by atmospheric surface flux forcing, *Journal of Climate*, *13*, 1481–1495, 2000.

Delworth, T. L. and Mann, M. E., Observed and simulated multidecadal variability in the Northern Hemisphere, *Climate Dynamics*, *16*, 661–676, 2000.

Delworth, T. L., Manabe, S., and Stouffer, R. J., Interdecadal variations of the thermohaline circulation in a coupled ocean-atmosphere model, *Journal of Climate*, *6*, 1993–2011, 1993.

Delworth, T. L., Manabe, S., and Stouffer, R. J., Multidecadal climate variability in the Greenland sea and surrounding regions: a coupled model simulation, *Geophysical Research Letters*, *24*, 257–260, 1997.

Dijkstra, H. A., *Nonlinear Physical Oceanography*, Springer, Dordrecht, Netherlands, 2005.

Dijkstra, H. A., Interaction of SST modes in the North Atlantic Ocean, *Journal of Physical Oceanography*, *36*, 286–299, 2006.

Dijkstra, H. A. and von der Heydt, A., Localization of multidecadal variability: II. spectral origin of multidecadal modes, *Journal of Physical Oceanography*, *37*, 2415–2428, 2007.

Dijkstra, H. A., te Raa, L. A., Schmeits, M., and Gerrits, J., On the physics of the Atlantic Multidecadal Oscillation, *Ocean Dynamics*, *56*, 36–50, 2006.

Divine, D. V. and Dick, C., Historical variability of sea ice edge positions in the Nordic seas, *Journal of Geophysical Research*, *111*, C01 001, 2006.

Dong, B. and Sutton, R. T., Mechanism of interdecadal thermohaline circulation variability in a coupled ocean-atmosphere GCM, *Journal of Climate*, *18*, 1117–1135, 2005.

Eden, C. and Jung, T., North Atlantic interdecadal variability: Oceanic response to the North Atlantic Oscillation (1865–1997), *Journal of Climate*, *14*, 676–691, 2001.

Enfield, D. B. and Cid-Serrano, L., Projecting the risk of future climate shifts, *International Journal of Climatology*, *26*, 885–895, 2006.

Enfield, D. B., Mestas-Nuñez, A. M., and Trimble, P. J., The Atlantic Multidecadal Oscillation and its relation to rainfall and river flows in the continental U.S., *Geophysical Research Letters*, *28*, 2077–2080, 2001.

Farrell, B. F. and Ioannou, P. J., Generalized stability theory. I: Autonomous operators, *Journal of Atmospheric Science*, *53*, 2025–2040, 1996.

Fedorov, A. and Philander, S., Is El Niño changing?, *Science*, *288*, 1997–2002, 2000.

Feng, S. and Hu, Q., How the North Atlantic Multidecadal Oscillation may have influenced the Indian summer monsoon during the past two millennia, *Geophysical Research Letters*, *35*, L01 707, 2008.

Ganachaud, A. and Wunsch, C., Improved estimates of global ocean circulation, heat transport and mixing from hydrographic data, *Nature*, *408*, 453–457, 2000.

Ghil, M., Natural climate variability, in *Encyclopedia of Global Environmental Change, volume 1*, edited by T. Munn, M. C. MacCracken, and J. S. Perry, Wiley, 2002.

Ghil, M. and Vautard, R., Interdecadal oscillations and the warming trend in global temperature time series, *Nature*, *350*, 324–327, 1991.

Ghil, M., Allen, M. R., Dettinger, M. D., Ide, K., Kondrashov, D., Mann, M. E., Robertson, A. W., Saunders, A., Tian, Y., Varadi, F., and Yiou, P., Advanced spectral methods for climatic time series, *Reviews of Geophysics*, *40*, 1–41, 2002a.

Ghil, M., Allen, R. M., Dettinger, M. D., Ide, K., Kondrashov, D., Mann, M. E., Robertson, A., Saunders, A., Tian, Y., Varadi, F., and Yiou, P., Advanced spectral methods for climatic time series, *Reviews of Geophysics*, *40*, 2002b.

Goldenberg, S. B., Landsea, C. W., nez, A. M. M.-N., and Gray, W. M., The recent increase in Atlantic hurricane activity: Causes and implications, *Science*, *293*, 474–479, 2001.

Gouretski, V. and Koltermann, K. P., How much is the ocean really warming?, *Geophysical Research Letters*, *34*, L01 610, 2007.

Greatbatch, R. J. and Zhang, S., An interdecadal oscillation in an idealized ocean basin forced by constant heat flux, *Journal of Climate*, *8*, 81–91, 1995.

Griffies, S. M. and Bryan, K., Predictability of North Atlantic multidecadal climate variability, *Science*, *275*, 181–184, 1997.

Griffies, S. M. and Tziperman, E., A linear thermohaline oscillator driven by stochastic atmospheric forcing, *Journal of Climate*, *8*, 2440–2453, 1995.

Grosfeld, K., Lohmann, G., Rimbu, N., Fraedrich, K., and Lunkeit, F., Atmospheric multidecadal variation in the North Atlantic realm: proxy data, observations, and atmospheric circulation model studies, *Climate of the Past*, *3*, 39–50, 2007.

Guckenheimer, J. and Holmes, P., *Nonlinear Oscillations, Dynamical Systems and Bifurcations of Vector Fields*, 2^{nd} *edition*, Springer-Verlag, Berlin/Heidelberg, 1990.

Haak, H., Jungclaus, J., Mikolajewicz, U., and Latif, M., Formation and propagation of great salinity anomalies, *Geophysical Research Letters*, *30*, 2003.

Hansen, D. V. and Bezdek, H. F., On the nature of decadal anomalies in North Atlantic sea surface temperature, *Journal of Geophysical Research*, *101*, 8749–8758, 1996.

Hasselmann, K., Stochastic climate models. I: Theory, *Tellus*, *28*, 473–485, 1976.

Hawkins, E. and Sutton, R. T., Variability of the Atlantic thermohaline circulation described by three-dimensional empirical orthogonal functions, *Climate Dynamics*, *29*, 745–762, 2007.

Holgate, S. J., On the decadal rates of sea level change during the twentieth century, *Geophysical Research Letters*, *34*, L01 602, 2007.

Huck, T. and Vallis, G. K., Linear stability analysis of the three-dimensional thermally-driven ocean circulation: application to interdecadal oscillations, *Tellus A*, *53*, 526–545, 2001.

Huck, T., de Verdiére, A. C., and Weaver, A. J., Interdecadal variability of the thermohaline circulation in box-ocean models forced by fixed surface fluxes, *Journal of Physical Oceanography*, *29*, 865–892, 1999.

Huck, T., Vallis, G. K., and Colin de Verdiére, A., On the robustness of the interdecadal modes of the thermohaline circulation, *Journal of Climate*, *14*, 940–963, 2001.

Jin, F.-F. and Neelin, J. D., Modes of interannual tropical ocean-atmosphere interaction - a unified view. I: Numerical results., *Journal of Atmospheric Science*, *50*, 3477–3503, 1993.

Jungclaus, J. H., Haak, H., Latif, M., and Mikolajewicz, U., Arctic-North Atlantic interactions and multidecadal variability of the meridional overturning circulation, *Journal of Climate*, *18*, 4013–4031, 2005.

Jungclaus, J. H., Keenlyside, N., Botzet, M., Haak, H., Luo, J.-J., Marotzke, J., Mikolajewicz, U., and Roeckner, E., Ocean circulation and tropical variability in the coupled model ECHAM5/MPI-OM, *Journal of Climate*, *19*, 3952–3972, 2006.

Kaplan, A., Kushnir, Y., Cane, M. A., and Blumenthal, M. B., Reduced space optimal analysis for historical data sets: 136 years of Atlantic sea surface temperatures, *Journal of Geophysical Research*, *102*, 27 835–27 860, 1997.

Keenlyside, N. S., Latif, M., Jungclaus, J., Kornblueh, L., and Roeckner, E., Advancing decadal-scale climate prediction in the North Atlantic sector, *Nature*, *453*, 84–88, 2008.

Keller, H. B., Numerical solution of bifurcation and nonlinear eigenvalue problems, in *Applications of Bifurcation Theory*, edited by P. H. Rabinowitz, Academic Press, New York, U.S.A., 1977.

Kerr, R. A., A North Atlantic climate pacemaker for the centuries, *Science*, *288*, 1984–1986, 2000.

Knight, J. R., Allan, R. J., Folland, C. K., Vellinga, M., and Mann, M. E., A signature of persistent natural thermohaline circulation cycles in observed climate, *Geophysical Research Letters*, *32*, L20 708, 2005.

Knight, J. R., Folland, C. K., and Scaife, A. A., Climate impacts of the Atlantic Multidecadal Oscillation, *Geophysical Research Letters*, *33*, L17 706, 2006.

Kushnir, Y., Interdecadal variations in North Atlantic sea surface temperature and associated atmospheric conditions, *Journal of Climate*, *7*, 141–157, 1994.

Levitus, S., Antonov, J. I., Boyer, T. P., and Stephens, C., Warming of the World Ocean, *Science*, *287*, 2225–2229, 2000.

Luterbacher, J., Xoplaki, E., Dietrich, D., Jones, P. D., Davies, T. D., Portis, D., Gonzales-Rouco, J. F., von Storch, H., Gyalistras, D., Casty, C., and Wanner, H., Extending North Atlantic Oscillation reconstructions back to 1500, *Atmospheric Science Letters*, *2*, 114–124, 2002.

Mann, M. E. and Emanuel, K. A., Atlantic hurricane trends linked to climate change, *EOS*, *87*, 233–244, 2006.

Miller, L. and Douglas, B. C., Gyre-scale atmospheric pressure variations and their relation to 19th and 20th century sea level rise, *Geophysical Research Letters*, *34*, L16 602, 2007.

Molinari, R. L., Mayer, D. A., Festa, J. F., and Bezdek, H. F., Multiyear variability in the near-surface temperature structure of the midlatitude western North Atlantic Ocean, *Journal of Geophysical Research*, *102*, 3267–3278, 1997.

Neelin, J. D., Battisti, D. S., Hirst, A. C., Jin, F.-F., Wakata, Y., Yamagata, T., and Zebiak, S. E., ENSO Theory, *Journal of Geophysical Research*, *103*, 14,261–14,290, 1998.

Nøst, O. A. and Isachsen, P. E., The large-scale time-mean ocean circulation in the Nordic Seas and Arctic Ocean estimated from simplified dynamics, *Journal of Marine Research*, *61*, 175–210, 2003.

Pacanowski, R. C. and Griffies, S. M., MOM 3.0 Manual, http://www.gfdl.gov/∼smg/MOM/web/guide_parent/guide_parent.html, 2000.

Peizoto, J. P. and Oort, A. H., Physics of climate, *Reviews of Modern Physics*, *56*, 365–429, 1984.

Philander, S. G. H., *El Niño and the Southern Oscillation*, Academic Press, New York, 1990.

Plaut, G., Ghil, M., and Vautard, R., Interannual and interdecadal variability in 335 years of Central England temperatures, *Science*, *268*, 710–713, 1995.

Pohlmann, H., Botzet, M., Latif, M., Roesch, A., Wild, M., and Tschuck, P., Estimating the decadal predictability of a coupled aogcm, *Journal of Climate*, *17*, 4463–4472, 2004.

Polyakov, I. V. and Johnson, M. A., Arctic decadal and interdecadal variability, *Geophysical Research Letters*, *27*, 2000.

Polyakov, I. V., Alekseev, G. V., Bekryaev, R. V., Bhatt, U. S., Colony, R., Johnson, M. A., Karklin, V. P., Walsh, D., and Yulin, A. V., Long-term ice variability in Arctic

marginal seas, *Journal of Climate*, *16*, 2078–2085, 2003a.

Polyakov, I. V., Bekryaev, R. V., Alekseev, G. V., Bhatt, U. S., Colony, R. L., Johnson, M. A., Maskshtas, A. P., and Walsh, D., Variability and trends of air temperature and pressure in the maritime arctic, 1875-2000, *Journal of Climate*, *16*, 2067–2077, 2003b.

Polyakov, I. V., Walsh, D., Dmitrenko, I., Colony, R. L., and Timokhov, L. A., Arctic Ocean variability derived from historical observations, *Geophysical Research Letters*, *30*, 2003c.

Polyakov, I. V., Alekseev, G. V., Timokhov, L. A., Bhatt, U. S., Colony, R. L., Simmons, H. L., Walsh, D., Walsh, J. E., and Zakharov, V. F., Variability of the intermediate Atlantic water of the Arctic Ocean over the last 100 years, *Journal of Climate*, *17*, 4485–4497, 2004.

Rayner, N. A., Parker, D. E., Horton, E. B., Folland, C. K., Alexander, L. V., Rowell, D. P., Kent, E. C., and Kaplan, A., Global analyses of sea surface temperature, sea ice, and night marine air temperature since the late nineteenth century, *Journal of Geophysical Research*, *108*, 10.1029/2002JD002 670, 2003.

Rayner, N. A., Brohan, P., Parker, D. E., Folland, C. K., Kenndy, J. J., Vanicek, M., Ansell, T. J., and Tett, S. F. B., Improved analysis of changes and uncertainties in sea surface temperature measured in situ since the mid-ninteenth century: The HadSST2 dataset, *Journal of Climate*, *19*, 446–469, 2006.

Roulston, M. and Neelin, J. D., The response of an ENSO model to climate noise, weather noise and intraseasonal forcing, *Geophysical Research Letters*, *27*, 3723–3726, 2000.

Saravanan, R. and McWilliams, J. C., Stochasticity and spatial resonance in interdecadal climate fluctuations, *Journal of Climate*, *10*, 2299–2320, 1997.

Saravanan, R. and McWilliams, J. C., Advective ocean-atmosphere interaction: An analytical stochastic model with implications for decadal variability, *Journal of Climate*, *11*, 165–188, 1998.

Schlesinger, M. E. and Ramankutty, N., An oscillation in the global climate system of period 65-70 years, *Nature*, *367*, 723–726, 1994.

Sévellec, F., Huck, T., Ben Jelloul, M., and Vialard, J., Nonnormal multidecadal response of the thermohaline circulation induced by optimal surface salinity perturbations, *Journal of Physical Oceanography*, *39*, 852–872, 2009.

Sleijpen, G. L. G. and van der Vorst, H. A., A Jacobi-Davidson iteration method for linear eigenvalue problems, *SIAM J. Matrix Anal. Appl.*, *17*, 410–425, 1996.

Sterl, A., Severijns, C., Dijkstra, H. A., Hazeleger, W., van Oldenborgh, G. J., van den Broeke, M., Burgers, G., van den Hurk, B., van Leeuwen, P. J., and van Velthoven, P., When can we expect extremely high surface temperatures?, *Geophysical Research Letters*, *35*, L14 703, 2008.

Stouffer, R. J., Yin, J., Gregory, J. M., Dixon, K. W., Spelman, M. J., Hurlin, W., Weaver, A. J., and et. al., Investigating the causes of the response of the thermohaline circulation to past and future climate changes, *Journal of Climate*, *19*, 1365–1387, 2006.

Stroeve, J., Holland, M. M., Meier, W., Scambos, T., and Serreze, M., Arctic sea ice decline: Faster than forecast, *Geophysical Research Letters*, *34*, 2007.

Sutton, R. T. and Allen, M. R., Decadal predictability of North Atlantic sea surface temperature and climate, *Nature*, *388*, 563–567, 1997.

Sutton, R. T. and Hodson, D. L., Atlantic Ocean forcing of North American and European summer climate, *Science*, *309*, 115–118, 2005.

te Raa, L. A. and Dijkstra, H. A., Instability of the thermohaline ocean circulation on interdecadal timescales, *Journal of Physical Oceanography*, *32*, 138–160, 2002.

te Raa, L. A. and Dijkstra, H. A., Modes of internal thermohaline variability in a single-hemispheric ocean basin, *Journal of Marine Research*, *61*, 491–516, 2003.

te Raa, L. A., Gerrits, J., and Dijkstra, H. A., Identification of the mechanism of interdecadal variablity in the North Atlantic Ocean, *Journal of Physical Oceanography*, *34*, 2792–2807, 2004.

Thompson, D. W. J. and Wallace, J. M., Regional climate impacts of the northern hemisphere annular mode, *Science*, *293*, 85–89, 2001.

Timmermann, A., Latif, M., Voss, R., and Grötzner, A., Northern hemisphere interdecadal variability: A coupled air-sea mode, *Journal of Climate*, *11*, 1906–1931, 1998.

Unal, Y. S. and Ghil, M., Interannual and interdecadal oscillation patterns in sea level, *Climate Dynamics*, *11*, 255–278, 1995.

van Oldenborgh, G. J., te Raa, L. A., Dijkstra, H. A., and Philip, S. Y., Frequency- or amplitude dependent effects of the Atlantic meridional overturning on the tropical Pacific Ocean, *Ocean Science*, *5*, 293–301, 2009.

Vautard, R., Yiou, P., and Ghil, M., Singular-spectrum analysis: A toolkit for short, noisy chaotic signals, *Physica D: Nonlinear Phenomena*, *58*, 95–126, 1992.

Vellinga, M. and Wu, P., Low-latitude freshwater influence on centennial variability of the Atlantic thermohaline circulation, *Journal of Climate*, *17*, 4498–4511, 2004.

Venegas, S. A. and Mysak, L. A., Is there a dominant timescale of natural climate variability in the Arctic?, *Journal of Climate*, *13*, 3412–3434, 2000.

Vinje, T., Loyning, T. B., and Polyakov, I., Effects of melting and freezing in the Greenland sea, *Geophysical Research Letters*, *29*, 2002.

Visbeck, M., Chassignet, E. P., Curry, R. G., Delworth, T. L., Dickson, R. R., and Krahmann, G., The ocean's response to North Atlantic Oscillation variability, in *The North Atlantic Oscillation: Climatic Significance and Environmental Impact*, edited by J. W. Hurrell, Y. Kushnir, G. Ottersen, and M. Visbeck, Geophysical Monograph 134, American Geophysical Union, 2003.

von der Heydt, A. and Dijkstra, H. A., Localization of multidecadal variability: I. Cross equatorial transport and interbasin exchange, *Journal of Physical Oceanography*, *37*, 2401–2414, 2007.

Winton, M. and Sarachik, E. S., Thermohaline oscillations induced by strong steady salinity forcing of general circulation models, *Journal of Physical Oceanography*, *23*, 1389–1410, 1993.

Woodworth, P. L. and Player, R., The Permanent Service for Mean Sea Level: An update to the 21st century, *Journal of Coastal Research*, *19*, 287–295, 2003.

Yan, Z., Tsimplis, M. N., and Woolf, D., Analysis of the relationship between the North Atlantic Oscillation and sea-level changes in northwest Europe, *International Journal of Climatology*, *24*, 743–758, 2004.

Yin, J., Schlesinger, M. E., and Stouffer, R. J., Model projections of rapid sea-level rise on the northeast coast of the United States, *Nature Geoscience*, *2*, 262–266, 2009.

Zanna, L. and Tziperman, E., Optimal surface excitation of the thermohaline circulation,

Journal of Physical Oceanography, *38*, 1820–1830, 2008.

Zebiak, S. E. and Cane, M. A., A model El Niño-Southern Oscillation., *Mon. Wea. Rev.*, *115*, 2262–2278, 1987.

Zhang, R., Coherent surface-subsurface fingerprint of the Atlantic meridional overturning circulation, *Geophysical Research Letters*, *35*, L20 705, 2008.

Zhang, R. and Delworth, T. L., Impact of Atlantic multidecadal oscillations on India/Sahel rainfall and Atlantic hurricanes, *Geophysical Research Letters*, *33*, L17 712, 2006.

Zhang, R. and Vallis, G. K., Impact of Great Salinity Anomalies on the low-frequency variability of the North Atlantic climate, *Journal of Climate*, *19*, 470–482, 2006.

Zhang, R., Delworth, T. L., and Held, I. M., Can the Atlantic Ocean drive the observed multidecadal variability in northern hemisphere mean temperature?, *Geophysical Research Letters*, *34*, L02 709, 2007.

Zhu, X. and Jungclaus, J. H., Interdecadal variability of the meridional overturning circulation as an ocean internal mode, *Climate Dynamics*, *31*, 731–741, 2008.

ACKNOWLEDGEMENTS

Although only my name appears on the front of this thesis, there are many people who have contributed to it. Firstly, my supervisor - thank you Henk for hiring me, sight unseen, on the strength of a recommendation and a phone interview. It's been an amazing experience and you have been a wonderful supervisor, always available in person or by email and always full of inspirational ideas. Anna, my co-promotor, you have been a great source of support and encouragement.

My colleagues and friends at IMAU, you have made the last four years of work a pleasure. Thank you to all of you for interesting discussions at lunch and tea breaks (and occasionally delicious cake as well), for tips on everything from MATLAB and ferret to which restaurants in the city to avoid, for commiserations when I'm stressed and congratulations when I'm successful. Lianke, I will be forever grateful for your numerous patient explanations when I was just getting started. Virginia, my first office-mate, you helped me get settled and learn the way of things at IMAU. Petra, the ocean group hasn't quite been the same since you graduated. Mirjam, an honourary IMAU-er, I hope our discussions will continue regardless of what we both end up doing in the future. Dewi, Erik, Matthijs, Yvonne, my temporary office-mates on the 5th floor, it's been fun! Selma, my temporary and permanent office-mate, I'm so glad you moved in with me! I'm sure we spent more time than we should have chatting rather than researching, but it's definitely been worth it. A special thank you to Selma for translating my summary into Dutch, and to Matthijs for checking it.

How does one adequately thank one's family? Mum, Dad, Luke, Nim, you have always been absolutely supportive of whatever I have chosen to do, barely even batting an eyelash when I decided that I was moving off to the other side of the world. Mum, your proof-reading skills are awesome. I should really brush up on my grammar and punctuation! Thanks Dad, for painting me a perfect thesis cover. I'm glad that you found artistic inspiration in my work and very proud to display the result.

My extended family of friends, spread all over the world, everywhere I go, there you are! Min, Mel, isn't it convenient how Europe is so tiny? Aradhana, you are a constant inspiration. Nefta, without whom I would have had no social life, and Henriette, the world's most easy going housemate, I was lucky to find both of you.

Finally, to my teachers and fellow students from school, college and university who have made the search for knowledge such a fascinating journey - thank you.

Curriculum Vitae

Leela Frankcombe was born on the 13th of January 1984 in Melbourne, Australia. She completed high school in 2001 and in 2002 began a Bachelor of Science degree at the Australian National University in Canberra, studying physics and astronomy. She had plans to spend the rest of her life star-gazing until in her third year she took a course on geophysical fluid dynamics and decided that down-to-earth science was much more interesting. Her honours research project, on time dependence in hydraulic flows, was conducted at the Research School of Earth Sciences at the Australian National University, from where she graduated with an honours degree in 2005. In 2006 she moved to the Netherlands, arriving in the country with only the clothes on her back (the rest of her luggage having missed a connecting flight). For the next four years she worked as a PhD student at the Institute for Marine and Atmospheric research, Utrecht. The fruits of that labour are presented in this thesis.

PUBLICATIONS

Dijkstra, H. A., L. M. Frankcombe and A. von der Heydt (2008), A stochastic dynamical systems view of the Atlantic Multidecadal Oscillation, *Philosophical Transactions of the Royal Society A*, **366**, 2545-2560.

Frankcombe, L. M., H. A. Dijkstra and A. von der Heydt (2008), Sub-surface signatures of the Atlantic Multidecadal Oscillation, *Geophysical Research Letters*, **35**, L19602.

Frankcombe, L. M., H. A. Dijkstra and A. von der Heydt (2009), Noise-induced multidecadal variability in the North Atlantic: Excitation of normal modes, *Journal of Physical Oceanography*, **39** (1), 220–233.

Frankcombe, L. M. and H. A. Dijkstra (2009), Coherent multidecadal variability in North Atlantic sea level, *Geophysical Research Letters*, **36**, L15604.

Frankcombe, L. M., H. A. Dijkstra and A. von der Heydt (2010), The Atlantic Multidecadal Oscillation: a stochastic dynamical systems view, in *Stochastic Physics and Climate Modelling* (ed. T. Palmer and P. Williams), pp. 287-306.

Frankcombe, L. M., A. S. von der Heydt and H. A. Dijkstra, North Atlantic multidecadal climate variability: An investigation of dominant time scales and processes, *accepted by the Journal of Climate*.

Frankcombe, L. M. and H. A. Dijkstra, Internal modes of multidecadal variability in the Arctic Ocean, *submitted to the Journal of Physical Oceanography*.